INNOVATIVE PAYLOADS FOR SMALL UNMANNED AERIAL SYSTEM-BASED PERSONAL REMOTE SENSING AND APPLICATIONS

by

Austin M. Jensen

A dissertation submitted in partial fulfillment
of the requirements for the degree

of

DOCTOR OF PHILOSOPHY

in

Electrical Engineering

Approved:

Dr. YangQuan Chen Major Professor	Dr. Mac McKee Committee Member
Dr. David Geller Committee Member	Dr. Don Cripps Committee Member
Dr. Jacob Gunther Committee Member	Dr. Mark R. McLellan Vice President for Research and Dean of the School of Graduate Studies

UTAH STATE UNIVERSITY
Logan, Utah

2014

Abstract

Innovative Payloads for Small Unmanned Aerial System-Based Personal Remote Sensing and Applications

by

Austin M. Jensen, Doctor of Philosophy

Utah State University, 2014

Major Professor: Dr. YangQuan Chen
Department: Electrical and Computer Engineering

Remote sensing enables the acquisition of large amounts of data, over a small period of time, in support of many ecological applications (i.e. precision agriculture, vegetation mapping, etc.) commonly from satellite or manned aircraft platforms. This dissertation focuses on using small unmanned aerial systems (UAS) as a remote sensing platform to collect aerial imagery from commercial-grade cameras and as a radio localization platform to track radio-tagged fish. The small, low-cost nature of small UAS enables remotely sensed data to be captured at a lower cost, higher spatial and temporal resolution, and in a more timely manner than conventional platforms. However, these same attributes limit the types of cameras and sensors that can be used on small UAS and introduce challenges in calibrating the imagery and converting it into actionable information for end users. A major contribution of this dissertation addresses this issue and includes a complete description on how to calibrate imagery from commercial-grade visual, near-infrared, and thermal cameras. This includes the presentation of novel surface temperature sampling methods, which can be used during the flight, to help calibrate thermal imagery. Landsat imagery is used to help evaluate these methods for accuracy; one of the methods performs very well and is logistically feasible for regular use. Another major contribution of this dissertation includes

novel, simple methods to estimate the location of radio-tagged fish using multiple unmanned aircraft (UA). A simulation is created to test these methods, and Monte Carlo analysis is used to predict their performance in real-world scenarios. This analysis shows that the methods are able to locate the radio-tagged fish with good accuracy. When multiple UAs are used, the accuracy does not improve; however the fish is located much quicker than when one UA is used.

(154 pages)

Public Abstract

Innovative Payloads for Small Unmanned Aerial System-Based Personal Remote Sensing and Applications

by

Austin M. Jensen, Doctor of Philosophy

Utah State University, 2014

Major Professor: Dr. YangQuan Chen
Department: Electrical and Computer Engineering

Remote sensing enables the acquisition of large amounts of data, over a small period of time, in support of many ecological applications (i.e. precision agriculture, vegetation mapping, etc.) commonly from satellite or manned aircraft platforms. This dissertation focuses on using small unmanned aerial systems (UAS) as a remote sensing platform to collect aerial imagery from commercial-grade cameras and as a platform to track radio-tagged fish. The small, low-cost nature of small UAS enable remotely sensed data to be captured at a lower cost, higher spatial and temporal resolution, and in a more timely manner than conventional platforms. However, these same attributes limit the types of cameras and sensors that can be used on small UAS and introduce challenges in calibrating the imagery and converting it into actionable information for end users. A major contribution of this dissertation addresses this issue and includes a complete description on how to calibrate imagery from commercial-grade visual, near-infrared, and thermal cameras. Another major contribution includes novel, simple methods to estimate the location of radio-tagged fish. Simulations are used to evaluate these methods and predict their performance in real-world scenarios.

Acknowledgments

I am very grateful to my adviser, Dr. YangQuan Chen, for giving me this opportunity, providing me with such a great project, and teaching me how to properly conduct meaningful research. My committee members have also been vital in support of this project, especially Dr. Mac McKee whose vision started the AggieAir project and who has been a great mentor and friend to me. I appreciate all those who helped me collect and process the data needed for the surface temperature sampling (Rick Cressall, Ian Gowing, Shannon Syrstad, Mark Winkelaar, Chris Thomas, Dan Robinson, Ben Kendall, Jon Thorne, Tyler Jacox, Alfonso Torres, Manal Alarab, Miguel Leonardo, etc.). Thank you Miguel Leonardo and Ivan Jimenez for your hardware developments on the fish-tracking payload which was used to collect the data used in the propagation model. I also acknowledge the countless others over the past few years who have contributed indirectly to this work in many ways (Cal Coopmans, Chris Coffin, Aaron Quitberg, Jarret Bone, Jinlu Han, Nathan Hoffer, Jeremy Frint, Haiyang Chao, Di Long, etc.). Most of all, I owe this work to my enduring, loving wife and my patient children for their endless sacrifices and relentless support.

Austin M. Jensen

Contents

Page

Abstract . . . **iii**

Public Abstract . . . **v**

Acknowledgments . . . **vi**

List of Tables . . . **ix**

List of Figures . . . **x**

Acronyms . . . **xiv**

1 Introduction . . . **1**
1.1 Unmanned Aerial System-Based Remote Sensing . . . 3
1.2 Dissertation Contributions and Organization . . . 4

2 AggieAir - A UAS-Based Multispectral Remote Sensing System . . . **6**
2.1 Launching and Landing . . . 8
2.2 Paparazzi Autopilot . . . 10
2.3 Payload . . . 11
2.4 Ground Station . . . 11
2.5 Paparazzi Ground Control Station . . . 12
2.6 US Government Regulations and FAA Certificate of Authorization . . . 14
2.7 Chapter Summary . . . 15

3 Visual Near-infrared Imagery . . . **16**
3.1 Radiometric Calibration . . . 16
3.2 Geometric Camera Calibration . . . 20
3.3 Creating Orthorectified Mosaics . . . 20
3.4 Chapter Summary . . . 21

4 Thermal Imagery . . . **25**
4.1 Preparation for Orthorectification . . . 25
4.2 Geometric Calibration . . . 29
4.3 Compensate for External Disturbances . . . 30
4.3.1 Ground Sampling Methods . . . 33
4.3.2 Evaluating the Ground Sampling Methods . . . 43
4.3.3 Ground Sampling Conclusions . . . 52
4.4 Chapter Summary . . . 53

5 Biotelemetry Fish Tracking **54**
5.1 Simulation Environment 55
5.1.1 Environmental Dynamics 58
5.1.2 UA System Dynamics 59
5.1.3 Simulating and Estimating the Tag Location 64
5.1.4 Navigation using Potential Fields 67
5.2 Experimental Results 73
5.2.1 Flight Simulation 73
5.2.2 Monte Carlo Simulations 81
5.2.3 Summary 83
5.3 Chapter Summary 84

6 Delivering Actionable Information **86**
6.1 Vegetation Mapping 86
6.2 Precision Agriculture 88
6.3 Fish Thermal Refugia 92
6.4 Cyber Physical System Based on small UAS-Based Remote Sensing 93
6.5 Chapter Summary 94

7 Conclusions and the Future of Small UAS Remote Sensing **96**

References **98**

Appendix **105**

Vita **133**

List of Tables

Table Page

2.1 Specifications for the AggieAir-Minion aircraft. 7

4.1 A thermal camera comparison for remote sensing. 26

4.2 Flight altitude vs. sample area size. 34

4.3 Flight altitude vs. ground camera height. 35

4.4 Flight altitude vs. camera height. 36

4.5 Standard deviation of temperature distribution for pool discharge systems. 40

4.6 Regression results of surface sampling methods for flight #1 (May 16th). . . 46

4.7 Regression results of surface sampling methods for flight #2 (June 1st). . . 47

4.8 Regression results of surface sampling methods for flight #3 (June 9th). . . 47

4.9 Regression results of surface sampling methods for flight #4 (June 17th). . 47

4.10 Regression results of surface sampling methods for flight #5 (June 25th). . 47

4.11 Ground camera and pool models compared to Landsat data. 51

4.12 Correlation between possible error sources and ground camera model Landsat goodness of fit. 52

4.13 Correlation between weather parameters and ground camera model coefficients. 52

5.1 Parameters for the fish-tracking flight simulation. 76

5.2 Monte Carlo simulation results for tag error dispersion and 100 flights (meters). 82

List of Figures

Figure Page

1.1 The Processing Cycle for Meaningful Remote Sensing. 2

1.2 The AggieAir-Minion aircraft with a VIS-NIR payload. 5

2.1 AggieAir-Minion airframe layout. 7

2.2 AggieAir-Minion fuselage layout. 7

2.3 AggieAir-Minion avionics layout. 8

2.4 Diagram of AggieAir auto-takeoff procedure. 9

2.5 Diagram of AggieAir auto-landing procedure. 9

2.6 Diagram of the AggieAir payload system. 11

2.7 AggieAir ground station diagram. 12

2.8 Paparazzi ground control station software interface. 13

3.1 Processing diagram for VIS-NIR imagery. 17

3.2 Reflectance factor explanation. 18

3.3 Taking a picture of the white panel before and after flight. 19

3.4 The picture of the white panel after stretching the contrast. 20

3.5 Target for camera calibration toolbox for Matlab. 21

3.6 The reference target for geometric camera calibration. 22

3.7 Individual raw visual images captured from a flight. 23

3.8 Individual images after direct georeferencing. 23

3.9 Orthorectified mosaic using 200 images from AggieAir and EnsoMOSAIC. . 24

4.1 Processing flow chart for thermal imagery from uncooled TIR cameras. . . . 26

4.2 Tool used to choose map from brightness temperature to digital numbers. . 27

4.3 Comparison between original sensor brightness temperature images and images after applying uniform map to digital numbers. 28

4.4 Sensor brightness temperature images after applying uniform map to digital numbers. 29

4.5 Tool used to find thermal camera temperature drift. 30

4.6 Graph of difference in temperature vs. difference in time. 31

4.7 Sensor brightness temperature images after compensating for drift. 32

4.8 CalCam target for thermal camera geometric calibration. 33

4.9 Diagram of ground-based thermal camera apparatus. 35

4.10 Diagram of thermal pool system. 37

4.11 Basic Discharge System for temperature pools. 38

4.12 **L** Discharge System for temperature pools. 39

4.13 Pressure Nozzle Discharge System for temperature pools. 39

4.14 Weir Discharge System for temperature pools. 40

4.15 Circulation patterns in the Basic System. 41

4.16 Thermal image for the Pressure Nozzle System. 41

4.17 Thermal image for **L** System. 42

4.18 Analysis area where pool temperatures were taken from. 43

4.19 The thermal mosaic acquired on June 9th 2013 from 450m AGL. 44

4.20 A ground thermal image of bare-ground taken from ground-based thermal camera. 45

4.21 Aircraft thermal pixels vs. ground thermal images (June 17th). 45

4.22 Thermal aircraft image of cool temperature pool. 48

4.23 Aircraft thermal pixels vs. pool temperature samples (June 17th). 48

4.24 Aircraft thermal pixels vs. Landsat thermal pixels (June 17th). 49

4.25 Aircraft thermal pixels vs. Landsat thermal pixels (June 17th). 49

4.26 Aircraft thermal pixels vs. sample methods (June 17th). 50

5.1 The processing cycle for fish tracking. 56

5.2 Flight simulation system diagram. 57

5.3 UA system diagram. 60

5.4 Closed-loop heading controller. 65

5.5 The flower flight path used to collect flight data. 65

5.6 The two-dimensional, fourth-order polynomial model plotted with the test flight data. 67

5.7 Residuals of the flight data vs. the signal model. 68

5.8 Repulsive fractional order potential field ($1 \leq n \leq 5$). 70

5.9 Attractive fractional order potential field ($1 \leq n \leq 5$). 71

5.10 Potential field map for the Attractive Method. 72

5.11 Potential field map for the Repulsive Method. 73

5.12 Potential field map for the Offset Repulsive Method. 74

5.13 Potential field map for the Dual-offset Repulsive Method. 74

5.14 Map for the fish-tracking flight simulation. 75

5.15 Plot of UA position error in x and y. 77

5.16 Plot of wind magnitude and direction. 77

5.17 Plot of actual and measured ground speed. 78

5.18 Plot of yaw, heading, and wind direction. 78

5.19 Plot of measured and modeled signal strength. 79

5.20 Simulation results for the Repulsive Method. 79

5.21 Simulation results for the Offset Repulsive Method. 80

5.22 Tag position variance plot for the Offset Repulsive Method. 80

5.23 Simulation results for the Dual-offset Repulsive Method (2 UAs). 81

5.24 MC simulation with 1 UA using Repulsive Method. 83

5.25 MC simulation with 1 UA using Offset Repulsive Method. 84

5.26 MC simulation with 3 UA using Repulsive Method. 85

6.1 VIS-NIR mosaics and a classified image of *Phragmites Australius*. 87

6.2 A series of vegetation maps can be used for change detection. 88

6.3 VIS-NIR and thermal mosaics of two center pivots. 89

6.4 NDVI and LAI maps of two center pivots. 90

6.5 Chlorophyll maps of oats five weeks after germination and early flowering. . 90

6.6 Nitrogen maps of oats five weeks after germination and early flowering. . . . 91

6.7 Evapotranspiration maps of two center pivots. 91

6.8 VIS-NIR and thermal mosaics of river. 93

6.9 Thermal mosaic of river displayed over visual mosaic. 94

Acronyms

AGL	Above Ground Level
AOI	Area of Interest
BRMBR	Bear River Migratory Bird Refuge
BFT	Biotelemetry Fish Tracking
BT	Brightness Temperature
COA	Certificate of Authorization
CPS	Cyber Physical System
DEM	Digital Elevation Model
DN	Digital Number
FAA	Federal Aviation Administration
FOV	Field of View
FOPF	Fractional Order Potential Field
GPS	Global Positioning System
GCS	Ground Control Station
IMU	Inertial Measurement Units
ICI	Infrared Cameras Inc.
MP	Megapixels
NUC	Non-Uniformity Correction
NOTAM	Notice to Airmen
PF	Potential Field
RVM	Relevance Vector Machine
RC	Remote Control
TIR	Thermal Infrared
UAS	Unmanned Aerial System
UA	Unmanned Aircraft
USU	Utah State University

VIS-NIR	Visual (red, green, blue) and Near-Infrared
VLOS	Visual Line-of-sight

Chapter 1

Introduction

Remote sensing is a method of capturing information without physical contact. The freedom from this physical connection enables large amounts of data to be gathered quickly from a single point over a large area of interest (AOI). For this reason, remote sensing is commonly used to measure the surface of the earth which can include complex, dynamic, distributed systems. From the air (e.g. manned aircraft or satellite), large portions of the earth can be measured in a short period of time and used for many ecological applications including agriculture [1–7], wildlife management [8,9], vegetation management [10–12], stream and river management [13–15], and forestry [16–18]. To properly use this data it must be converted into the actionable information needed by end users; otherwise, the data and its acquisition would be worthless. Figure 1.1 shows a general diagram of the steps needed to acquire and process the remotely sensed data into actionable information. The end user is the one in need of information in order to manage and make decisions; for example, a farmer could use information about soil moisture to water more efficiently. The end user provides the AOI and a plan is built to acquire the data. If the data is being acquired from an aircraft, this plan would be a detailed flight plan. If a satellite is being used to acquire the data, a specific AOI might have to be requested or ordered if it has already been acquired. After the data is acquired, it is georeferenced and converted into Global Information System (GIS) data. Specifically for aerial imagery, the georeferencing step would include stitching the images together into one image and creating an orthorectified mosaic. The next step in Figure 1.1 is calibration. The placement of this block is to give a general idea of this process, and in practice the calibration can be performed before or after the georeferencing. The purpose of the calibration block is to convert the raw data from the sensor into data with physical meaning. For visual and near-infrared (VIS-NIR)

imagery, this is the process of converting physically meaningless digital pixel numbers into some absolute measure of light. Some sensors automatically calibrate the data they deliver and eliminate the need for the calibration step; however environmental effects (e.g. atmosphere, temperature, humidity) may distort the data and require additional calibration for accuracy. Even after the data is calibrated and scientific, this is still potentially useless to the end user. The last step prevents this by simplifying the data into information that the end user can act upon. For example if a farmer is given a map of soil moisture but has no way to program a center pivot accordingly, the map is useless to him. Instead, the soil moisture map should be simplified into an irrigation schedule which is something the farmer can use to take actions. This conversion from scientific data to actionable information is very important and can be very difficult since it is subjective; a farmer with a center pivot would need the data simplified differently than a farmer that uses flood irrigation.

The important thing to understand about The Processing Cycle for Meaningful Remote Sensing is that if one or more of the blocks are missing, success will not be possible and the end user will not get actionable information. If it is not possible to give the right information to the end user, there is no point in even acquiring the data. Therefore, it is important to have a good understanding of what the end user needs before attempting to acquire the data.

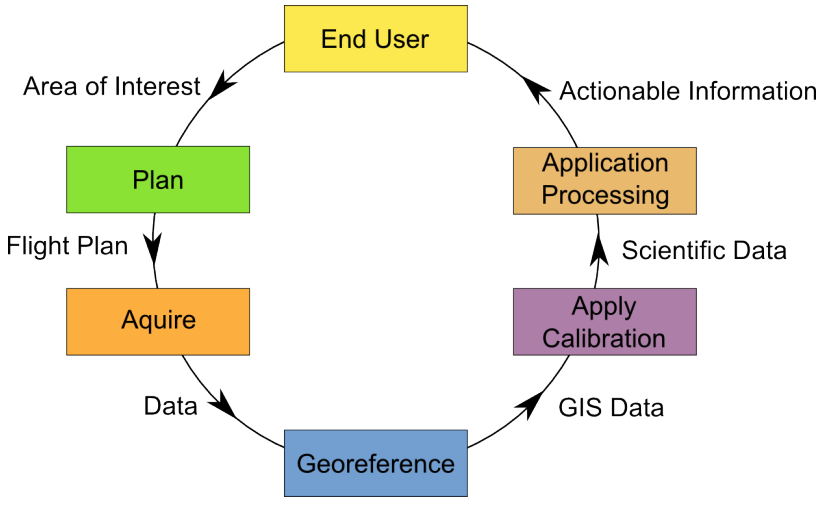

Fig. 1.1: The Processing Cycle for Meaningful Remote Sensing.

Many have been successful at closing this loop. For agricultural applications, VIS-NIR multispectral imagery has been used to estimate many variables including, yield estimation [1, 2], nitrogen deficiencies [3, 4], crop types [5], disease [6], and general health to help with applying herbicides and pesticides [7]. By adding thermal-infrared (TIR) imagery, soil moisture and evapotranspiration have also been estimated [4,19]. In vegetation management applications, VIS-NIR imagery has been used to classify vegetation and help manage and remove invasive plant species which displace native vegetation and affect wildlife habitat [10–12]. For river and stream applications, monitoring and managing fish habitat is important for maintaining and sustaining native fish populations. VIS-NIR imagery has been used to map the river channel [13] and identify types of fish habitat while TIR imagery has been used to map river surface temperatures [14,15] for fish thermal refugia. In addition to using multispectral imagery for fish habitat, acoustic biotelemetry is another important form of remote sensing to track fish movement [20].

1.1 Unmanned Aerial System-Based Remote Sensing

The successful applications mentioned above were all acquired using either manned aircraft or satellite. The data acquired by these sources can include high costs, poor image resolution, inflexible acquisition times, and slow turn-around times. In order to deal with these shortcomings, many are turning to unmanned aerial systems (UAS) as an alternative platform for remote sensing [21–24]. Since many of these UAS are small, remotely sensed data can be obtained at a low-cost, quickly, and at high spatial and temporal resolution. However, the small (less than 20lbs), low-cost nature of these systems introduces problems that make it difficult to successfully deliver actionable information. This is most apparent in the small, low-cost navigation sensors (GPS and inertial measurement units (IMU)) which provide position and orientation information to the autopilot. Because they are small and low-cost, they tend to be less accurate than other systems used by manned aircraft and satellite. Even though their accuracy is enough to navigate the aircraft, they have enough errors to make georeferencing remotely-sensed data very difficult. In addition to these challenges with georeferencing, data quality is also a problem for low-cost, small, consumer-

grade cameras compatible with small UAS. In many cases, these sensors do not come with calibration information which is important for generating scientific data. Some have used larger UAS to carry expensive, scientific-grade sensors to provide actionable information to end users. Laliberte et al. [25] used a large UAS, and VIS-NIR imagery for mapping vegetation over rangeland. Berni et al. [22] looked at using thermal imagery for soil moisture and compared that to methods for soil moisture using VIS-NIR imagery. While quality scientific data was produced in both of these cases, large UAS (20lb takeoff weight) were used along with expensive scientific grade sensors.

1.2 Dissertation Contributions and Organization

One of the main contributions of this dissertation includes a complete description on how to calibrate imagery from consumer grade VIS-NIR and TIR cameras for small UAS and scientific applications. While other documents may contain some of these steps, this is the first document to include every step in detail for both VIS-NIR and TIR. Another important contribution in this dissertation is a presentation of novel surface temperature sampling methods to help calibrate the TIR imagery [26]. Comparisons are made between the different sampling techniques and a trusted source of remote sensing data: Landsat. The final major contribution details the conversion of raw data from a novel biotelemetry fish tracking (BFT) payload into scientific data (estimated location of a radio-tagged fish) [27]. In addition to presenting new, simple methods for multi-UAV navigation and radio source estimation, Monte Carlo analysis was used to take a detailed look into how much accuracy can be expected in real-world scenarios. Such an analysis has never been done before with biotelemetry and small UAS.

The small UAS used to gather the data is called AggieAir (Figure 1.2) and is described in Chapter 2. Each chapter thenceforth will outline the conversion process to scientific data for the three different payloads (VIS-NIR, TIR, BFT). Chapter 3 will show how VIS-NIR imagery is converted into scientific data for commercial-grade, point-and-shoot cameras. This process is already well established; therefore Chapter 3 will be a review of current practices. Chapter 4 will show how TIR imagery can be converted into surface temperature

using low-cost, microbolometer, uncooled, thermal cameras. In particular, Section 4.3 shows methods for surface temperature ground sampling and how these samples can be used to compensate the imagery for external disturbances. Chapter 5 will show how to complete The Processing Cycle for Meaningful Remote Sensing in real-time for BFT using a new payload recently developed for AggieAir. The topics in Chapters 3-5 are very different; therefore literature reviews and conclusions for each topic are provided in their respective chapters. Chapter 6 shows how these methods have been used to provide actionable information for applications in vegetation mapping, precision agriculture, and fish habitat mapping and how they are part of a Cyber Physical System (CPS). The final conclusion in Chapter 7 outlines the contributions given in this dissertation and gives suggestions for future work.

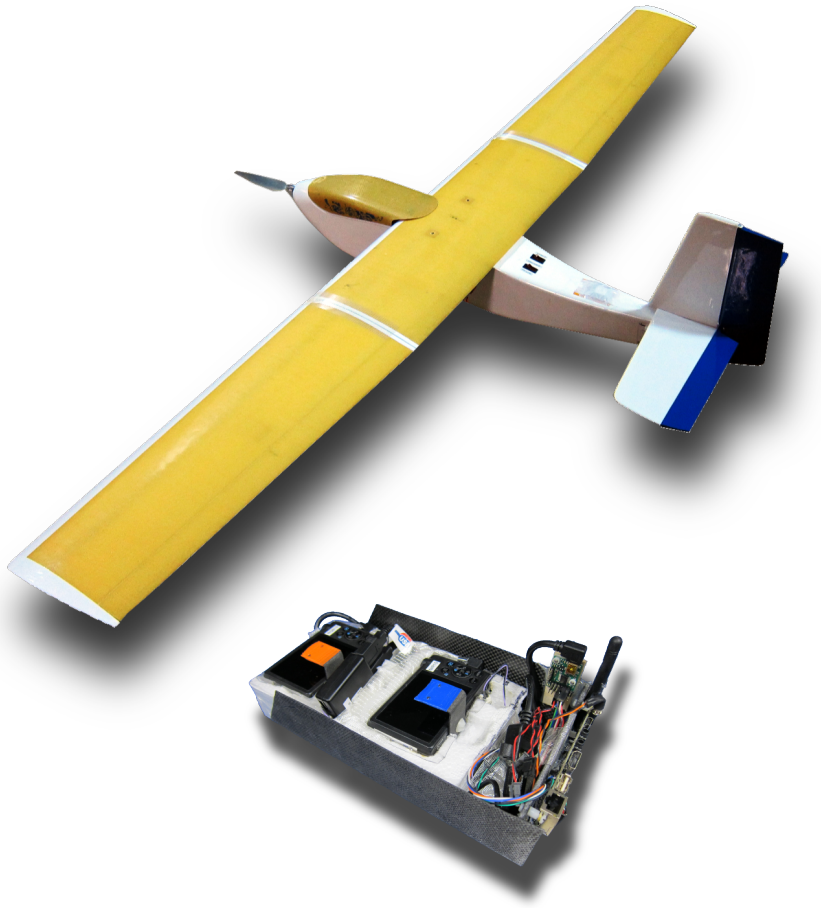

Fig. 1.2: The AggieAir-Minion aircraft with a VIS-NIR payload.

Chapter 2

AggieAir - A UAS-Based Multispectral Remote Sensing System

AggieAir is an unmanned aerial system (UAS) designed to carry camera payloads to acquire aerial imagery for ecological applications. Figure 2.1 shows the layout of the Minion airframe, and Table 2.1 shows specifications for the AggieAir-Minion aircraft. The wings have a Clark Y airfoil built with EPP foam and wrapped with Kevlar. The fuselage is also constructed with Kevlar and holds the batteries, the payload, and the avionics (Figure 2.2). The aircraft is propelled using an electric brushless motor and can roll, pitch, and yaw by means of the ailerons, elevator, and rudder using electric servos. AggieAir also has flaps to help slow the aircraft down during landing. The motor and the servos are all controlled by the Paparazzi Autopilot (Figure 2.3). Through the autopilot, the aircraft can be flown autonomously or manually. In autonomous mode, Paparazzi controls the movement of the aircraft to follow a pre-programmed flight plan. In manual mode, a human operator controls the aircraft using a 2.4 GHz transmitter like any hobby radio controlled (RC) aircraft. The inertial sensors, which are used by the autopilot to navigate the aircraft, include a GPS module and an IMU. The data from these sensors are combined using the inertial encoder and sent to the autopilot and payload. While navigating the aircraft, Paparazzi sends important data to the Ground Control Station (GCS) using a 900MHz modem. Some of the data sent to the GCS includes position, orientation, battery voltage, and airspeed. This 900MHz communication channel is also used by the GCS to send the aircraft high level commands (e.g. return home, execute the main flight plan, increase/decrease altitude, etc.).

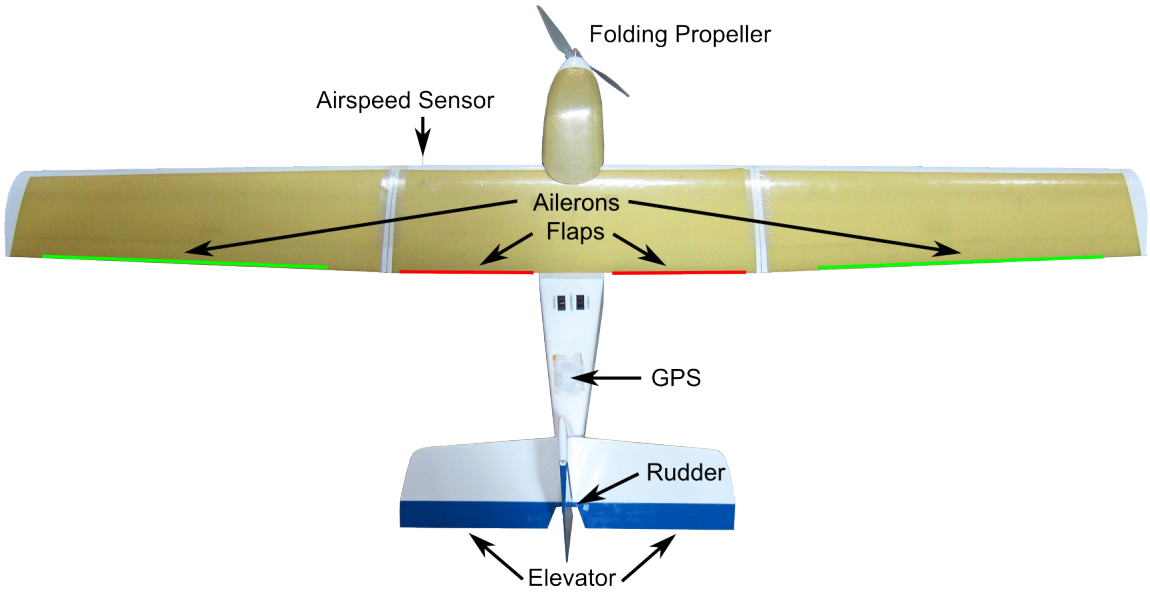

Fig. 2.1: AggieAir-Minion airframe layout.

Table 2.1: Specifications for the AggieAir-Minion aircraft.

Flight Duration	45-60min
Maximum Takeoff Weight	14 lbs
Wing Span	8 ft
Flight Altitudes	700-3200 ft
VIS-NIR Resolution	2.5-12 inches
Thermal Resolution	12-60 inches
Flight Area Coverage	3 miles^2
Flight Linear Coverage	5-10 miles

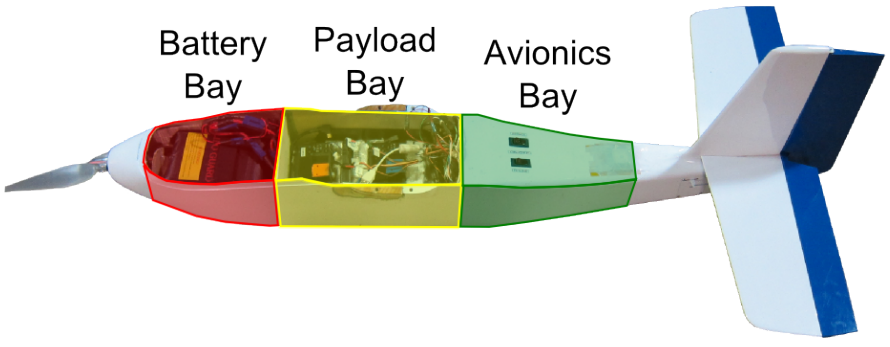

Fig. 2.2: AggieAir-Minion fuselage layout.

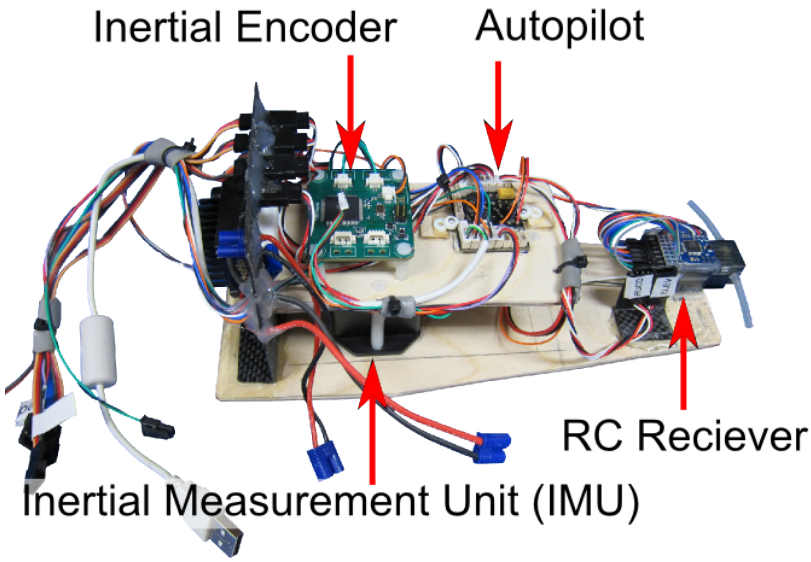

Fig. 2.3: AggieAir-Minion avionics layout.

2.1 Launching and Landing

A 50×100 yard strip of clear land is needed for successful autonomous takeoff and landing. Manual operation can be used for takeoff and landing in smaller areas or if the pilot prefers. A grassy field is ideal for landing however a dirt field or road will also work.

AggieAir uses a 20' bungee for takeoff. As Figure 2.4 shows, one end of the bungee is staked into the ground and the other end is attached to a hook underneath the aircraft. Once the bungee is stretched to a length of 100', the aircraft is released and launched into the air. While accelerating and gaining altitude, the autopilot follows a line beginning from the point at which it was released and extending to the known GPS location of where the bungee is staked into the ground. Once the aircraft flies past this bungee location, the bungee is disconnected from the hook and the autopilot turns the throttle on. With the throttle engaged, the aircraft continues to fly straight until it reaches a preset altitude and ground speed. At this point, the autopilot moves on to the next command in the flight plan. If the pilot prefers to takeoff in manual mode, a similar procedure is executed manually.

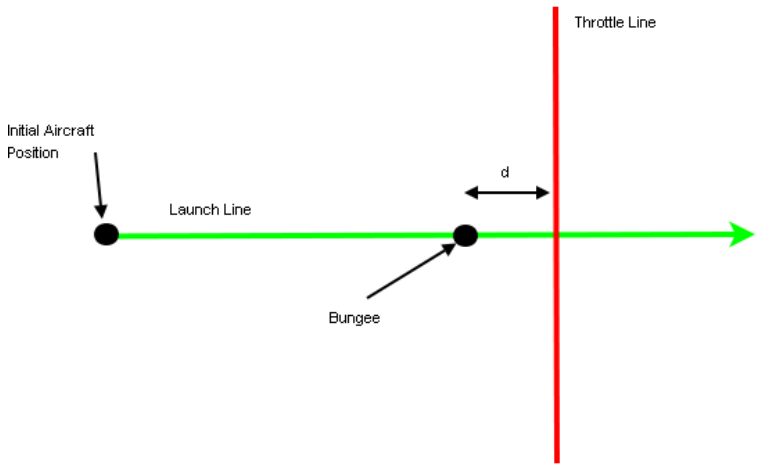

Fig. 2.4: Diagram of AggieAir auto-takeoff procedure.

Figure 2.5 shows a diagram of the auto-landing procedure. The autopilot first circles the aircraft around a given waypoint (typically called the AF waypoint) until it reaches a specific altitude; this altitude is usually set at 65ft above ground level (AGL). Once this altitude is reached and the aircraft is pointed toward the TD waypoint, the autopilot flies toward TD and slowly decreases altitude until it reaches ground level. The TD waypoint is commonly set about 150 - 200 yards away from the AF waypoint. As the aircraft reaches ground level, it has scrubbed off most of its speed and safely lands on its belly.

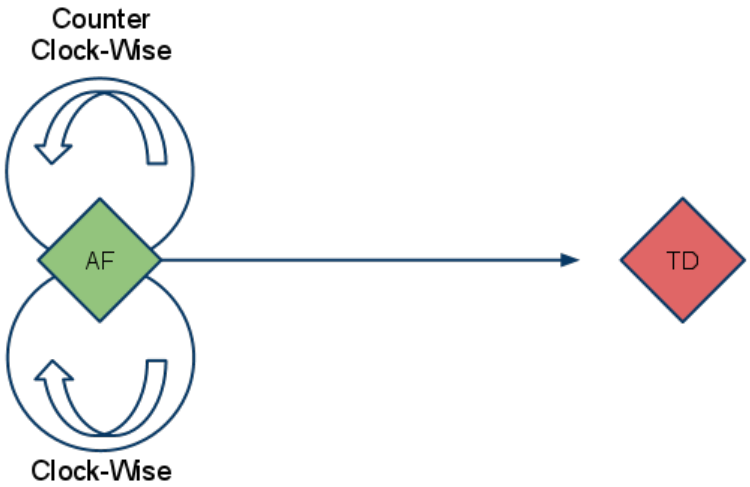

Fig. 2.5: Diagram of AggieAir auto-landing procedure.

2.2 Paparazzi Autopilot

The Paparazzi Autopilot has three modes of operation: manual, semi-autonomous, and fully-autonomous. The pilot can switch between these modes using a switch on the RC transmitter. If Paparazzi does not detect the transmitter, the default mode of operation is fully-autonomous.

When in manual mode, the RC receiver on the aircraft receives the command signals from the transmitter and passes them on to the Paparazzi board. The Paparazzi board then actuates the motor and servos according to these control signals. Even though the actuators are controlled through the Paparazzi board, the pilot is in complete control of the aircraft.

Like manual mode, control of the aircraft in semi-autonomous mode is also through the pilot and an RC transmitter at the GCS. However, the roll and pitch of the aircraft are stabilized using the autopilot and the IMU; the throttle is still manually controlled. For example, if the pilot pulls the stick to the right, the autopilot will interpret this as a specific positive roll value and will try to hold the aircraft in that orientation. If the pilot lets go of the stick, Paparazzi will hold the aircraft at zero roll and zero pitch. The semi-autonomous mode is used to help trim and tune the aircraft.

When in fully autonomous mode, Paparazzi flies the aircraft according to a preprogrammed flight plan. The flight plan contains waypoints and blocks which are used to tell the aircraft where to go and what to do there. A waypoint is a point of interest on the map defined by its location (GPS and altitude). The blocks use the waypoints to give specific commands to the autopilot. An example of a block is the Goto Block; the Goto Block simply tells the autopilot to go to a given waypoint. Another example is the Circle Block, which tells the autopilot to circle around a given waypoint at a given radius. Blocks can be set up to simply move to the next block when finished, to move to a different block somewhere else in the flight plan, or to repeat until the operator directs it to a different block. Exceptions can also be used in the flight plan to detect specific conditions and to redirect the aircraft accordingly. For example, an exception could be used to tell the autopilot to

come home if it gets too far away.

2.3 Payload

The basic AggieAir payload system includes the cameras, a payload computer, and a payload bay door (Figure 2.6). The cameras are controlled through USB by the payload computer. This computer tells the cameras when to take a picture, and records the position and orientation of the aircraft when the picture is exposed. The pictures are taken at equal time increments which are dependent on the altitude of the aircraft over the AOI. To protect the cameras, the payload bay door is opened by the payload computer while flying over the AOI and closed before takeoff and landing.

2.4 Ground Station

The ground station for AggieAir is operated with a two person crew: the pilot and the GCS operator (Figure 2.7). The pilot's job is to watch and manually fly the aircraft whenever needed while in sight. The pilot also inspects the aircraft before each flight, makes any necessary repairs, and launches the aircraft. The GCS operator programs the autopilot with its flight plan, sets up the payload, and monitors and controls the autopilot from the GCS.

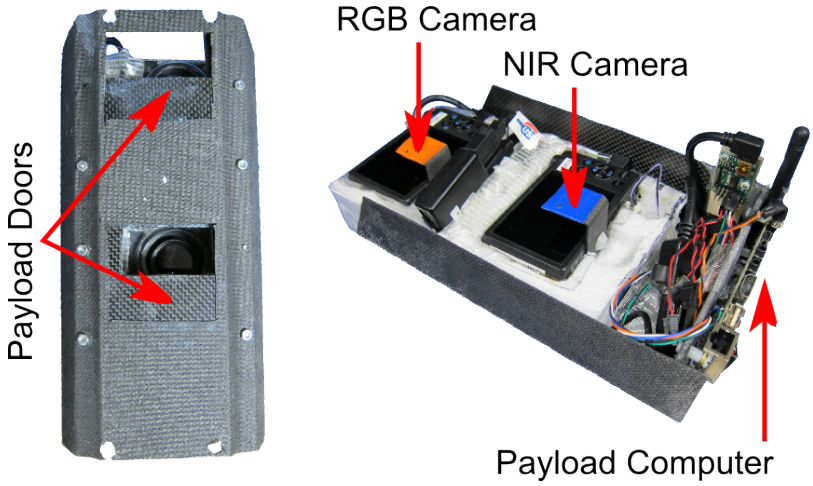

Fig. 2.6: Diagram of the AggieAir payload system.

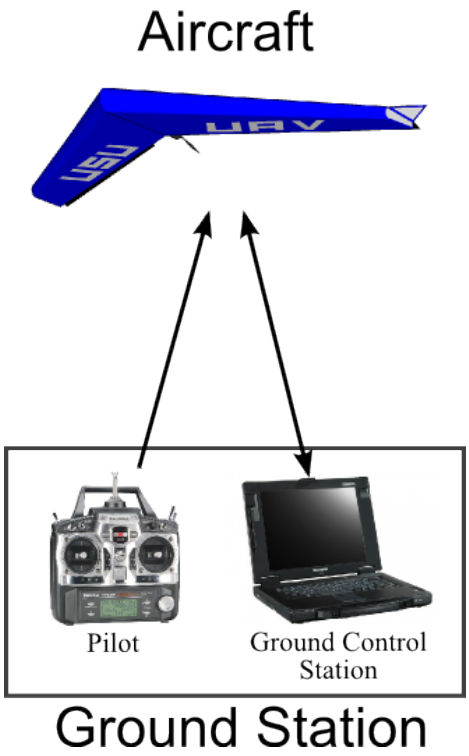

Fig. 2.7: AggieAir ground station diagram.

2.5 Paparazzi Ground Control Station

The Paparazzi GCS is used to monitor and control the autopilot while in flight or simulation. Figure 2.8 shows the layout of the GCS.

The 2D map gives the user an aerial perspective to help control and monitor the aircraft. The current aircraft position, the flight plan waypoints, the path of the aircraft, and the desired path of the aircraft are all displayed on the 2D map. To help visualize where the aircraft is, background images can be downloaded from Google maps under the Maps menu. The 2D map can be navigated using the mouse, the arrow keys, or by using the menus and buttons above the map.

Each strip on the GCS displays important telemetry data and has buttons for common commands for the autopilot. Examples of the telemetry data displayed on each strip include battery voltage, speed, throttle, current altitude, target altitude, and the autonomous mode. In addition to common command buttons (e.g. launch, kill throttle, altitude, and lateral

shift), the user also has the option to add more buttons which represent different blocks in the flight plan.

Each page in the notebook frame has multiple subpages which contain tools for monitoring and controlling the autopilot. The flight plan subpage is used to display all the elements in the flight plan. It also allows the user to change the current block being executed by the aircraft (highlighted in green). The GPS, PFD, and Misc subpages all display information about the aircraft. The GPS displays the number of satellites and the position error of the GPS signal, the PFD displays the orientation of the aircraft, and the Misc subpage displays other information such as estimated wind. The settings subpage contains autopilot settings which the user can change during the flight. These settings include the controller gains, the kill throttle, and other flight parameters.

The console frame displays messages and alerts the user when the status of the aircraft has changed.

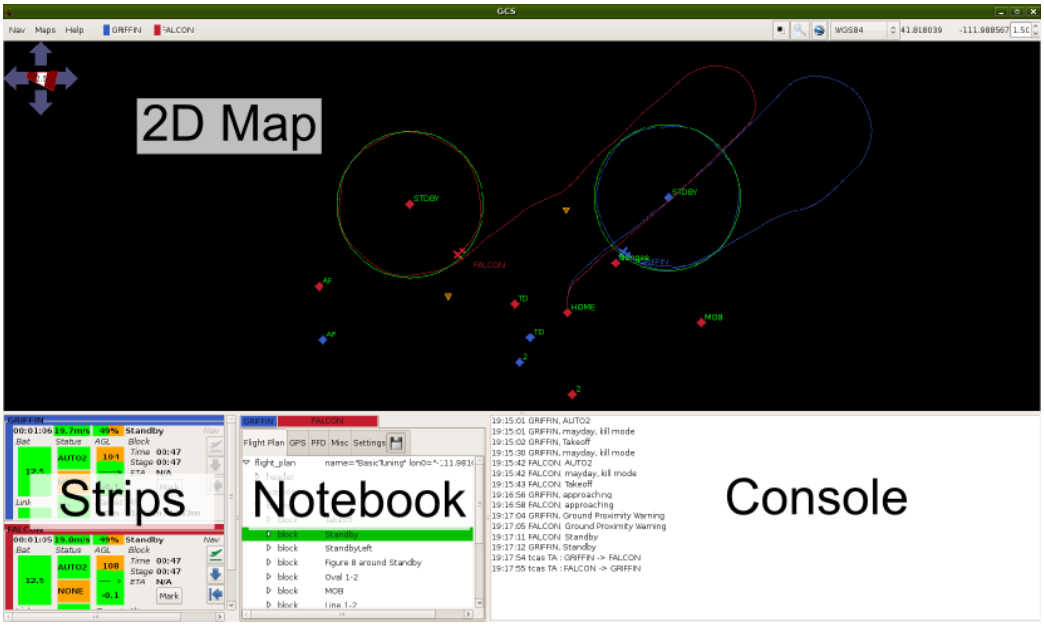

Fig. 2.8: Paparazzi ground control station software interface.

2.6 US Government Regulations and FAA Certificate of Authorization

In the United States (US), all flights of an unmanned aircraft (UA) are regulated by the Federal Aviation Administration (FAA). A UA is defined as any aircraft where a pilot is not on-board. This includes autonomous UAS aircraft, like AggieAir, as well as hobby RC aircraft. Since most RC hobbyists usually fly their aircraft for recreation, the FAA allows flight according to The Academy of Model Aeronautics National Model Aircraft Safety Code [28]. If a UA is flown for anything beyond recreation (e.g. to support a research project, profit, emergency response, etc.), at any altitude, the operator should apply for a Certificate of Authorization (COA) from the FAA [29]. Before using them to authorize UA flights, the FAA used COAs to give permission for aviation events such as airshows which required temporary alteration of current regulations for the period of the airshow. Applicants would state which regulations would need to be waived, and how they would mitigate the additional risks. The COA is used for UA in a similar way: since the pilot is not on-board the aircraft and cannot comply with the standard see-and-avoid responsibilities to avoid mid-air collision, these risks must be mitigated before the flight is allowed. To mitigate the risks of UA flights, the FAA has additional regulations and restrictions that must be satisfied in the COA application. Some of these restrictions include no UA flights at night, no UA flights over a populated area, no UA flights in class B airspace, one UA in the airspace at a time, and keeping the UA within visual line-of-sight (VLOS) at all times. There are also certain qualifications the crew must have; some flight operations require a pilot with a private pilot's license, others require a minimum of ground school [29]. In addition to the pilot, at least one observer must be included in the flight operations to keep the UA within VLOS at all times. Specific fail-safe procedures also need to be included in the COA application to explain what the UA will do if it looses link with the ground station or looses GPS link. The types of organizations who can receive a COA is also restricted. Only public entities like municipalities, police forces, state universities, military, etc. can receive a COA; all private companies (profit or non-profit) are excluded. FAA officials will also look at airworthiness of the aircraft in the COA application. For a public entity, this

is done using a signed airworthiness statement which contains a maintenance schedule and a preflight checklist to ensure airworthiness before each flight.

After a COA is approved, it is only valid for the specific aircraft, during specific times, at a specific location, and for the flight operation included in the application. Before flying the UA, the COA may also require the operators to file a Notice to Airmen (NOTAM) and to contact local airports and airspace managers in advance. Depending on the applicant's experience and the number of COAs in the queue, a COA may take between 2 to 9 months before it is approved. An example COA for AggieAir on the North Slope of Alaska is included in the Appendix along with the flight operations which were submitted with the application. This example is one of many COAs approved for the AggieAir UAS through state universities such as Utah State University (USU), Texas State University, and UC Merced.

2.7 Chapter Summary

This chapter presented the AggieAir UAS and how it is programmed, launched, recovered, and controlled. Government regulations were also briefly reviewed and insight was given into what is required to apply for an FAA COA. However, this only covers the first two steps in the Processing Cycle for Meaningful Remote Sensing. There is no value in a UAS with a camera unless the rest of the cycle can be completed. The following chapters will detail how to make sense of the remotely sensed data, specifically, to georeference and calibrate the data from the UAS.

Chapter 3

Visual Near-infrared Imagery

Many scientific VIS-NIR cameras are developed either for aerial imaging from a manned aircraft or for industrial use. The cameras developed for aerial imaging from a manned aircraft commonly have high quality optics and high resolution; however, they also tend to be very large, heavy, and expensive which does not work with small UAS. There are also small, less-expensive aerial imaging cameras which are more compatible with small UAS. Laliberte et al. [30] used the Mini MCA-6 multispectral camera on the BAT3 UAS to map vegetation over a rangeland. The MCA-6 is small and designed to output scientific data; however it is still costly and has a coarse resolution (1.3 megapixels (MP)). Others have also used the MCA-6 for UAV remote sensing for its data quality [31, 32]. Small industrial cameras could work for UAS aerial imaging; however they are generally designed to produce video and can be very expensive at high resolution. Another type of camera available for small UAS are consumer-grade cameras (personal point-and-click cameras); these cameras are ideal because they are small, low-cost, and have high resolution (8-12 MP) [25, 33]. However they can be difficult to control and synchronize with the inertial data from the aircraft [34]. In addition, using consumer-grade cameras for scientific applications can be difficult since they do not come with the calibrations performed on typical remote sensing VIS-NIR cameras [35]. This chapter will show how the data from consumer-grade cameras can be processed and converted into quality scientific data, and used to collect multispectral VIS-NIR imagery. Figure 3.1 shows a flow chart of this processing stream.

3.1 Radiometric Calibration

The first processing step in Figure 3.1 is radiometric calibration. When most digital cameras capture an image, the intensity of light from each pixel within the image is rep-

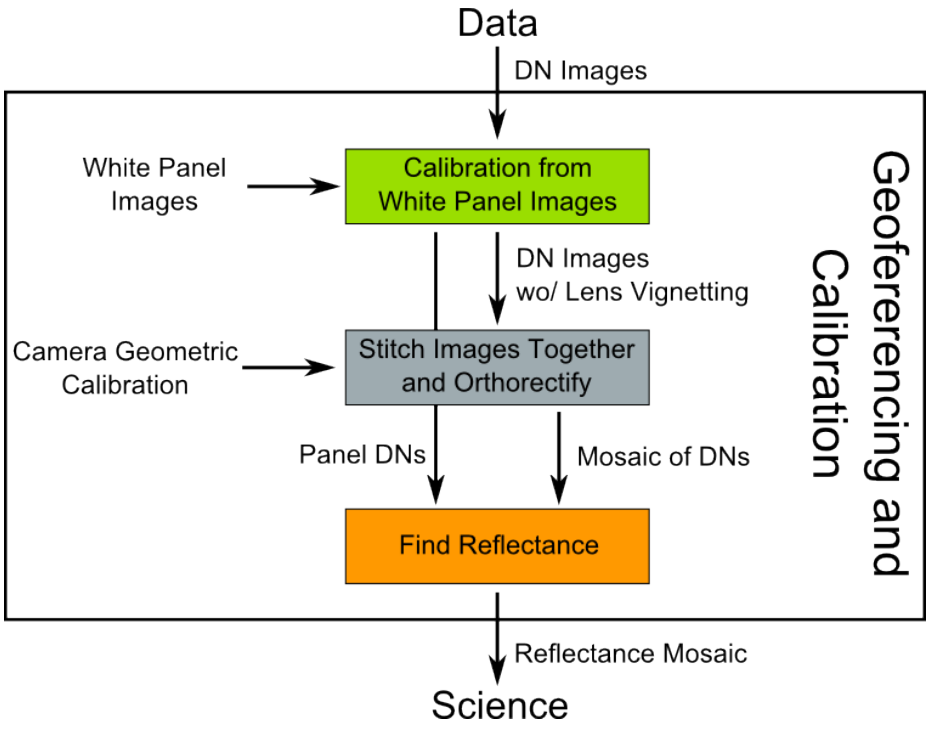

Fig. 3.1: Processing diagram for VIS-NIR imagery.

resented by a digital number (DN). The light represented by the DNs is relative and does not have absolute physical meaning, therefore radiometric calibration is needed to convert the DNs to an absolute measure of light. The measure of light which VIS-NIR imagery is commonly converted to is reflectance [36]. As Figure 3.2 illustrates, the reflectance is the ratio of light reflected from any surface (like the earth) versus the light reflected by a Lambertian surface ($\frac{R_e}{R_l}$) when the two surfaces are under the same lighting conditions. A Lambertian surface is used to normalize the images because it reflects all light perfectly in all directions.

For consumer-grade cameras, there are many different methods to calibrate imagery for reflectance. Laliberte et al. [30] placed a black and white target (with known reflectances) on the ground and within the AOI to calibrate their aerial images. The reflectance of the targets were measured with a field spectrometer and a Spectralon reflectance panel. A similar method was used by Hunt et al. [37] except five colored targets (beige, gray, green, red, and black) were used instead of one black and one white. Ritchie et al. [35] took

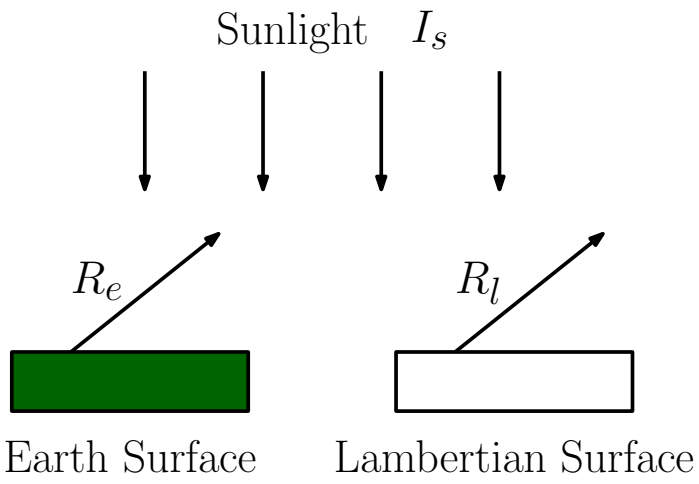

Fig. 3.2: Reflectance factor explanation.

pictures of a Gretag-Macbeth ColorChecker before the flight instead of using targets on the ground.

AggieAir uses a simple calibration method that can easily be applied to any consumer-grade camera [38]. Setup time is short and ground targets are not required. The only additional data collection needed for this method is a picture of a Lambertian surface before and after the flight. This process is shown in Figure 3.3 using a Spectralon Reflectance panel. The cameras used to take the picture of the panel are the same cameras used to collect the aerial imagery. In addition, the camera settings (exposure, f-stop, ISO, etc.) should be the same for both the panel images and the aerial imagery. This causes an issue because the ideal settings for the aerial imagery will often overexpose the images over the panel. Therefore, neutral-density filters are used on the cameras while taking pictures of the panel to darken the image and prevent it from overexposure.

As Figure 3.1 shows, the panel image is also used to remove lens vignetting. Figure 3.4 shows a picture taken over the reflectance panel; the color is stretched to show an example of this distortion. After the panel image is used to correct each aerial image for lens vignetting, they are stitched together and orthorectifed into one large mosaic. The vignetting is also removed from the panel image and the DNs are averaged and used with Equation (3.1) to convert the mosaic from DNs to reflectance. In Equation (3.1), DN_I are the DN pixels

from the aerial mosaic, DN_P is the average DN value of the panel, R_I are the reflectance pixels for the reflectance mosaic, and $R_P(\theta_z)$ is the reflectance factor for the Spectralon Reflectance panel. The reflectance factor for the panel is a function of the sun zenith angle (θ_z) and is calibrated using a radiometer. It is important to include the reflectance factor since the panel is not a perfect Lambertian surface.

$$R_I = \frac{DN_I}{DN_P} R_P(\theta_z) \tag{3.1}$$

Fig. 3.3: Taking a picture of the white panel before and after flight.

Fig. 3.4: The picture of the white panel after stretching the contrast.

3.2 Geometric Camera Calibration

In order to accurately map each 2D image into 3D space, an intrinsic camera model is needed. This includes basic parameters found in the pinhole model (focal length, principal point, pixel width and height, etc.) and lens distortion caused by the shape and placement of the lens on the image sensor [39]. A popular tool to find the intrinsic camera model is the Camera Calibration Toolbox for Matlab [22, 40]. While this tool works well and is free with Matlab, it neglects tangential distortion and uses a checkerboard pattern as its calibration target (Figure 3.5). A more accurate calibration target uses circular features as control points instead of checkerboard lines [41] and is used by other tools like CalCam from Mosaic Mill (Figure 3.6) [42]. Multiple pictures are taken of the target from different angles and the control points are matched in each of the pictures and used to calculate the intrinsic parameters.

3.3 Creating Orthorectified Mosaics

After each flight, the aircraft may have acquired 300-400 images from each camera. Figure 9 shows a sample of these images. The quickest way to georeference these images is

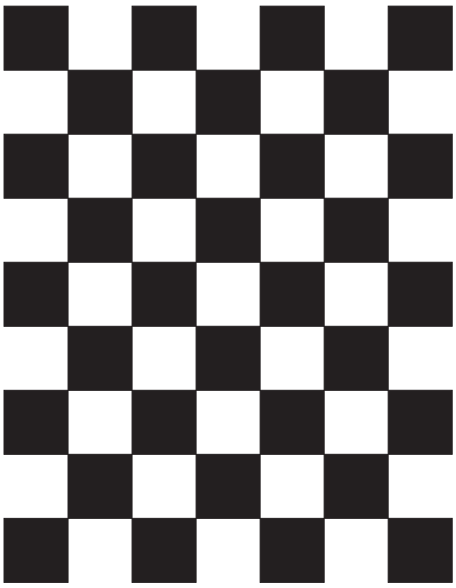

Fig. 3.5: Target for camera calibration toolbox for Matlab.

to directly georeference them using the position and orientation of the UAV when the image was exposed [43]. However as Figure 3.8 shows, errors in the position and orientation estimate created errors in the georeferencing accuracy. In addition, making use of each image individually would be very difficult and overwhelming. Therefore, creating an orthorectified mosaic of all of these images is a very important step in simplifying the data. For the highest accuracy, EnsoMOSAIC is used to orthorectify AggieAir imagery [42]. EnsoMOSAIC generates hundreds of tie-points between overlapping images and uses photogrammetry and block adjustment to refine the position and orientation information for each image thereby accurately georeferencing each image. EnsoMOSAIC also generates a digital elevation model (DEM) to compensate the imagery for distortions caused by changing elevations. The resulting product is the orthorectified mosaic shown in Figure 3.9.

3.4 Chapter Summary

This chapter explained how a consumer-grade digital camera can be used with a UAS to capture VIS-NIR images and use them to create multispectral maps for scientific applications. This process includes radiometric calibration to convert the digital pixels into a

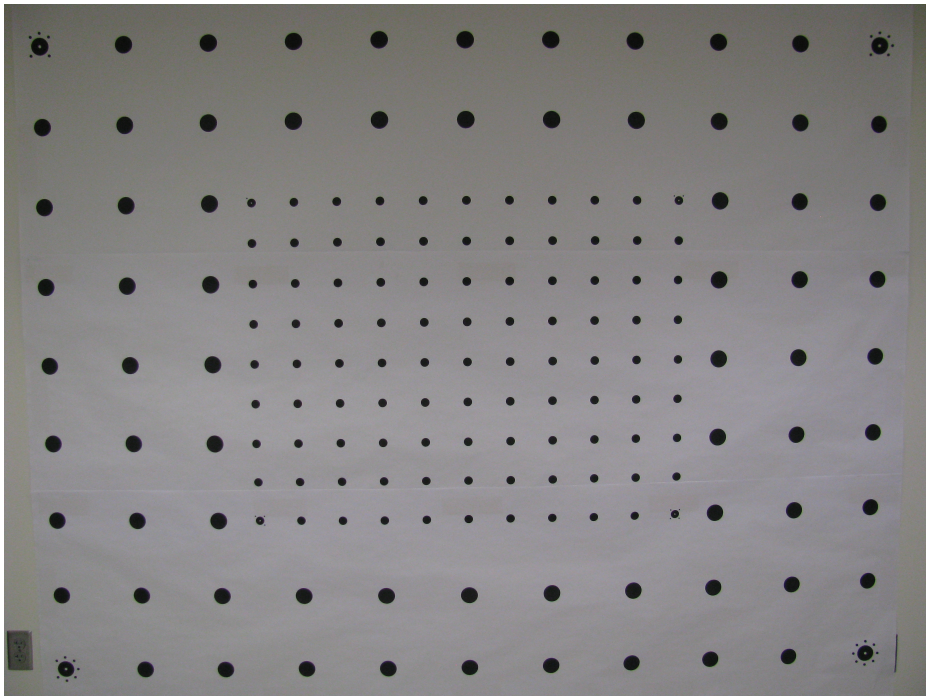

Fig. 3.6: The reference target for geometric camera calibration.

measure of reflectance, geometric calibration to help project the 2D images into a 3D space, and the stitching and orthorectification process to combine all of the images into one large mosaic. Different options for these processes were reviewed with current literature, but the process used with AggieAir was featured. Beneficial future research in this area would be to improve the speed of the orthorectification without sacrificing spatial accuracy. In many cases, the actionable information needed by the end user is very time sensitive and the orthorectification step, for accurate mosaics, is still very time consuming (one week to one month per flight). Another area of research would be to improve the radiometric calibration by finding the spectral response of the cameras using a monochromator [44].

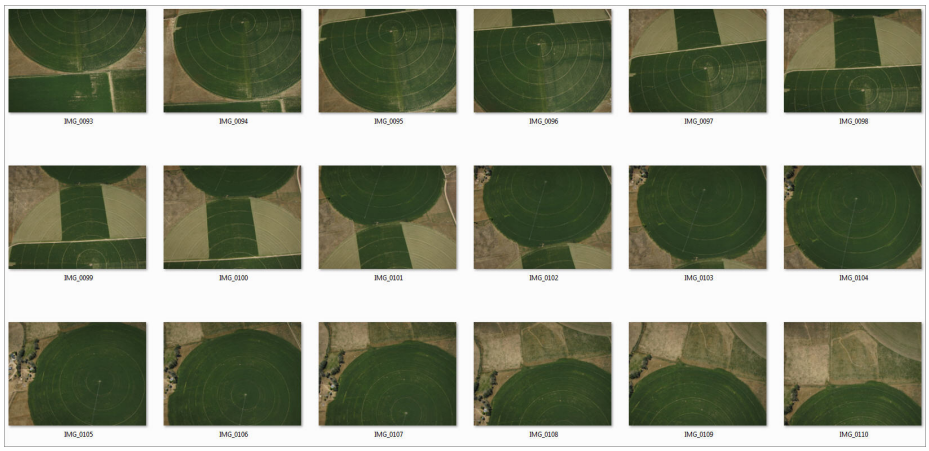

Fig. 3.7: Individual raw visual images captured from a flight.

Fig. 3.8: Individual images after direct georeferencing.

Fig. 3.9: Orthorectified mosaic using 200 images from AggieAir and EnsoMOSAIC.

Chapter 4

Thermal Imagery

Most thermal cameras used for remote sensing are cooled systems. While these cooled systems are very sensitive and accurate, they are also large, expensive, and consume a lot of power. As an example, Table 4.1 contains the specifications of the ThermoVision 1000 which is commonly used for remote sensing [45]. Because of their large size and power consumption, cooled thermal camera systems can not be used on small unmanned aerial platforms like AggieAir. For surveillance and military applications, microbolometer (uncooled) thermal cameras are widely used because they are smaller, less expensive, and consume less power than cooled thermal cameras [46, 47]. However, microbolometer thermal cameras are not as sensitive and accurate as cooled systems. In addition, many are not calibrated and measure only relative temperature. For most remote sensing applications, absolute surface temperature is necessary and requires a calibrated thermal camera. The thermal camera used with AggieAir is one of the smallest, low-power, microbolometer thermal cameras and comes from Infrared Cameras Inc. (ICI) [48]. Most importantly, this camera is calibrated so it outputs its data as absolute brightness temperature (BT). It also contains an image array with 640×480 pixels, and produces images with between 30cm and 1.5m ground resolution. However, there are still important processing steps necessary to deliver an absolute surface temperature mosaic. Figure 4.1 shows the processing steps needed to convert individual BT images from the camera to an absolute surface temperature mosaic.

4.1 Preparation for Orthorectification

Unlike the common visual camera, the thermal camera does not output the imagery with DNs. Instead the BT pixels from the thermal camera are in degrees Celsius sensitive to 0.1 degrees. Therefore before the thermal images can be orthorectified, they must be

Table 4.1: A thermal camera comparison for remote sensing.

	ThermoVision 1000	ThermoVision A40M	ICI 7640
Cooled/Uncooled	Cooled	Uncooled	Uncooled
Size	12.2" ×6.5" ×8.7"	8.1" ×3.6" ×4.3"	2.1" ×3.2" ×0.5"
Weight	17.6	3 lbs	0.5 lbs
Sensitivity	0.1°C	0.1°C	0.1°C
Accuracy	± 0.5°C	± 2°C or 2%	± 2°C or 2%
Resolution	640×480	320×240	640×480
Power	65W	<6W	<1W

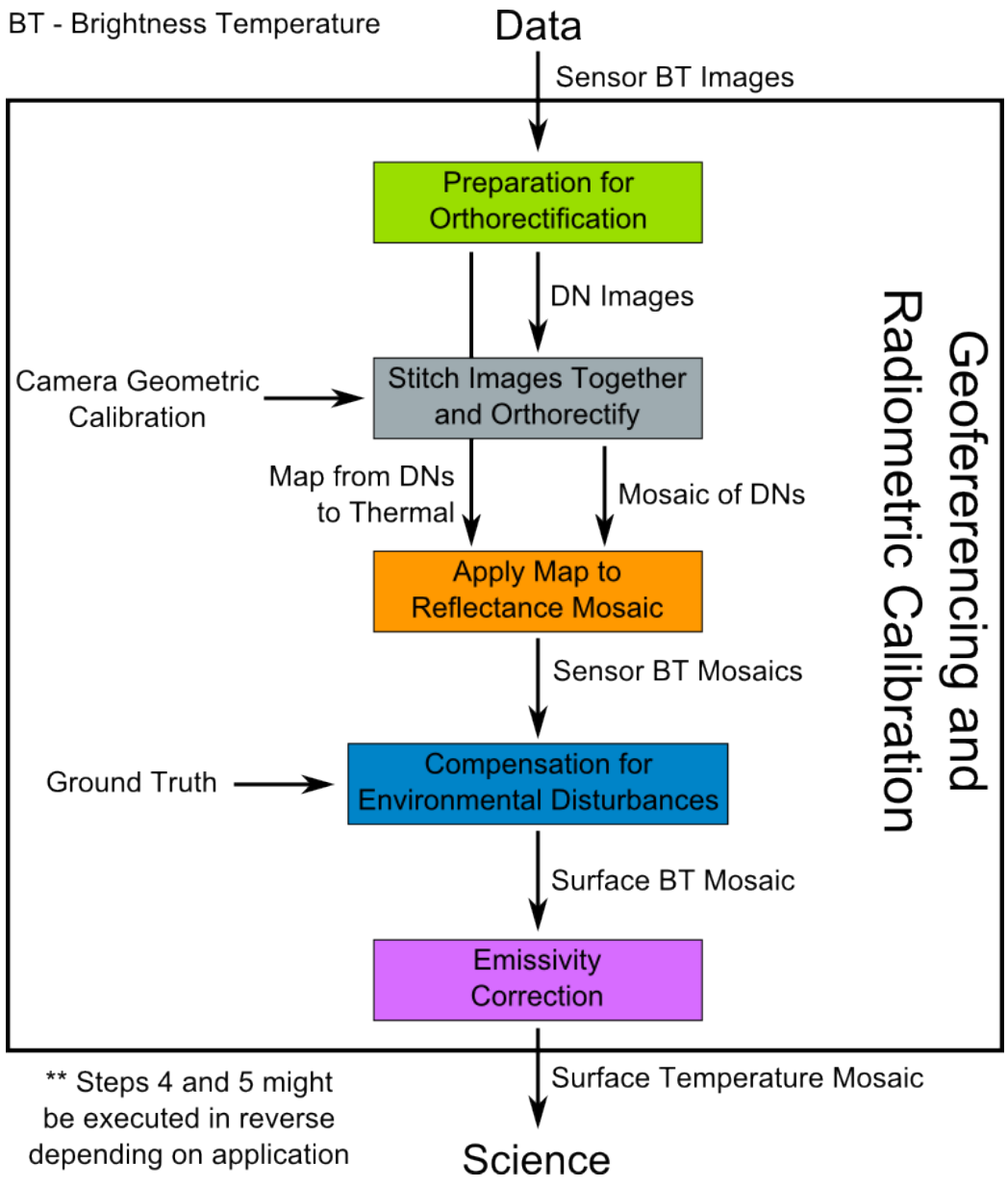

Fig. 4.1: Processing flow chart for thermal imagery from uncooled TIR cameras.

converted to 8-bit, gray-scaled DN images. Figure 4.2 shows the tool used to do this conversion. By default this tool uses the minimum and maximum temperature values in each BT image to generate their respective DN images. Since the minimum and maximum temperature values can change from image to image, it is not suggested to use this default setting to generate the DN images for mosaicing. The sliding bars on the dialog left of the image can be used to change the minimum and maximum temperature values that will be used to map temperature to DNs. After the range and the map is selected, it can be applied to all of the images so they are uniform. The range should be carefully selected around the temperatures found in the area of interest. If the range is too big, then data is lost to precision in the 8-bit images; if the range is too small, important data may be lost due to saturation outside the minimum and maximum temperatures. Selecting range is also important for successful orthorectification. If too many features are removed by saturating them out of the image, there will be less tie points for the orthorectification. Figure 4.3 shows a comparison between original images using the default temperature range and the same images after applying a temperature map. These images have been directly georeferenced to get a rough idea of how they fit together and even though the georeferencing is inaccurate, the figure still shows the effect of the temperature mapping.

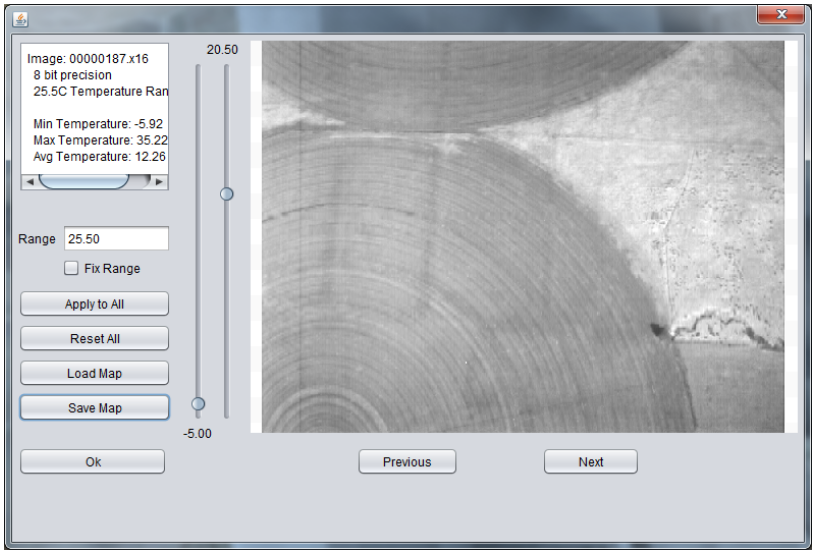

Fig. 4.2: Tool used to choose map from brightness temperature to digital numbers.

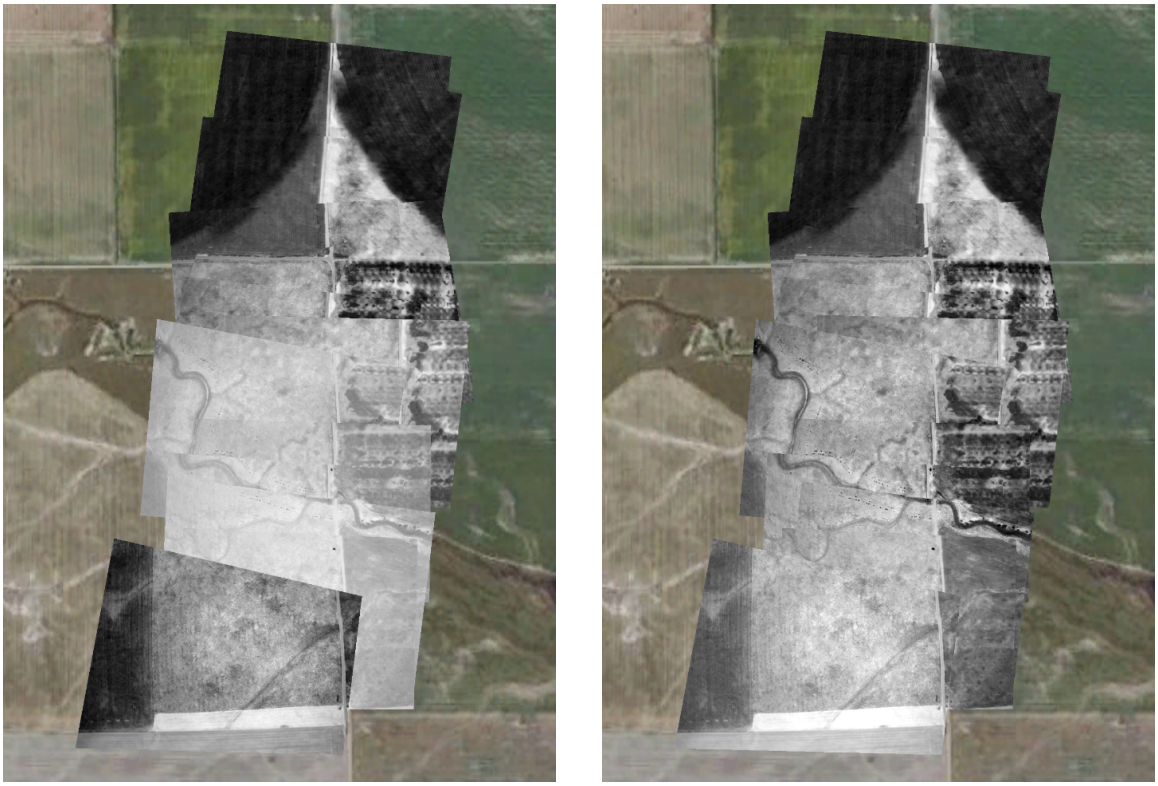

Fig. 4.3: Comparison between original sensor brightness temperature images and images after applying uniform map to digital numbers.

Before using the thermal camera to take pictures, it is important to make sure the core temperature of the camera is stable. If this is not done, the core temperature will drift over the flight along with the brightness temperatures given by the camera. Figure 4.4 shows an example of how this drift affects the brightness temperatures. Beginning in the top right corner of the map, the plane flew four sweeps across the AOI and ended at the top left. The images show that throughout the 30-minute flight the brightness temperatures slowly drift up making the surface appear hotter than it really is.

In order to find this drift and compensate for it, the tool in Figure 4.5 was created. With this tool, images with side overlap with other images from neighboring sweeps can be viewed. Similar features from the overlapping images are manually selected and with each point, the difference in temperature (ΔT) and time (Δt) are recorded. After finding many of these points, $\Delta T/\Delta t$ are plotted against the time of acquisition (of the later image)

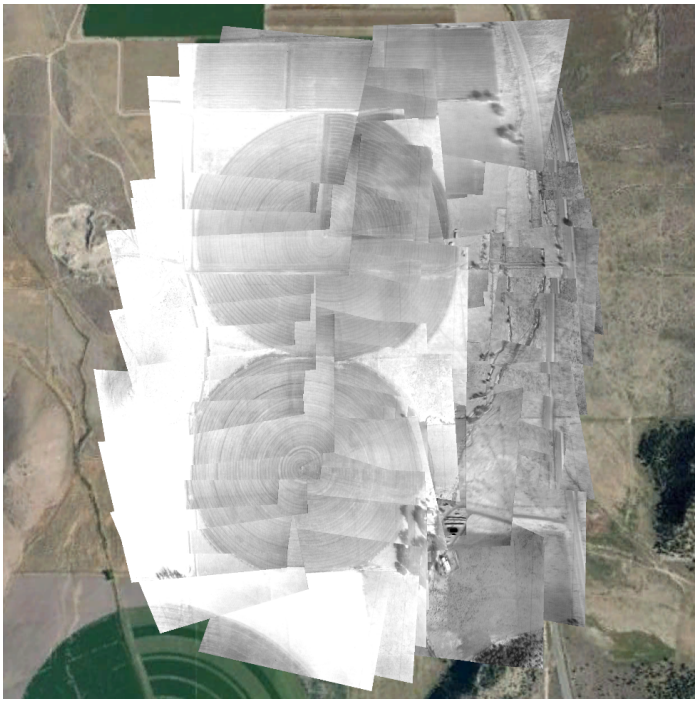

Fig. 4.4: Sensor brightness temperature images after applying uniform map to digital numbers.

as displayed in the graph in Figure 4.6. The blue line in Figure 4.6 shows the average of $\Delta T/\Delta t$ and represents the value of the drift rate. Therefore, the brightness temperature from each image can be compensated using the following equation where T_i is the initial temperature, T_c is the compensated temperature, and t is the difference in time between T_i and the first image:

$$T_c = T_i + \frac{\Delta T}{\Delta t} t. \tag{4.1}$$

Figure 4.7 shows the same images from Figure 4.4 after compensating them for the temperature drift. The uniform images show the success of the method.

4.2 Geometric Calibration

Like the VIS-NIR cameras, an intrinsic model for the thermal cameras is important to map the 2D image into a 3D space. However, calibrating a thermal camera is more difficult since it is sensitive to differences in temperature, not differences in color. Therefore

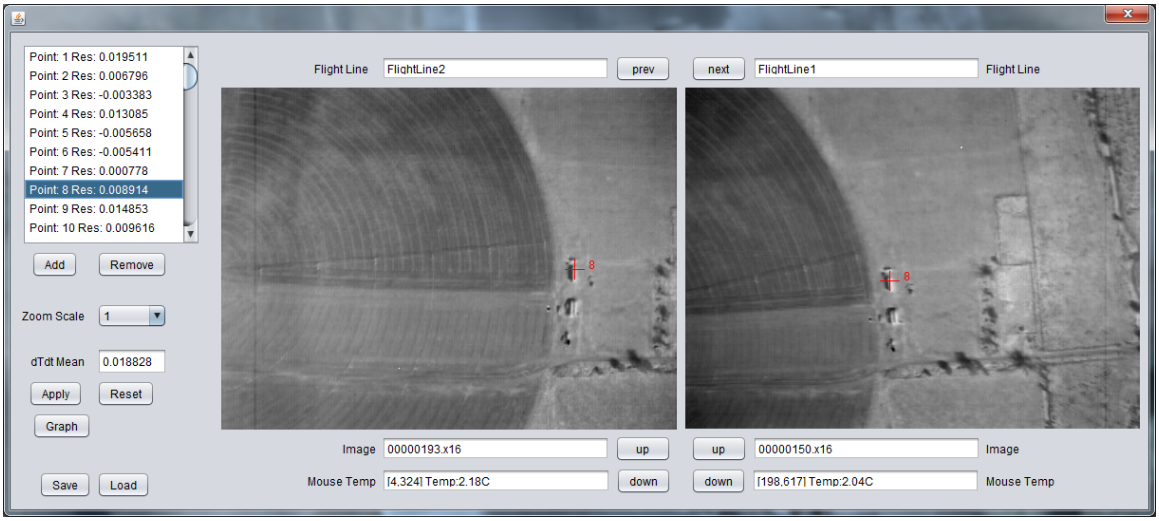

Fig. 4.5: Tool used to find thermal camera temperature drift.

a different type of target is needed to find the intrinsic model. Berni et al. [22] constructed a grid with resistive wires. When electricity was ran through them, the wires would heat up and the grid was visible through the thermal camera. This method cannot be used with the CalCam target since it uses dots instead of lines. To calibrate the thermal camera with CalCam, an aluminum wall is used with painted dots (Figure 4.8). When the aluminum wall is heated, the dots appear hotter than the bare aluminum (because of the difference in emissivity) and are visible to the thermal camera.

4.3 Compensate for External Disturbances

External disturbances like temperature, wind, and humidity all have an effect on the accuracy of the thermal camera to measure surface temperature. Ground surface temperature sampling can be used to check the accuracy of the thermal imagery and to help model and understand these external disturbances affecting the accuracy of the thermal camera [49]. Current methods to sample surface temperature use probes or thermometers to measure it directly, or point radiometers (hand-held infrared thermometers) to measure it indirectly. Prata [50] used a direct method and placed twenty-five thermometers throughout a 1km^2 area. Data from these thermometers were averaged and compared with the respective 1km^2 pixel from the thermal image gathered by the satellite. Some issues with

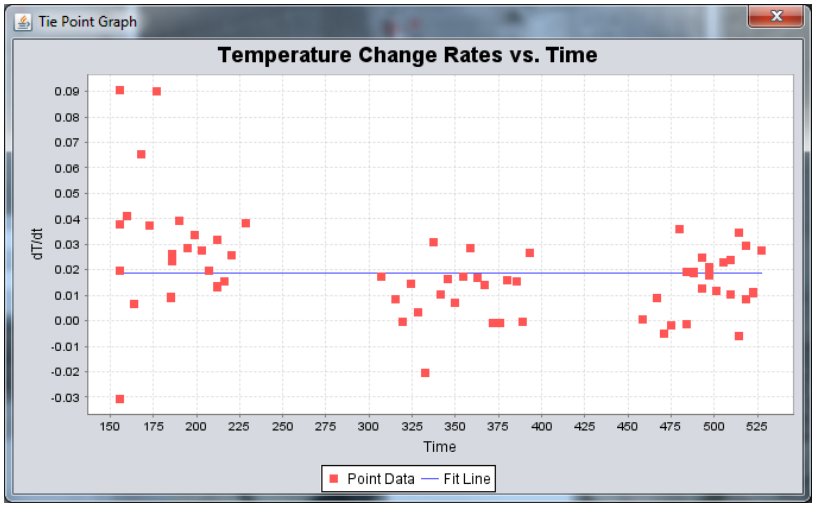

Fig. 4.6: Graph of difference in temperature vs. difference in time.

this type of sampling include measuring the temperature under or over the surface instead of at the surface, and representing an area measurement with multiple point measurements. However, it is difficult to sample surface temperature at such a large scale; there are not many other options. At a smaller scale, Wukelic et al. [51] calibrated the data from Landsat 5 (120m pixels) by choosing uniform sample areas, such as bodies of water and flat uniform land types (soil, grass, etc.), and characterizing their surface temperature with point measurements (using radiometers and thermometers). Torgersen et al. [45] captured thermal imagery over a river with a manned aircraft, and placed probes throughout the river to calibrate the thermal image. While all of these methods of sampling surface temperature were effective for their respective scales, they all made use of their large footprint to find uniform land areas or bodies of water to calibrate the thermal imagery. Such an option is not always available for small UAS remote sensing systems which cover small areas. For example, if a UAS is used for precision agriculture and captures thermal imagery to generate evapotranspiration maps, it is likely that the farm will not include bodies of water large enough to calibrate the thermal image. In a similar scenario, Berni et al. [22] used an unmanned helicopter to capture thermal imagery over a farm. Areas with bare soil and black and white targets were used to calibrate the thermal image using a point radiometer. While this method provided good results, it might be difficult to sample a wide range of

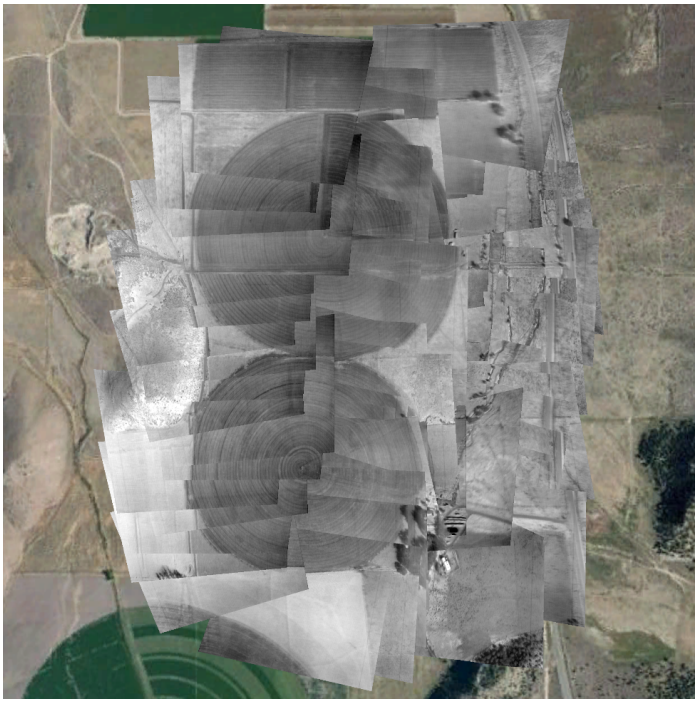

Fig. 4.7: Sensor brightness temperature images after compensating for drift.

temperatures. Also, the point radiometer has a small field of view and may not represent the larger pixel from the thermal imagery accurately.

There is a need to develop new ground temperature sampling methods which can easily and routinely be implemented with small UAS to compensate thermal images from low-cost microbolometer thermal cameras and understand the environmental disturbances that affect their accuracy. For the AggieAir system, these methods must accurately represent the surface temperature for an entire pixel ranging in size from 30cm to 1.5m. Two methods are evaluated in this section. The first method is similar to the method using the hand-held point radiometer, however a thermal camera is used instead. This delivers high resolution samples over an area large enough to cover four pixels to ensure at least one pixel is matched entirely by the sample. Before each sample, the thermal camera is calibrated using a black body. The second method uses bodies of water, with known and different temperatures, to compare with the thermal imagery taken by the aircraft. It is assumed that the temperature for each body of water is uniform. Temperature probes are used to measure the water

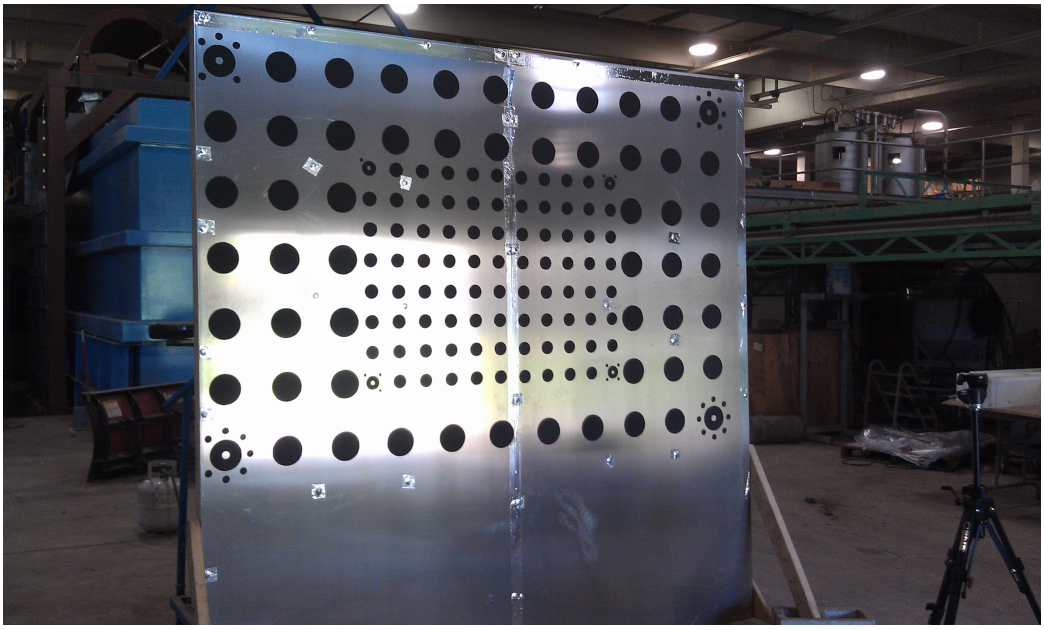

Fig. 4.8: CalCam target for thermal camera geometric calibration.

temperature of the pool and a radiometer is used to measure the surface temperature. To determine which of these methods is better, they were tested five separate times over a two-month period. Each test included a flight from AggieAir and was conducted on a day that coincided with a Landsat overflight; Landsat imagery was used to help evaluate the methods for accuracy.

4.3.1 Ground Sampling Methods

Before each flight, it is important to establish the size of each ground sample. Only one pixel is needed for each sample, however it is not possible to know where the location of this pixel will be before the flight. Therefore, the sample should cover an area of at least four pixels (2×2 pixels). This will ensure that at least one pixel is covered entirely by the sample. Pixels that are only partially covered by the sample should not be used. Table 4.2 shows a range of flight altitudes above ground and their respective pixel sizes and minimum sample area dimensions. The imagery acquired to test the methods was flown at 450m above ground. With a pixel size of 0.65m the minimum sample size is 1.3×1.3m; therefore a larger area of 1.7×1.7m was selected to include extra room for error.

Table 4.2: Flight altitude vs. sample area size.

Alt (m)	Res (m)	Sample Area (m)
200	0.30	0.60×0.60
450	0.65	1.30×1.30
600	0.85	1.70×1.70
1000	1.40	2.80×2.80

To ensure that valid comparisons can be made between the thermal cameras, the thermal radiometer, and Landsat, all emissivity correction is disabled (emissivity set to 1). Even though it is important for the actual surface temperature, it does not need to be considered except when comparing the aircraft thermal image with the temperature probes in the pools. In that case, the emissivity of water is assumed to be 0.98.

Ground-Based Thermal Camera Apparatus

Figure 4.9 shows the apparatus used to capture the surface temperature of the sample area with the thermal camera. To avoid confusion, the imagery collected by the ground-based thermal camera is referred to as ground thermal or ground pixels; the imagery collected by the aircraft is referred to as the aircraft thermal or aircraft pixel. The thermal camera is mounted to the end of a long boom which places it over the sample area. It is also connected to a laptop which is used to control the camera and take the pictures. A counterweight can be mounted on the other side of the boom to ensure stability.

The geometry of the apparatus is based on the camera field of view (FOV) and the desired sample area. The ICI 7640 has a 40 degree FOV. Based on this FOV, Table 4.3 shows the required camera height above ground for each flight altitude. To match the sample size previously selected, the samples presented in this section were collected at a camera height of 2.5m. Even though this camera apparatus is quite lengthy, it is built with carbon fiber rods to make it strong and easy to transport from sample to sample. While not being used, the apparatus can also be taken apart into 1.5m long pieces to make it manageable during transport.

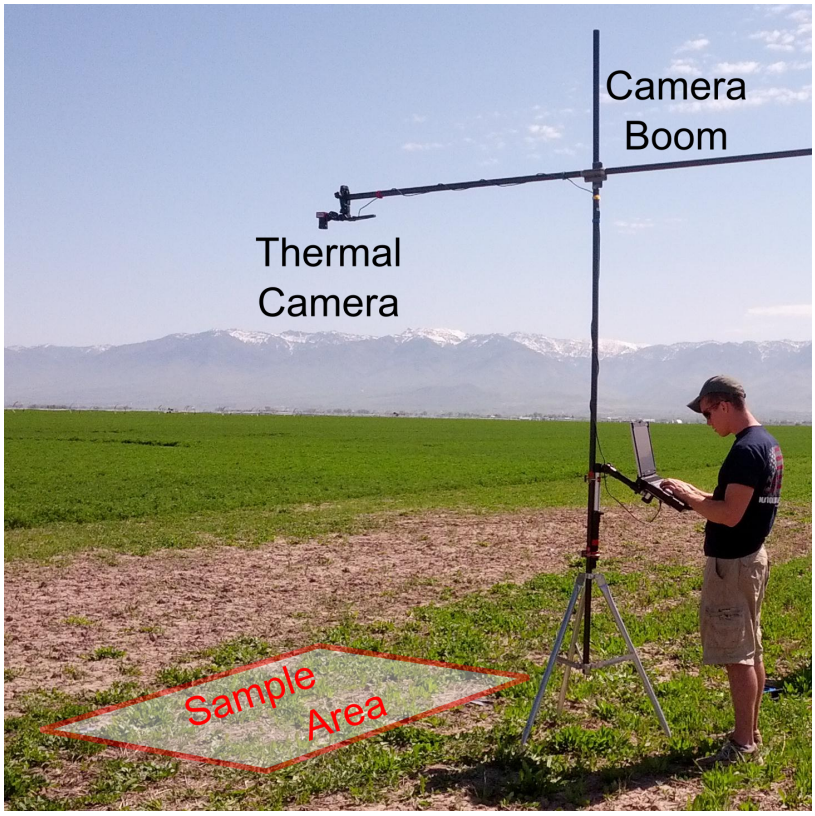

Fig. 4.9: Diagram of ground-based thermal camera apparatus.

Table 4.3: Flight altitude vs. ground camera height.

Alt (m)	Sample Area (m)	Camera Height (m)
200	0.60×0.60	0.9
450	1.30×1.30	1.95
600	1.70×1.70	2.55
1000	2.80×2.80	4.20

Ground-Based Thermal Camera Sampling

Before taking each picture of the sample area with the thermal camera, a non-uniformity correction (NUC) is performed and a picture is taken of an ambient black body. The picture of the black body is used to calibrate the ground thermal image of the sample area. Immediately after a picture is taken of the black body, the apparatus is rotated over the sample area. Small targets that can be seen by the thermal camera are then placed inside the sample area at each corner in the image; these targets are used to georeference the ground thermal image after the flight. After all four targets are placed, a picture of the

sample area is captured. Before moving to the next sample area, flags are placed in the center of the targets and their locations are measured with a survey grade GPS receiver.

Multiple locations for the ground-based thermal camera samples should be determined before the flight to spread the temperature range between samples as far apart as possible. The collection process should also be carefully timed close to the flight to reduce the difference between the fly-over time and the collection time.

Temperature Pools

Figure 4.10 shows an image of one of three temperature pools. Three pools are constructed in order to get a range of samples: cool, warm, and hot. The cool and hot water pools are actively cooled/warmed by pumping the pool water into a heat transfer reservoir which either contains ice to cool the water or is heated using a propane heater. After the heat transfer, the water is fed back into the pool using a discharge system.

Since the thermal camera only measures the surface temperature of water, the water in the pools only needs to be deep enough so that any tilt in the pool will not expose the bottom surface. After experimentation with the water depth, and looking at the required volumes, a depth of at least 2.5cm is recommended. Table 4.4 shows the amount of water needed for the various flight altitudes and sample areas. To test the pools and compare them with the ground-based thermal camera, three were built with a sample area of 1.7mx1.7m. Each pool was constructed with sufficient strength to hold 74kg of water; if the structure sags and deforms, this will cause non-uniform depth and areas might form where the bottom of the pools are exposed. Water-proof tarps were placed over the wood structure to prevent leaking.

Table 4.4: Flight altitude vs. camera height.

Alt (m)	Sample Area (m)	Water (liters)
200	0.60×0.60	9
450	1.30×1.30	43
600	1.70×1.70	74
1000	2.80×2.80	200

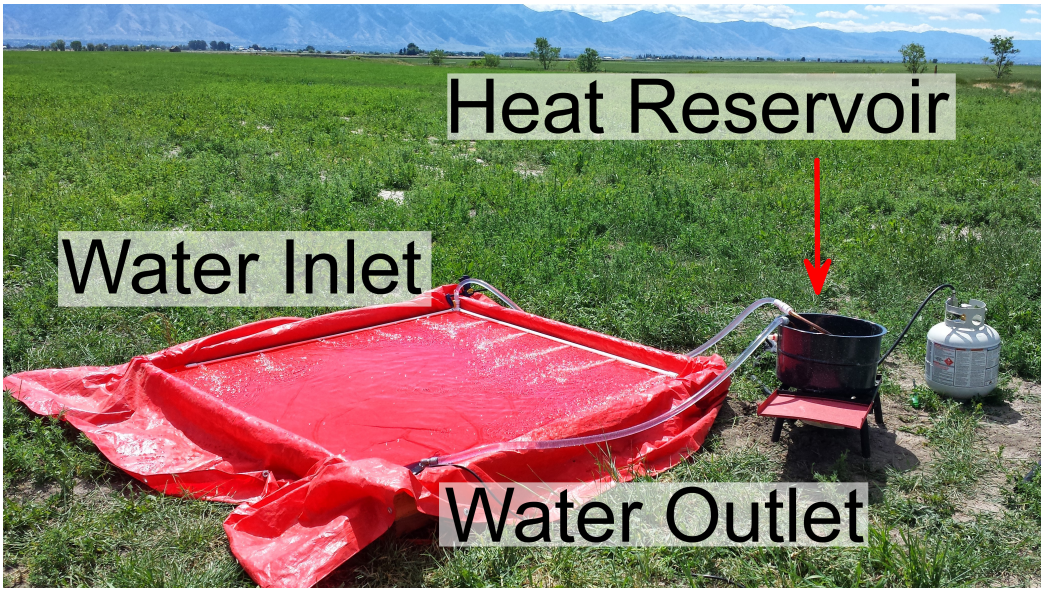

Fig. 4.10: Diagram of thermal pool system.

Two devices are used to measure the water temperature: a temperature probe and a thermal radiometer. The temperature probe is placed in the pool at setup and measures the temperature of the water body every minute for the duration of the flight. The thermal radiometer is used to measure the water surface temperature at ten different points over the pools right before the fly-over time. Along with this temperature data, the locations of the pool corners are measured with a GPS receiver to help determine their location in the aircraft thermal image.

Pool Discharge Systems

A vital part of the temperature pools is the system that cycles the water from the pool, through a heat transfer reservoir, and then back into the pool. While the body temperature of water is slow to change, the surface temperature changes easily and is very sensitive to wind. Therefore, the ideal discharge system keeps the surface temperature of the pool uniform by making sure the water is always moving and stirring. This section presents four discharge systems and evaluates them by how uniform they are able to keep the surface temperature of the pools.

The first discharge system (Figure 4.11) is composed of a straight PVC pipe that spans the side of the pool. A centered inlet and five outlets (each 6mm in diameter) are spaced evenly along its length.

The second discharge system (Figure 4.12) is much like the first except shaped like an **L** to take advantage of the pump located in the opposite corner. Each leg spans a side of the pool and has five outlets (10 in total) 3mm in diameter. The inlet is located where the two legs join together.

The third system (Figure 4.13) is also similar to the first system but incorporates three pressure nozzles instead of drilled holes. The nozzles are spaced to divide the pool into four equal segments. The pressure nozzles spray in a flat plane at 65° and are oriented parallel to the pool surface.

The fourth system (Figure 4.14) includes a series of weirs that split the pool into three sections: a small inflow area about 100mm across, a larger outflow area about 300mm across, and a large central area. Each area is separated by a wier that allows water to flow over it across the entire length of the pool. The inflow weir is higher than the outflow wier and allows water to flow with a constant velocity across the width of the pool from the inflow area to the outflow area. To test the fourth system, each weir was made from a straight piece of wood planed down to provide a smooth, even surface. Vertical adjustments were made with two leg screws and horizontal stability was provided by vertical brackets into which each weir was slid.

Evaluation of the Pool Discharge Systems

To evaluate each discharge method, a thermal camera was mounted on the camera

Fig. 4.11: Basic Discharge System for temperature pools.

Fig. 4.12: **L** Discharge System for temperature pools.

Fig. 4.13: Pressure Nozzle Discharge System for temperature pools.

apparatus and positioned over one of the pools. Each discharge system was setup, turned on, and allowed to stabilize. After a NUC was performed on the thermal camera, it was then used to find the standard deviation of the pool temperature every 2 seconds for a 20 second period. This set of standard deviations were averaged, and the test was repeated with a fan blowing across the surface. It was important to also test each discharge system with the fan to see how resilient they would be against wind. Table 4.5 shows the results of the pool discharge system test. Both the **L** System and the Pressure Sprayer Nozzle System showed improvements over the Basic System. It is likely that the **L** System benefited from providing a degree of symmetry with the pool. The Pressure Sprayer Nozzle System slightly outperformed the **L** System using only 3 exit points instead of 10. The marginal performance gain of the Pressure Sprayer Nozzle System over the **L** System of 1.5% in no wind conditions increased to 6.4% in wind conditions. This shows that the Pressure Nozzle System would be more robust in windy conditions.

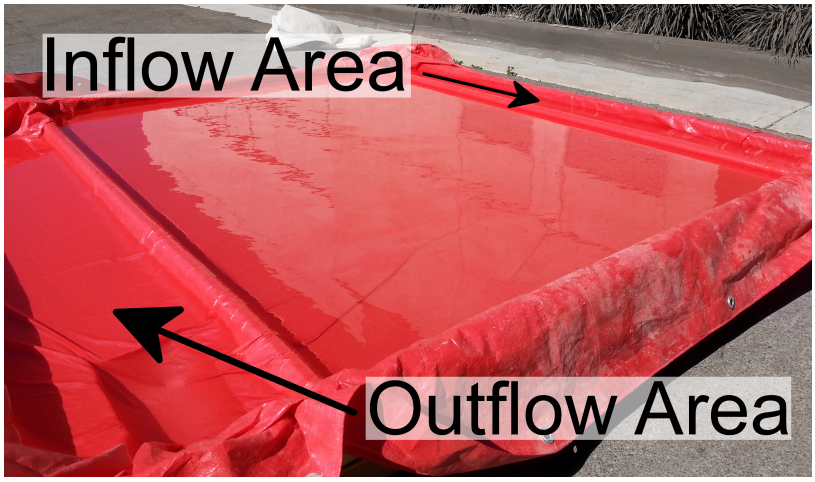

Fig. 4.14: Weir Discharge System for temperature pools.

Ideally, the water should flow in a direct path from the outlet to the inlet. In both the Basic System and the Pressure Nozzle System, currents formed that curved away from the outlet and returned to the inlet side of the pool. This effect is very clear in the Basic System (Figure 4.15) where this recirculation causes the two outlet holes on the right side to be pushed apart. This was less of an issue for the Pressure Nozzle System (Figure 4.16), and the **L** System avoided this recirculation effect completely (Figure 4.17).

The Weir System was never fully tested due to the non-uniformity of flow across the entire surface of the weir. Sections were left uncovered by water that compromised the test. There were two reasons for this. The first is that the wooden wiers were not stiff enough and allowed some sagging to occur. This could be fixed by adding more adjustable legs but was not attempted due to the difficulty of accessing the legs to make adjustments while the pool was full of water. Alternately, a stiffer material such as metal could be used. The second problem is that a smooth surface covering the weirs could not be obtained due to

Table 4.5: Standard deviation of temperature distribution for pool discharge systems.

Configuration	StdDev (°C)	StdDev w/Fan (°C)
Basic system	0.546±0.173	0.640±0.202
L system	0.358±0.113	0.398±0.126
Pressure Nozzle	0.350±0.111	0.358±0.113
Weir System	-	-

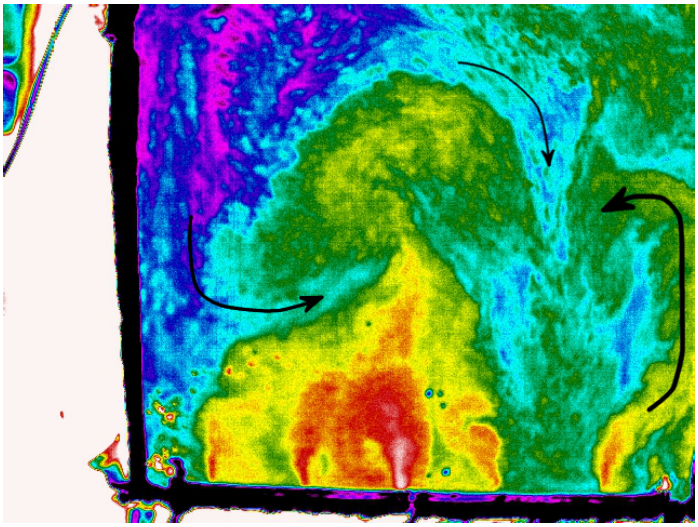

Fig. 4.15: Circulation patterns in the Basic System.

the thickness of the tarp that was used to provide water proofing. The pumps used must be submerged and a hole was cut into the floor of the pool. The tarp was then pushed down into the hole providing a pool of water deep enough for the pump to sit in. The close proximity of this hole to the weir kept the tarp from staying smooth over the wier while also providing an area deep enough for the pump. This could be fixed by extending the length of the pools allowing for more separation from the wier and pump, or a more pliable

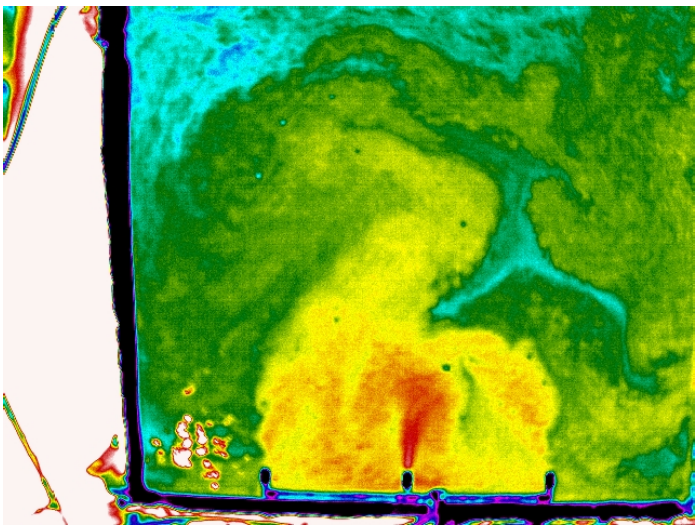

Fig. 4.16: Thermal image for the Pressure Nozzle System.

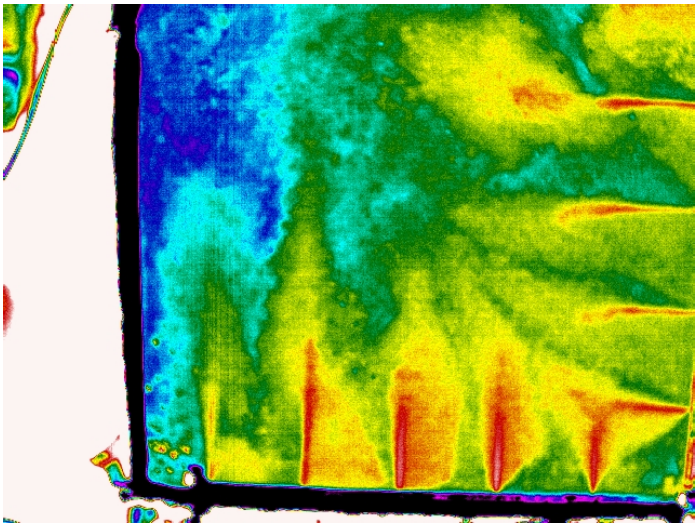

Fig. 4.17: Thermal image for **L** System.

material could be used for water proofing. None of these modifications were made because the system would have become too complex for the scope of the project and the simpler methods (e.g. the **L** and Pressure Nozzle Systems) were already performing well.

As shown in Figures 4.15, 4.16, and 4.17, the thermal camera captured an area larger than the pool and required that an analysis area be defined through software which only included the pool. The analysis area was set to include as much of the pool as possible. However, the physical body of the discharge system was not included. This was especially important in the Pressure Nozzle System where the low emissivity of the metal on the pressure nozzles caused them to show up as very cold in the thermal imagery. The analysis area was reduced further due to the reflection from the sun. This reflection can be seen in the bottom left corner of the thermal images but is especially clear in the Pressure Nozzle System (Figure 4.16). Several locations for the camera apparatus were tested, but movement from the water surface caused reflection regardless of position. Eventually the analysis area was shifted to the right to exclude the effects of the sun reflection. This shift also avoided the cooler water that collects in the upper left corner before it is cycled back into the thermal reservoir. Figure 4.18 shows the final location of the analysis area.

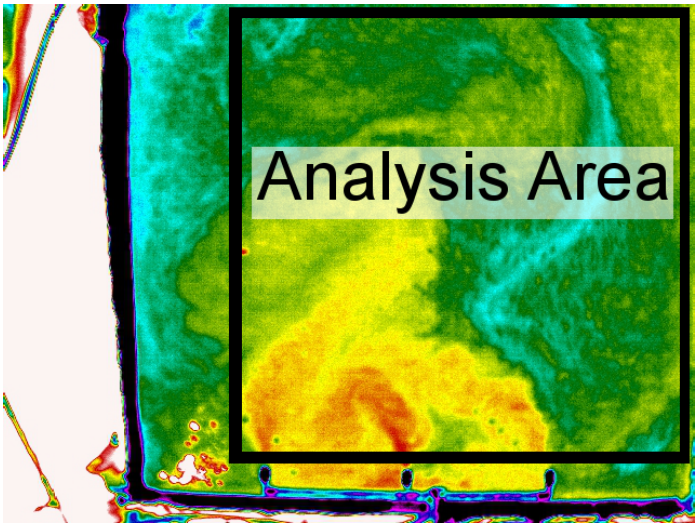

Fig. 4.18: Analysis area where pool temperatures were taken from.

4.3.2 Evaluating the Ground Sampling Methods

One application of TIR imagery is precision agriculture. It can be used to map evapotranspiration and soil moisture to help farmers irrigate and save water. To look at this application and to test these ground sampling methods, five separate flights were conducted over a two-month period to acquire VIS-NIR and TIR imagery over a farm. Each flight was 8-16 days apart in order to coincide with either Landsat 7 or 8. However the first flight had some cloud cover and a good Landsat image was not available. The first flight took place on May 16th 2013 and the last flight took place June 25th 2013.

Each flight took 20 minutes to cover the 1.5 km^2 area of interest and acquired 155 individual thermal images. These images were were stitched together and orthorectified into one image for each flight. Figure 4.19 shows the thermal mosaic acquired on June 9th.

Ground-Based Thermal Camera Results

Three to eight ground thermal images were collected during each flight. In order to match the thermal image from the aircraft, the ground thermal images were georeferenced using the targets placed at their corners. Figure 4.20 shows the georeferenced ground thermal image over bare soil (the pixilated image behind the ground thermal image is the aircraft image). The targets used to georeference the image are shown in the corner of the

ground thermal image. The aircraft pixels should only be compared with ground pixels if they are not mixed with the area outside of the sample area. The purple polygon shows which of these aircraft pixels are not mixed. The temperature of the ground pixels and the aircraft pixels within the purple polygon were averaged separately and used to model the relationship between the two. Figure 4.21 shows a plot of the data and the resulting model. More results from the ground camera sample regression for all of the flights can be found in Tables 4.6, 4.7, 4.8, 4.9, and 4.10.

Temperature Pool Results

During each flight, the pools were placed within the area of interest. Figure 4.22 shows the location of the cool temperature pool in the thermal mosaic. The measured

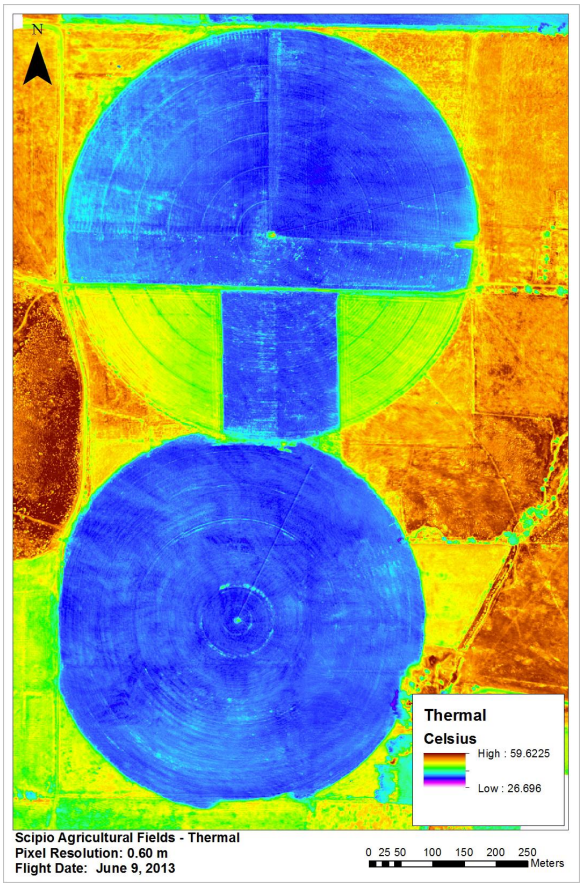

Fig. 4.19: The thermal mosaic acquired on June 9th 2013 from 450m AGL.

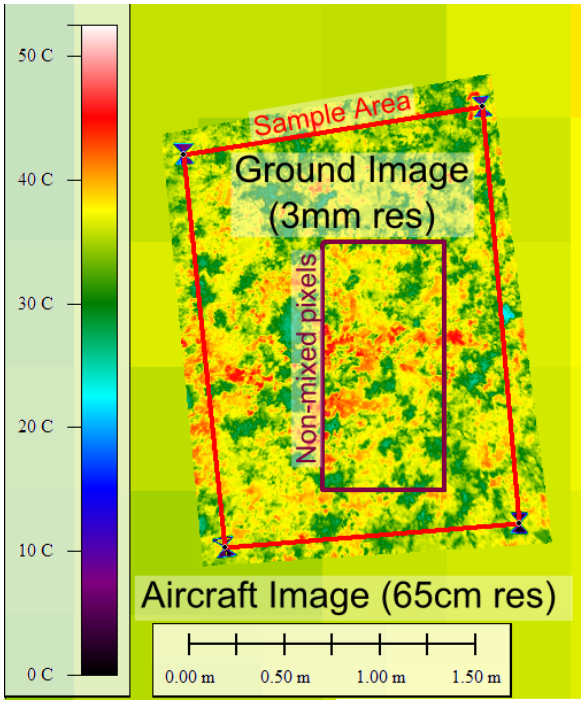

Fig. 4.20: A ground thermal image of bare-ground taken from ground-based thermal camera.

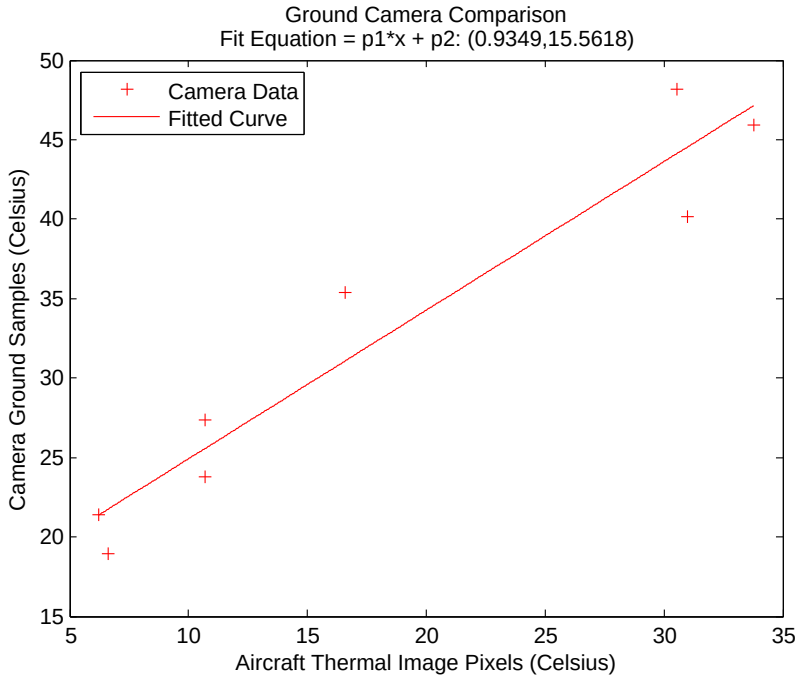

Fig. 4.21: Aircraft thermal pixels vs. ground thermal images (June 17th).

corner positions of the pools are used to determine the water surface of the pool (light blue polygon) and the non-mixed pixel area (yellow polygon). The non-mixed pixels from the aircraft thermal image are averaged and compared to the temperature values from the radiometer and the temperature probe. Figure 4.23 shows a plot of the data from the pool samples, the aircraft thermal pixels, and the resulting model for the flight on June 17th. Notice that the temperatures measured by the probes were warmer than the radiometer samples for both the hot and warm pools and almost equal for the cool pool. This illustrates the difference between the body temperature and surface temperature of water, and shows that the temperature probes might not be a good source of temperature data for this application (especially in windy conditions).

Ground Sampling Comparison

Figure 4.24 shows a Landsat thermal image and an AggieAir thermal image of the same area. A single element in the grid displayed over the AggieAir image shows the area covered by one Landsat pixel. The aircraft pixels under each of the elements in the grid are averaged to find a value to compare with each respective Landsat pixel. Figure 4.25 shows a plot of the data and the results of the regression between the aircraft thermal pixels and the Landsat thermal pixels for the fourth flight (June 17th). As Tables 4.6, 4.7, 4.8, 4.9, and 4.10 show, a linear relationship is seen for all of the flights.

Figure 4.26 is a plot that combines all of the data from one flight. While the models generated by the Landsat data and the ground camera samples are similar, the models generated by the temperature pools are very different. This is also shown in Table 4.11, which shows the coefficient of determination (R^2) and the residual norm for the models

Table 4.6: Regression results of surface sampling methods for flight #1 (May 16th).

Data Source	# of Samples	R^2	Residual Norm	RMSE
Ground Camera	3	0.996	0.197	0.768
Pool w/ Radiometer	3	0.996	0.415	1.116
Pool w/ Probes	3	0.999	0.00837	0.158

Table 4.7: Regression results of surface sampling methods for flight #2 (June 1st).

Data Source	# of Samples	R^2	Residual Norm	RMSE
Ground Camera	3	0.988	1.472	2.101
Pool w/ Radiometer	3	0.944	13.590	6.385
Pool w/ Probes	3	0.928	18.453	7.440
Landsat	1097	0.910	3.587	1.896

Table 4.8: Regression results of surface sampling methods for flight #3 (June 9th).

Data Source	# of Samples	R^2	Residual Norm	RMSE
Ground Camera	8	0.924	12.734	4.120
Pool w/ Radiometer	3	0.987	1.788	2.316
Pool w/ Probes	3	0.980	2.499	2.738
Landsat	1188	0.878	5.006	2.239

Table 4.9: Regression results of surface sampling methods for flight #4 (June 17th).

Data Source	# of Samples	R^2	Residual Norm	RMSE
Ground Camera	8	0.922	8.771	3.420
Pool w/ Radiometer	3	0.973	4.051	3.486
Pool w/ Probes	3	0.986	2.788	2.892
Landsat	1071	0.931	4.415	2.103

Table 4.10: Regression results of surface sampling methods for flight #5 (June 25th).

Data Source	# of Samples	R^2	Residual Norm	RMSE
Ground Camera	8	0.959	2.286	1.749
Pool w/ Radiometer	3	0.999	0.010	0.177
Pool w/ Probes	3	0.999	0.043	0.362
Landsat	1744	0.696	1.909	1.382

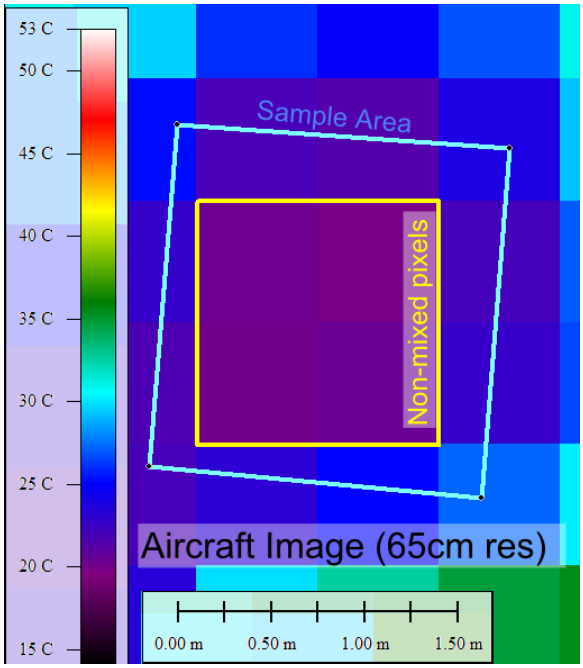

Fig. 4.22: Thermal aircraft image of cool temperature pool.

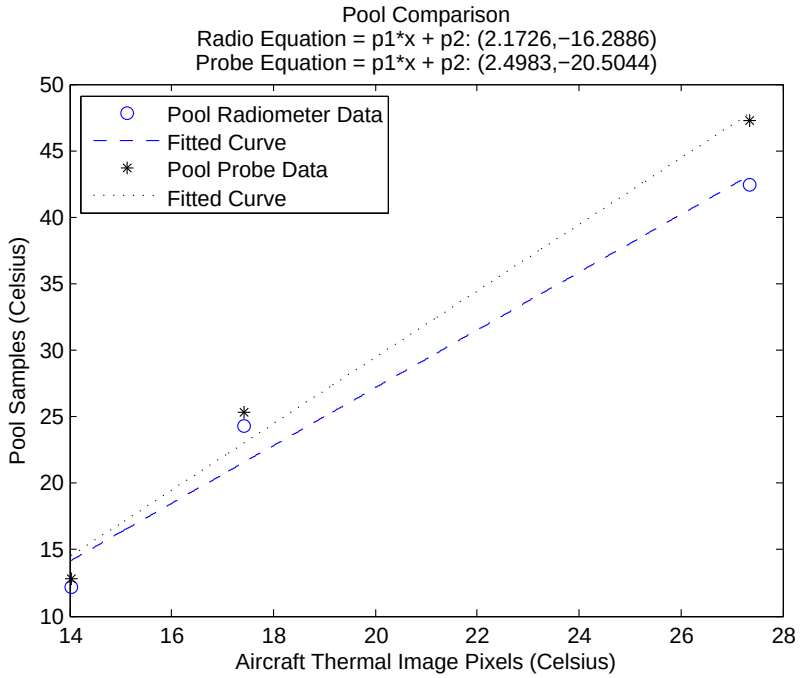

Fig. 4.23: Aircraft thermal pixels vs. pool temperature samples (June 17th).

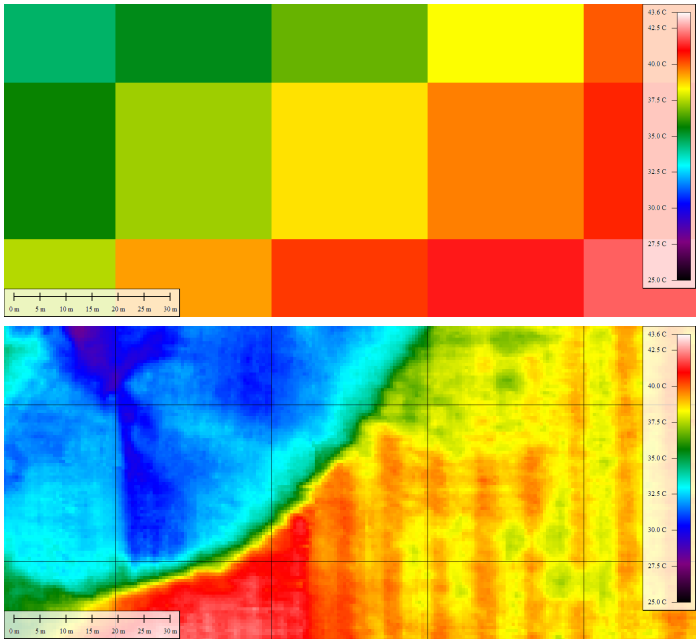

Fig. 4.24: Aircraft thermal pixels vs. Landsat thermal pixels (June 17th).

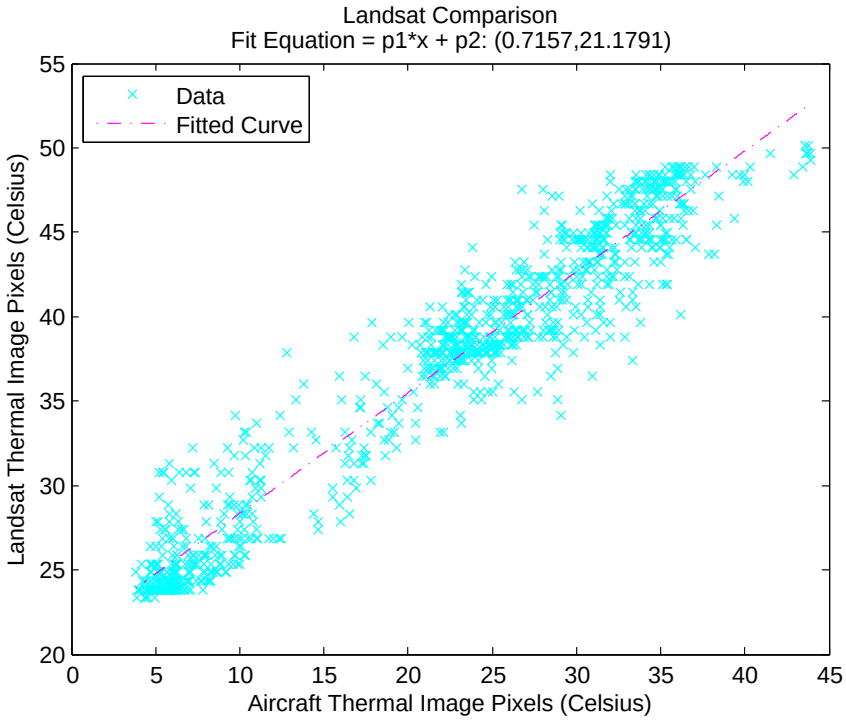

Fig. 4.25: Aircraft thermal pixels vs. Landsat thermal pixels (June 17th).

from the Ground Camera and the Pool methods using the data from Landsat instead of their respective dataset. This shows how well each model fits the Landsat data, which is used and trusted by many.

Table 4.11 shows that the Ground Camera models match the Landsat data much better than the Temperature Pool models. One reason for this could be that the Temperature Pool Method is more sensitive to mosaic position errors than the Ground Camera Method. This is true because the images from the Ground Camera Method were taken in uniform areas; if the position of the mosaic is off by a meter, it would not make much of a difference in the sample. This is not true for the Temperature Pool Method since the pools are only 1.7m×1.7m in dimension. If the mosaic is off by a meter, the sample would mix with the surrounding area and would distort the data. During processing, if it was obvious that the pools were not in the location originally measured with the GPS receiver they were moved. Even if there is no error in the position of the mosaic, it seems that the pools are not big enough and would still mix with the area outside the pools. Figure 4.26 shows this

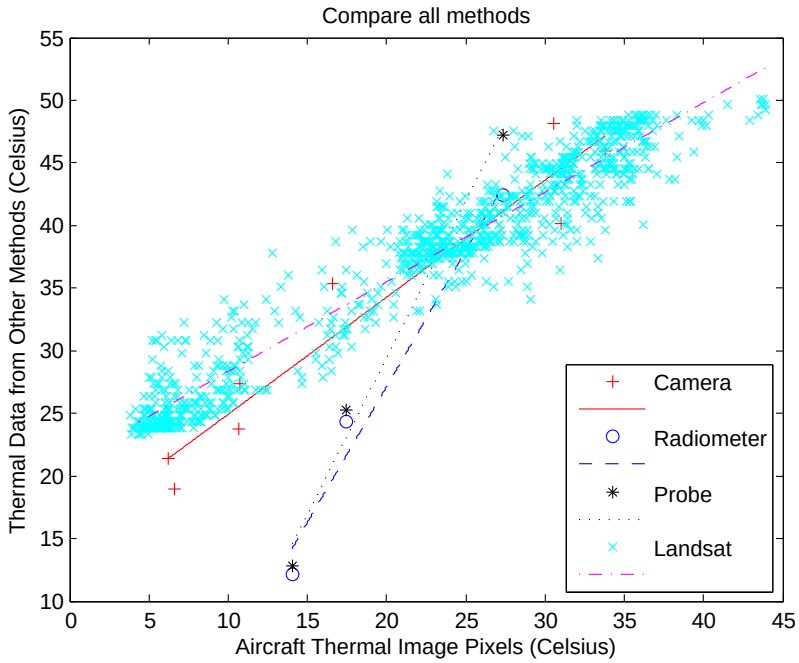

Fig. 4.26: Aircraft thermal pixels vs. sample methods (June 17th).

Table 4.11: Ground camera and pool models compared to Landsat data.

Data Source	R^2	Residual Norm
Ground Camera Flight #2	0.53227	18.6676
Ground Camera Flight #3	-0.24779	51.233
Ground Camera Flight #4	0.83285	10.6765
Ground Camera Flight #5	-2.9828	25.0755
Pool W/Radiometer Flight #2	-48.0416	1957.2956
Pool W/Radiometer Flight #3	-12.1971	541.8631
Pool W/Radiometer Flight #4	-3.4219	282.4404
Pool W/Radiometer Flight #5	-8.0791	57.1618
Pool W/Probe Flight #2	-47.6071	1939.9559
Pool W/Probe Flight #3	-11.3107	505.4652
Pool W/Probe Flight #4	-4.9598	380.6732
Pool W/Probe Flight #5	-11.3266	77.6081

possibility. While the point for the hot pool lies in the cluster of Landsat data, the points for the warm and cold pools are both measured warmer than they should by the aircraft thermal image. This could be because the pixels over the pools are being mixed with the outer warmer pixels. This mixing can be observed in the data from all of the flights.

Even though the Ground Camera models match the Landsat data better than the Temperature Pool models, it is not consistent. The Ground Camera data in Table 4.11 shows a better fit to Landsat data for flights two and four than for three and five. This could be because flights two and four were captured during Landsat 7 while flights three and five were captured during Landsat 8. Table 4.12 also shows the correlation between the goodness-of-fit values and possible sources of error between the Ground Camera method and Landsat. Notice the high correlation between both the R^2 and Residual Norm values and the Landsat mission number. Other sources of error with a high correlation include wind speed and relative humidity. One other reason for the inconsistencies could be the different thermal bands of Landsat 7 (band 6: 10.4 - 12.5μm [52]), Landsat 8 (band 10: 10.9 - 11.2 μm [53]), and the ICI 7640 (7.5 - 14μm).

Table 4.13 shows how the Ground Camera Models correlate with meteorological data. If there is some correlation between this data, a model based on weather could be used

Table 4.12: Correlation between possible error sources and ground camera model Landsat goodness of fit.

	Wind Speed	Air Temp	Relative Humidity	Solar Rad	Time Diff	Landsat 7 or 8
R^2	-0.79	-0.28	-0.44	-0.25	-0.18	-0.76
Res Norm	-0.32	0.18	0.89	-0.44	-0.41	0.77

to calibrate the aircraft mosaic instead of ground sampling. One or both coefficients from the Ground Camera Models show good correlation with air temperature, relative humidity, and solar radiation. With enough data, it is likely that a model could be created to replace ground sampling.

4.3.3 Ground Sampling Conclusions

Two methods were tested to sample surface temperatures on the ground to calibrate thermal aerial imagery taken from a small unmanned aircraft. The first method uses a ground-based thermal camera to take a high-resolution sample of surface temperature. The second method is to create temperature controlled pools which can be seen by the airborne thermal camera. They were both compared to Landsat and it was shown that the models generated using the ground thermal camera matched the Landsat data better than the temperature pools. It is likely that the pools did not match the Landsat data because they were not big enough and the aircraft pixels over the pools were mixing with the surrounding area. While this could be fixed by increasing the size of the pools, their current size is already hard to manage. The Ground Camera Method matched Landsat better because the samples could be collected from semi-uniform areas (e.g. bare soil, irrigated fields, non-irrigated fields, etc.) which are less prone to position errors in the mosaic. In addition, the Ground Camera Method can be used to collect many samples while the Temperature Pool

Table 4.13: Correlation between weather parameters and ground camera model coefficients.

	Wind Speed	Air Temperature	Relative Humidity	Solar Radiation
Slope	0.53	0.49	0.53	-0.61
Intercept	-0.35	-0.83	-0.39	0.035

Method is restricted to three.

Even though the Ground Camera Method performs better than the pool method, it was inconsistent with matching the Landsat data. Results showed that this is likely to be caused by the different Landsat satellites used to collect the data (Landsat 7 and Landsat 8). Overall, the Ground Camera Method seems like a good method to calibrate the thermal mosaics from AggieAir. More data should be obtained to confirm this.

Future work includes gathering more data to further investigate the relationship between the Ground Camera Method and Landsat. Since strong correlations were shown between the ground camera models and meteorological data, more data is also needed to establish a model to calibrate the thermal mosaic based on weather to replace the ground sampling.

4.4 Chapter Summary

Even though they share many of the same procedures, processing TIR imagery can be a lot more complex than VIS-NIR imagery. For example preparing the images for orthorectification is required in order to compensate for potential problems (like drift) and to map the temperature values into DNs so the orthorectification software can stitch them together. Geometric calibration is also more challenging with a thermal camera since it cannot distinguish differences in color and the standard target cannot be used. The largest challenge with using TIR imagery for aerial imagery is compensating for external disturbances (e.g. atmosphere and moving air cooling the lens) which affect the output of the camera. In order to compensate for these effects, new ground sampling techniques were presented in this chapter and compared against a trusted source or remotely sensed data (Landsat). Future work in this area includes gathering more ground sampling data to generate models to compensate for external disturbances.

Chapter 5

Biotelemetry Fish Tracking

In order to preserve our native fish species in the watersheds of the United States, managing, monitoring, and studying fish habitat is very important. Extensive fish habitat studies are conducted to minimize environmental impact before building a dam, while restoring natural habitat in a river, or in ensuring the economic strength of a fisheries market. An important part of these studies is tracking where fish are migrating, moving and living. This is commonly accomplished by tagging the fish of interest with a radio transmitter to locate the fish in the future to see where it has moved [20, 54]. The transmitter does not include position information, so localization is performed using a receiver and a directional antenna. As the antenna is pointed in the direction of the fish, the signal sent from the transmitter becomes louder. The operator can hear the beacon through the receiver and navigates toward the fish. While this method has proved to be effective, it can be time consuming and costly.

An alternative method for tracking fish utilizes AggieAir and a recently developed fish tracking payload [55]. Using the fish tracking payload, AggieAir is able to fly over a body of water and receive the signal transmitted by tagged fish. As AggieAir flies over the area of interest, the fish tracker measures the signal strength from its receiver and logs other data, including position, orientation, and speed of the aircraft. With this information, the aircraft is directed toward areas of the map to improve the estimate of the tag location. Others have looked into similar scenarios. In a general radio tracking problem, Frew et al. [56] proposed a radio localization technique cast as a distributed estimation problem. Consensus within a group of UAs was reached with a decentralized method; however, the algorithms used are computationally complex and only considered communication with one neighboring aircraft. Korner et al. [57] introduced a method that uses particle filters to

track multiple targets with radio tags. Implementation employed only one UA. While these methods work, a simple, decentralized method is needed for multi-UA navigation and radio tag localization. A method employing these features could be more practical for use in small UAS with embedded systems.

The fish-tracking methods introduced in this chapter are focused on simplicity for navigation, multi-UA coordination, and radio transmitter location estimation. Simplicity is important for real-world, real-time fish-tracking applications. Therefore, swarm-like rules (using potential fields [58]) are established for navigation and multi-UA coordination/avoidance. While navigating according to these rules, an Extended Kalman Filter is used to estimate the position of the transmitter. Four simple navigation methods are introduced which use this estimate and its covariance to direct the aircraft toward areas to improve the estimate of the tag position. Figure 5.1 shows the steps to estimate the position of the tag and how it relates to The Processing Cycle for Meaningful Remote Sensing. Notice the similarities between Figure 5.1 and Figure 1.1; they are identical except that the blocks and signals are labeled more specifically for fish tracking in Figure 5.1. An interesting difference between this fish tracking application and the VIS-NIR and TIR applications is that the fish tracking payload closes the loop in real-time and the actionable information is used by the UA to gather better data.

A real-world simulation is created and used with Monte Carlo analysis to test and evaluate these methods using one to three UAs. Part of this simulation includes a complex propagation model for the tag which is based on real flight data. The results from the Monte Carlo analysis give clear answers to which methods are effective, and what the expected performance would be in real-world scenarios.

5.1 Simulation Environment

In order to properly test different methods to locate tagged fish, a real-world simulation is needed. Figure 5.2 shows a diagram that describes the different pieces of the simulation. Multiple UAs can be included in the simulation. Each UA (i) uses wind ($|W|, \angle W$) and noise (ω, η) to generate truth states (X_i), and estimation states ($\hat{X}_i$). The potential field

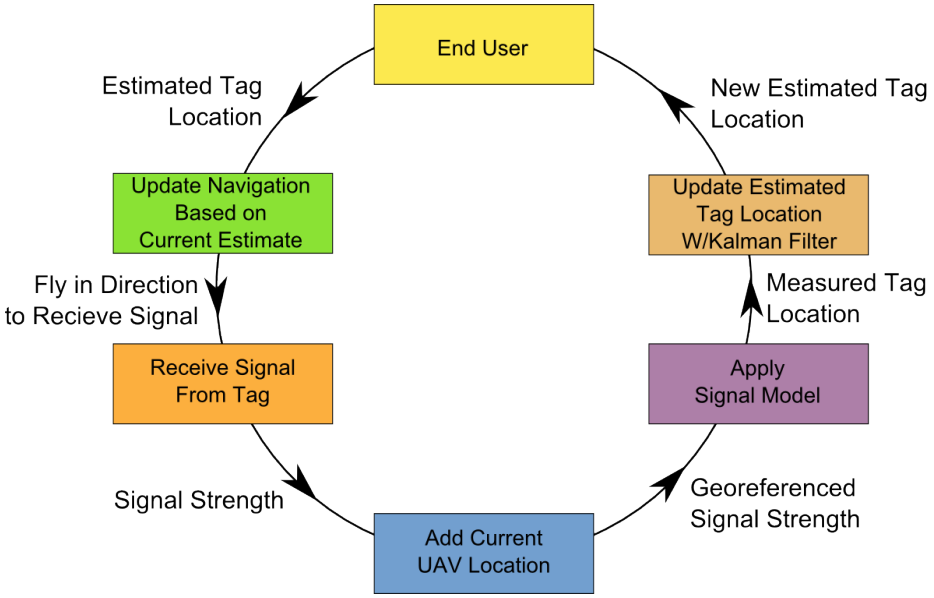

Fig. 5.1: The processing cycle for fish tracking.

map receives the estimation states from each of the UAs and updates the map with their current position. If the UA receives a signal from the fish tag, the UA estimation states are also used to update the estimated tag position. The truth state of the UA is used by the tag propagation model to determine whether or not a UA is close enough to receive a measurement and what that measurement will be ($\tilde{S}_i$). When the estimated tag state ($\hat{X}_T$) is updated with a new measurement, the estimated tag state and the corresponding covariance matrix (P_T) are both used to update the potential field map. The potential field map provides a force (F) which the UAs will use to control their heading. Indirectly through the potential map, the UAs share each others position, and the estimated position and covariance matrix of the tag. Static objects can also be contained in the potential map like ground-based obstacles and a boundary. The tag state estimation error (δX_T) is used to determine the success of the tag estimation and is calculated by subtracting the tag state estimate with the tag truth state (X_T).

Monte Carlo analysis was used with δX_T to determine whether or not a method was successful. The basic idea of Monte Carlo analysis is to run a high-fidelity simulation many times. Because of the noise and disturbances included in the simulation each trajectory

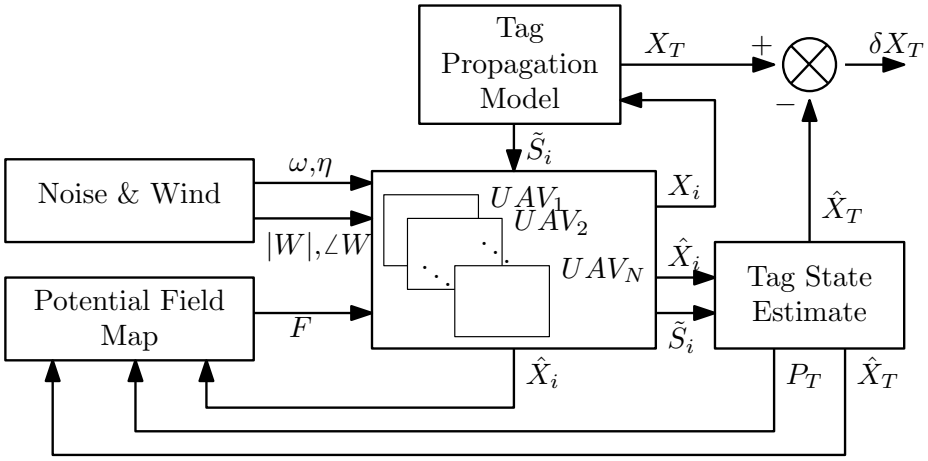

Fig. 5.2: Flight simulation system diagram.

generated by the simulation will be different. Monte Carlo analysis is used to show how the trajectories vary and predict expected performance in real-world scenarios. For example, the simulation in Figure 5.2 was run 100 times to look at how much δX_T varies for the different methods. One single run by this simulation will be referred to as a flight. Equation (5.1) shows how an error trajectory $\delta X_k(t)$ is calculated for flight number k.

$$\delta X_k(t) = X_T(t) - \hat{X}_{Tk}(t) \tag{5.1}$$

After all of the flights are finished, the error trajectories are compiled together in $\Omega(t)$:

$$\Omega(t) = [\delta X_1(t), \delta X_2(t) \cdots \delta X_N(t)]^T. \tag{5.2}$$

Then the mean $\mu(t)$ and variance $\Sigma(t)^2$ of $\Omega(t)$ are found for each time (t).

$$\mu(t) = E[\Omega(t)], \tag{5.3}$$

$$\Sigma(t)^2 = E[(\mu(t) - \Omega(t))(\mu(t) - \Omega(t))^T]. \tag{5.4}$$

The mean of the error trajectories describes the accuracy that most of the flights should achieve for that given method. The variance describes the best and the worst that

can be expected around the mean. Many applications require thousands of runs to reduce the uncertainty of the estimated variance. For this application, 100 flights are enough to compare navigation methods. In addition, the uncertainty of the variance is documented and confidence intervals around the variance curves are calculated using the chi-squared distribution.

The subsections below describe the important pieces of the flight simulation. These include the environmental dynamics, the UA system dynamics, simulating and estimating the tag Location, and navigation using potential fields.

5.1.1 Environmental Dynamics

Equation (5.5) is used to calculate the magnitude and direction of wind. $|W|_0$ and $\angle W_0$ are nominal values of the wind and $b_{|W|}$ and $b_{\angle W}$ are random biases modeled as first order Markov stochastic processes (Equation (5.6)).

$$\begin{aligned} |W| &= |W|_0 + b_{|W|}, \\ \angle W &= \angle W_0 + b_{\angle W}. \end{aligned} \tag{5.5}$$

$$\begin{aligned} |\dot{W}|_0 &= 0, \\ \angle \dot{W}_0 &= 0, \\ \dot{b}_{|W|} &= -\frac{b_{|W|}}{\tau_{|W|}} + \omega_{|W|}, \\ \dot{b}_{\angle W} &= -\frac{b_{\angle W}}{\tau_{\angle W}} + \omega_{\angle W}. \end{aligned} \tag{5.6}$$

The driving noise ($\omega_{|W|}$, $\omega_{\angle W}$) is Gaussian with the following properties:

$$\begin{aligned} E[\omega_{|W|}] &= 0, & E[\omega_{|W|}\omega'_{|W|}] &= \frac{2\sigma^2_{|W|}}{\tau_{|W|}}\delta(t-t'). \\ E[\omega_{\angle W}] &= 0, & E[\omega_{\angle W}\omega'_{\angle W}] &= \frac{2\sigma^2_{\angle W}}{\tau_{\angle W}}\delta(t-t'). \end{aligned} \tag{5.7}$$

5.1.2 UA System Dynamics

Figure 5.3 shows a detailed diagram of the simulated UA system for UAV_i. The force from the potential field map (F) is used by the controller to generate u_i (desired rate of change for the heading). This control input along with the noise and wind are used to generate the UA truth states (X_i) and the GPS measurements ($\tilde{z}_i$). The GPS measurements are used as measurements in the Kalman Filter to generate the estimated states of the UA.

Truth Dynamics

Equation (5.8) shows the UA truth state dynamics. x_i and y_i describe the position of the UA and its time derivative is a function of the airspeed v_i, the yaw ψ_i, and the x and y components of the wind (W_x, W_y). The airspeed is assumed to be constant and the change in yaw is equal to the controller output (u_i).

$$\begin{aligned}
\dot{x}_i &= v_i \cos(\psi_i) + W_x, \\
\dot{y}_i &= v_i \sin(\psi_i) + W_y, \\
\dot{v}_i &= 0, \\
\dot{\psi}_i &= u_i, \\
\dot{b}_{xi} &= -\frac{b_{xi}}{\tau_x} + \omega_{xi}, \\
\dot{b}_{yi} &= -\frac{b_{yi}}{\tau_y} + \omega_{yi}.
\end{aligned} \tag{5.8}$$

b_{xi} and b_{yi} are biases in the GPS measurement. These biases are also modeled as first order Markov stochastic processes.

$$\begin{aligned}
E[\omega_{xi}] &= 0, & E[\omega_{xi}\omega'_{xi}] &= \frac{2\sigma_x^2}{\tau_x}\delta(t-t'). \\
E[\omega_{yi}] &= 0, & E[\omega_{yi}\omega'_{yi}] &= \frac{2\sigma_y^2}{\tau_y}\delta(t-t').
\end{aligned} \tag{5.9}$$

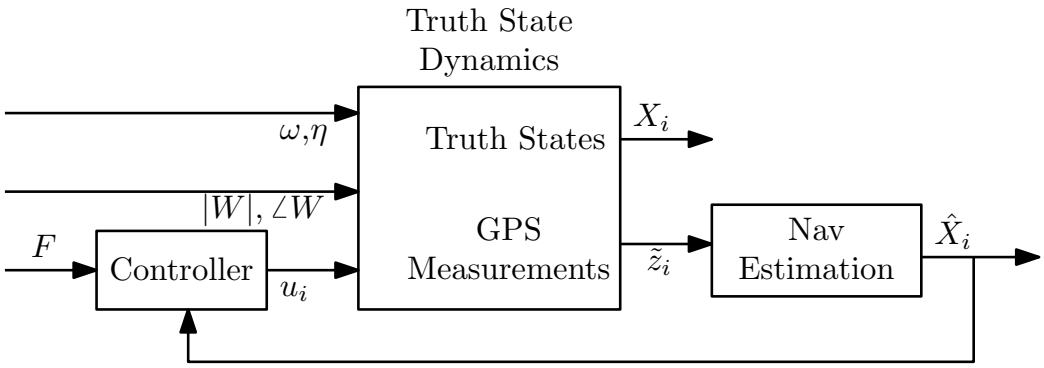

Fig. 5.3: UA system diagram.

Equation (5.10) shows the equations to calculate other important truth variables: ground speed (v_{gi}), and heading (ϕ_i).

$$\begin{aligned} v_{gi} &= \sqrt{\dot{x}_i^2 + \dot{y}_i^2}, \\ \phi_i &= \tan^{-1} \frac{\dot{y}_i}{\dot{x}_i}. \end{aligned} \tag{5.10}$$

Part of the truth model includes generating the GPS measurements that will be used by the navigation. As shown by Equation (5.11), the kth measurement is a function of the current position (x_i or y_i) and the respective random bias.

$$\begin{aligned} \tilde{x}_i[k] &= x_i + b_{xi}, \\ \tilde{y}_i[k] &= y_i + b_{yi}. \end{aligned} \tag{5.11}$$

A measured ground speed ($\tilde{v}_{gi}[k]$) and heading ($\tilde{\phi}_i[k]$) is also generated from the GPS measurements.

$$\begin{aligned} \tilde{v}_{gi}[k] &= \frac{\sqrt{(\tilde{x}_i[k] - \tilde{x}_i[k-1])^2 + (\tilde{y}_i[k] - \tilde{y}_i[k-1])^2}}{t[k] - t[k-1]}, \\ \tilde{\phi}_i[k] &= \tan^{-1} \frac{\tilde{y}_i[k] - \tilde{y}_i[k-1]}{\tilde{x}_i[k] - \tilde{x}_i[k-1]}. \end{aligned} \tag{5.12}$$

UA Navigation Estimation

To control the heading of the UA according to the potential field map, an estimated position and heading of the UA is needed ($\hat{\mathbf{X}}$): this is achieved through a Kalman Filter.

$$\hat{\mathbf{X}} = [\hat{x}_i \ \hat{y}_i \ \hat{\phi}_i]^T \tag{5.13}$$

To develop the Kalman filter, a design model is used where

$$\mathbf{X}^{dm} = [x_i^{dm} \ y_i^{dm} \ \phi_i^{dm}]^T, \tag{5.14}$$

and

$$\begin{aligned} \dot{x}_i^{dm} &= \tilde{v}_{gi}^{dm} \cos(\phi_i^{dm}) + \omega_x^{dm}, \\ \dot{y}_i^{dm} &= \tilde{v}_{gi}^{dm} \sin(\phi_i^{dm}) + \omega_y^{dm}, \\ \dot{\phi}_i^{dm} &= u_i + \omega_\phi^{dm}. \end{aligned} \tag{5.15}$$

ω_x^{dm}, ω_y^{dm}, and ω_ϕ^{dm} represent the process noise of the propagation.

Equation (5.15) can also be represented in the following vector form.

$$\dot{\mathbf{X}}^{dm} = \hat{f}(\mathbf{X}^{dm}, \tilde{v}_{gi}^{dm}, u_i) + \hat{B}\mathbf{w}^{dm}, \tag{5.16}$$

where

$$\begin{aligned} \hat{f} &= \begin{bmatrix} \tilde{v}_{gi}^{dm} \cos(\phi_i^{dm}) \\ \tilde{v}_{gi}^{dm} \sin(\phi_i^{dm}) \\ u_i \end{bmatrix}, \\ \hat{B} &= \begin{bmatrix} 1 & 0 & 0 \\ 0 & 1 & 0 \\ 0 & 0 & 1 \end{bmatrix}, \\ \mathbf{w}^{dm} &= [\omega_x^{dm} \omega_y^{dm} \omega_\phi^{dm}]^T. \end{aligned} \tag{5.17}$$

Using this design, the filter state is propagated according to the following equations:

$$\dot{\hat{\mathbf{X}}} = \hat{f}(\hat{\mathbf{X}}, \tilde{v}_{gi}, u_i), \tag{5.18}$$

$$\dot{\hat{P}} = \hat{F}\hat{P} + \hat{P}\hat{F}^T + \hat{B}\hat{Q}\hat{B}^T, \tag{5.19}$$

where

$$\hat{F} = \frac{\partial \hat{f}}{\partial \hat{\mathbf{X}}} = \begin{bmatrix} 0 & 0 & -\sin(\hat{\phi}_i) \\ 0 & 0 & \cos(\hat{\phi}_i) \\ 0 & 0 & 0 \end{bmatrix}, \tag{5.20}$$

$$\hat{Q} = E[\mathbf{w}^{dm}(\mathbf{w}^{dm})^T] = \begin{bmatrix} \sigma_{px}^2 & 0 & 0 \\ 0 & \sigma_{py}^2 & 0 \\ 0 & 0 & \sigma_{p\psi}^2 \end{bmatrix}. \tag{5.21}$$

For the update step of the Kalman filter, Equation (5.22) shows how the GPS measurements are related to the states of the design model.

$$\begin{aligned} \tilde{x}_i^{dm}[k] &= x_i^{dm} + \eta_{bx}^{dm}, \\ \tilde{y}_i^{dm}[k] &= y_i^{dm} + \eta_{by}^{dm}, \\ \tilde{\phi}_i^{dm}[k] &= \phi_i^{dm} + \eta_{\phi}^{dm}. \end{aligned} \tag{5.22}$$

The vector form of Equation (5.22) is shown below.

$$\tilde{z}_i[k] = \hat{h}(\mathbf{X}^{dm}) + \nu^{dm}, \tag{5.23}$$

where

$$\hat{h}(\mathbf{X}^{dm}) = \begin{bmatrix} x_i^{dm} \\ y_i^{dm} \\ \phi_i^{dm} \end{bmatrix}, \quad \nu^{dm} = \begin{bmatrix} \eta_{bx}^{dm} \\ \eta_{by}^{dm} \\ \eta_{\phi}^{dm} \end{bmatrix}. \tag{5.24}$$

Based on this design, the update equations for the Kalman filter are shown below.

$$\begin{aligned} K &= P^{-}\hat{H}^{T}(\hat{H}P^{-}\hat{H}^{T} + \hat{R})^{-1}, \\ P^{+} &= (I - K\hat{H})P^{-}(I - K\hat{H})^{T} + K\hat{R}K^{T}, \\ \hat{\mathbf{X}}^{+} &= \hat{\mathbf{X}}^{-} + K(\tilde{z} - \hat{z}), \end{aligned} \tag{5.25}$$

where

$$\hat{z}_i[k] = \hat{h}(\hat{\mathbf{X}}^{-}), \tag{5.26}$$

$$\hat{H} = \frac{\partial \hat{h}}{\partial \hat{\mathbf{X}}} = \begin{bmatrix} 1 & 0 & 0 \\ 0 & 1 & 0 \\ 0 & 0 & 1 \end{bmatrix}, \tag{5.27}$$

$$\hat{R} = E[\nu^{dm}(\nu^{dm})^{T}] = \begin{bmatrix} \sigma_x^2 & 0 & 0 \\ 0 & \sigma_y^2 & 0 \\ 0 & 0 & \sigma_\phi^2 \end{bmatrix}. \tag{5.28}$$

Heading Control

All of the UAs share their location to the potential field map. When UA_i shares its location (x_i and y_i), the potential field map finds the gradient of the potential in that area (created from other UAs, the border, other obstacles, etc.) and returns a force $F_i(x_i, y_i)$. The x and y components of the force are used to find the desired heading ϕ_{di} of the UA (Equation (5.29)).

$$\begin{aligned} F_i(x_i, y_i) &= F_x\,\hat{\mathbf{i}} + F_y\,\hat{\mathbf{j}}, \\ \phi_{fi} &= \tan\left(\frac{F_y}{F_x}\right). \end{aligned} \tag{5.29}$$

Figure 5.4 shows a diagram of the closed-loop heading controller. The error ($\phi_e = \phi_{fi} - \hat{\phi}_i$) is multiplied by a control gain k_i in order to give the appropriate amount of

control to turn the UA in the right direction. This control output (u_i) is the turning rate of the UA and is limited to physical constraints ($|u_i| \leq u_{max}$) which are applied to the control output before it is given to the UA.

5.1.3 Simulating and Estimating the Tag Location

To simulate the signal ($\tilde{S}$) that is received by the UAs, actual flight data was collected with AggieAir to find the propagation model. This data was collected by flying the fish tracking payload in the flower pattern shown in Figure 5.5 at 400m above the tag. Before the flight, the position of the tag (x_t, y_t) and the polarization angle (α_t) were both observed. During the flight, the payload software logged the signal strength and the position and orientation of the UA.

This data was fit to Equation (5.30) where f_s is the signal model, r is the distance from the UA to the tag (x_t, y_t), α is the difference between the polarization angles of the tag and the UA, and η_s is Gaussian white noise. The strength of measured signals ($\tilde{S}_m$) are used to find the coefficients of f_s (Equation (5.32)). As Equation (5.34) shows, α is symmetric around its own axis and the axis perpendicular to it ($0 \leq \alpha \leq \pi/2$).

$$\tilde{S} = f_s(r, \alpha) + \eta_s \tag{5.30}$$

$$E[\eta_s] = 0, \qquad E[\eta_{si}\eta_{sj}^T] = \sigma_s^2 \delta(ij) \tag{5.31}$$

$$f_s(r, \alpha) = \beta_1 + \beta_2 r + \beta_3 r^2 + \beta_4 r^3 + \beta_5 + \beta_6 \alpha + \beta_7 \alpha^2 + \beta_8 \alpha^3 \tag{5.32}$$

$$r = \sqrt{(\hat{x}_t - \hat{x})^2 + (\hat{y}_t - \hat{y})^2}, \tag{5.33}$$

$$\alpha = \begin{cases} \alpha_u - \alpha_t + 180 & -180 \leq \alpha_t - \alpha_u < -90 \\ \alpha_t - \alpha_u & -90 \leq \alpha_t - \alpha_u < 0 \\ \alpha_u - \alpha_t & 0 \leq \alpha_t - \alpha_u < 90 \\ \alpha_t - \alpha_u + 180 & 90 \leq \alpha_t - \alpha_u \leq 180 \end{cases} . \tag{5.34}$$

Figure 5.6 shows the result of the modeling. The surface in the plot is the model,

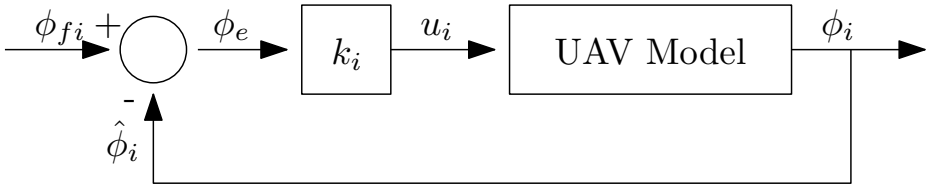

Fig. 5.4: Closed-loop heading controller.

and the points around the surface are the measured signals received during the flight. The values of the signal are unitless and represent the 8-bit integer values given to the payload computer during flight. It is likely that they could be converted to signal strength in decibels and that they are logarithmic; however they were not converted for this study. Figure 5.7 shows the residuals between the model and the data. The data from this figure shows the noise of the signal and is used to generate η_s in Equation (5.30) for the simulation. Notice that the 3-sigma value for the noise is half of the maximum possible value for the signal

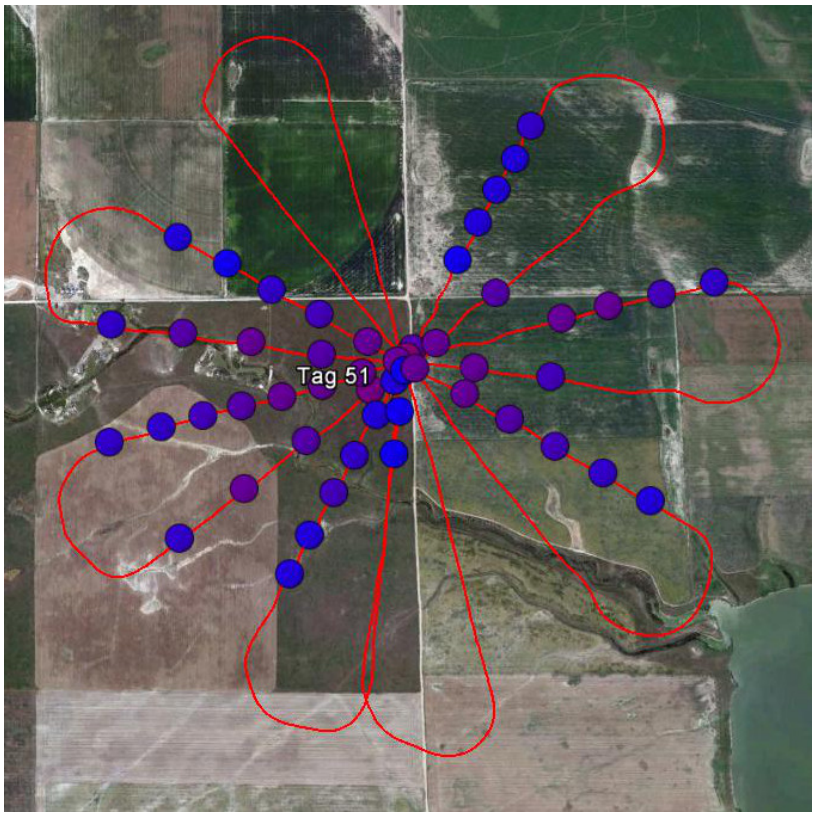

Fig. 5.5: The flower flight path used to collect flight data.

strength (approx. 80). This is to be expected in a wireless system especially while using a relatively simple model. A more complex model may yield lower noise but is not needed for the simulation since the goal is to recreate the signal (even if it is very noisy).

An Extended Kalman Filter was used to estimate the position of the tag. $\mathbf{X}_t$ is the state vector for the filter.

$$\mathbf{X}_t = \begin{bmatrix} x_t \\ y_t \end{bmatrix} \tag{5.35}$$

It is assumed that the tag will not move ($\dot{\mathbf{X}}_t = 0$), therefore there is no need for a propagation step with this filter. However, a linearized measurement model is needed. Equation (5.36) shows the measurement model that was used in the Kalman Filter. $\hat{h}$ is a simplified version of f_s and is not a function of α. In addition only the first two terms in r are going to be used for estimation.

$$\hat{S} = \hat{h}(r), \tag{5.36}$$

$$\hat{h}(r) = \beta_1 + \beta_2 r. \tag{5.37}$$

The Kalman gain K can be computed and the state and covariance matrices can be updated using Equation (5.38).

$$\begin{aligned} K &= P^- H^T (H P^- H^T + R)^{-1}, \\ P^+ &= (I - KH) P^- (I - KH)^T + KRK^T, \\ \hat{\mathbf{X}}_t^+ &= \hat{\mathbf{X}}_t^- + K(\tilde{S} - \hat{S}), \end{aligned} \tag{5.38}$$

where

$$H = \frac{\partial h}{\partial \mathbf{X}_t}, \tag{5.39}$$

$$\mathbf{H} = \frac{\partial \hat{h}}{\partial \mathbf{X}_t} = \left[\frac{\beta_2(\hat{x}_t - \hat{x})}{r}, \frac{\beta_2(\hat{y}_t - \hat{y})}{r} \right], \tag{5.40}$$

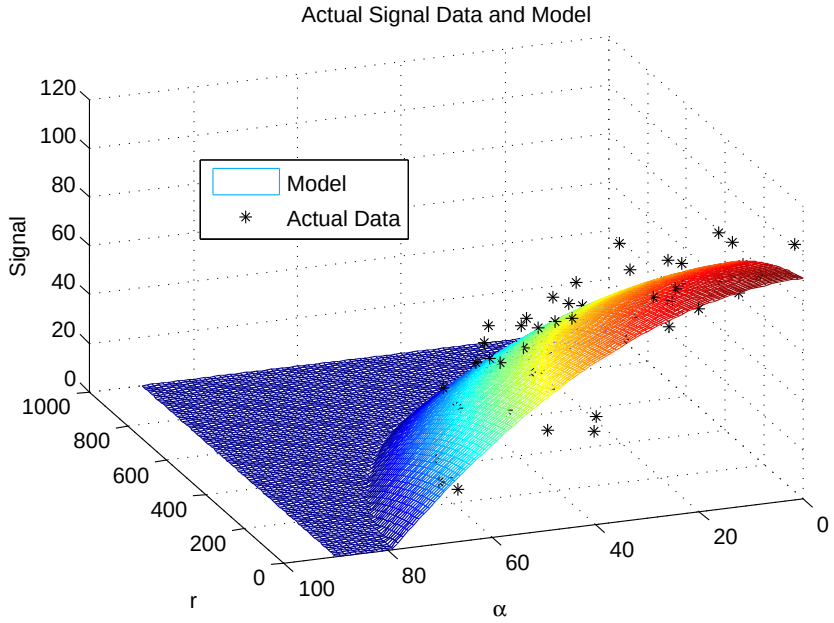

Fig. 5.6: The two-dimensional, fourth-order polynomial model plotted with the test flight data.

$$R = E[\eta_s(\eta_s)^T] = \sigma_s^2. \tag{5.41}$$

5.1.4 Navigation using Potential Fields

Conventional Potential Fields

Potential fields (PFs) are commonly used to dynamically plan the motion of ground [58] and air-based [59] mobile robots (agents). They are used to attract or repel agents to or from objects and other agents. For example, repulsive PFs around all agents could ensure that they do not collide with one another. Equation (5.42) shows a conventional definition of an attractive PF [60].

$$U(x) = \frac{1}{2}k(x_a - x_g)^2 \tag{5.42}$$

This PF is applied to the agents through a force defined as the negative gradient of the PF:

$$F(x) = -\nabla U(x). \tag{5.43}$$

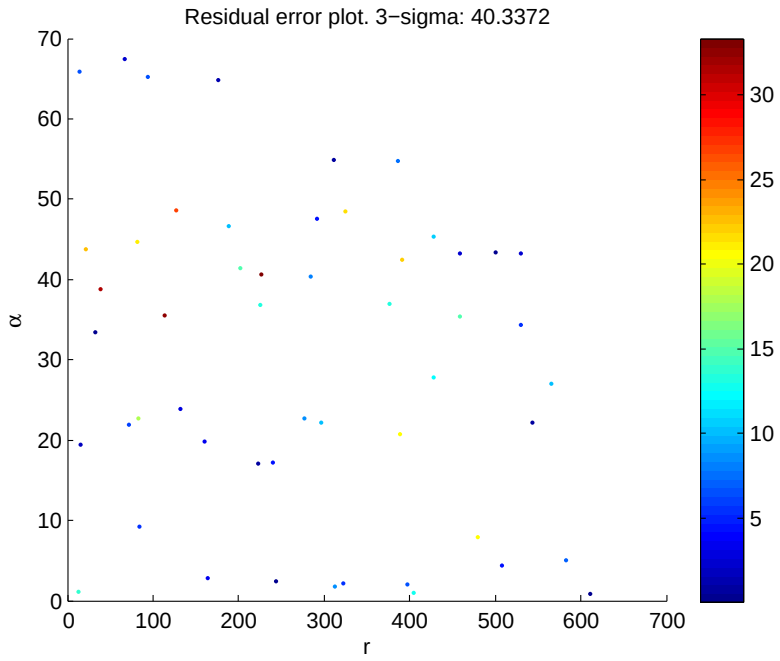

Fig. 5.7: Residuals of the flight data vs. the signal model.

As x_a (position of agent) gets further away from x_g (position of a goal), $U(x)$ goes up. The slope of $U(x)$ also increases as $U(x)$ goes up, which increases the force acting on the agent from the PF and attracts the agent toward x_g. A repulsive PF would increase as the distance from the object to the agent decreases and would repel the agent.

Fractional Order Potential Fields

The method used to generate the PFs for this project is called the Fractional Order Potential Field (FOPF) [61]. The main advantage of the FOPF over other methods is that the FOPF allows the user to design repulsive PFs based on a level of danger. For example, a collision with another UA would be very dangerous and therefore would get a different PF that produced a higher force than the PF of a less dangerous object like a boundary.

A repulsive FOPF is derived starting with the definition of the Coulombian electric field $E(r)$

$$E(r) = \frac{q}{4\pi\epsilon_0 r^2}. \tag{5.44}$$

A single integration of $E(r)$ produces the Coulombian potential from the electric field of a punctual charge ($V_1(r)$), and a double integration produces the Coulombian PF generated by the uniformly distributed charge along a straight-line segment $V_2(r)$:

$$V_1(r) = \frac{q}{4\pi\epsilon_0 r}, \tag{5.45}$$

$$V_2(r) = \frac{q \ln r}{4\pi\epsilon_0}. \tag{5.46}$$

Both $V_1(r)$ and $V_2(r)$ could be used as repulsive PFs. Figure 5.8 (for $n = 1$ and $n = 2$) shows the normalized potential of $V_1(r)$ and $V_2(r)$ vs. distance and shows that $V_2(r)$ will have a stronger force at a larger distance than $V_1(r)$. For a more dangerous object, $V_2(r)$ would be preferred over $V_1(r)$. It turns out that with each successive integration of $E(r)$, more force is applied at a further distance. Fractional calculus can be used to generate these integrals, as well as fractional order integrals. This conversion using the Weyl fractional integral [62] is given below:

$$V_n(r) = W^r E(r) = \frac{q}{4\pi\epsilon_0 \Gamma(n)} \int_r^\infty \frac{(\theta - r)^{n-1}}{r^2} d\theta, \tag{5.47}$$

where $V_n(r)$ is the nth integral of $E(r)$ (n can be any number greater than 0) and $\Gamma(n)$ is the Gamma function.

$$\Gamma(n) = \int_0^1 \left[\ln\left(\frac{1}{t}\right)\right]^{n-1} dt \tag{5.48}$$

After manipulating Equation (5.47), $V_n(r)$ can be written as shown below:

$$V_n(r) = \frac{q}{4\pi\epsilon_0} \frac{\Gamma(2-n)}{r^{2-n}} \quad \forall n \in (0,2)\ (2,\infty). \tag{5.49}$$

To further simplify, $V_n(r)$ can be normalized between 0 and 1 with a maximum and minimum distance (r_{max} and r_{min}, respectively) where the normalized potential function $U_n(r)$ would be 1 at the minimum distance and 0 at the maximum.

$$U_{rep}(r) = \frac{V_n(r) - V_n(r_{max})}{V_n(r_{min}) - V_n(r_{max})} = \frac{r^{n-2} - r_{max}^{n-2}}{r_{min}^{n-2} - r_{max}^{n-2}} \tag{5.50}$$

Figure 5.8 shows the result of Equation (5.50) with $1 \leq n \leq 5$. When $n = 2$, the denominator of Equation (5.50) goes to zero and produces a singularity, therefore Equation (5.46) is normalized and used in its place. As Figure 5.8 shows, an FOPF with a greater n will be more useful in dangerous cases and will apply a greater force sooner than an FOPF with a smaller n.

One additional advantage of the FOPF over other conventional PFs is that they are normalized and have maximum range. This will keep all PFs equal and unable to affect the agent if it is outside its range. For these reasons FOPFs are also used as attractive PFs. To find the attractive FOPFs, Equation (5.50) is mirrored around the x axis (Figure 5.9).

$$U_{att}(r) = -\frac{r^{n-2} - r_{max}^{n-2}}{r_{min}^{n-2} - r_{max}^{n-2}} \tag{5.51}$$

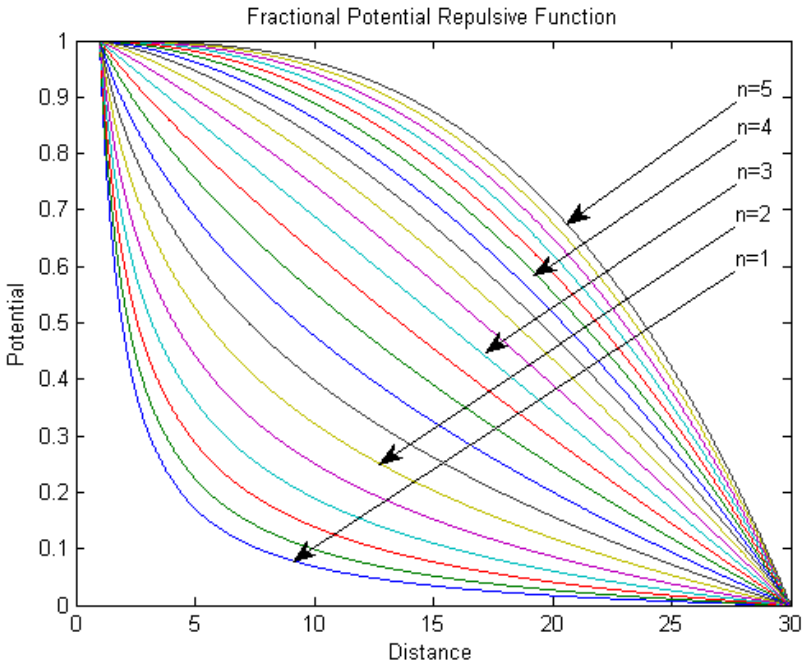

Fig. 5.8: Repulsive fractional order potential field ($1 \leq n \leq 5$).

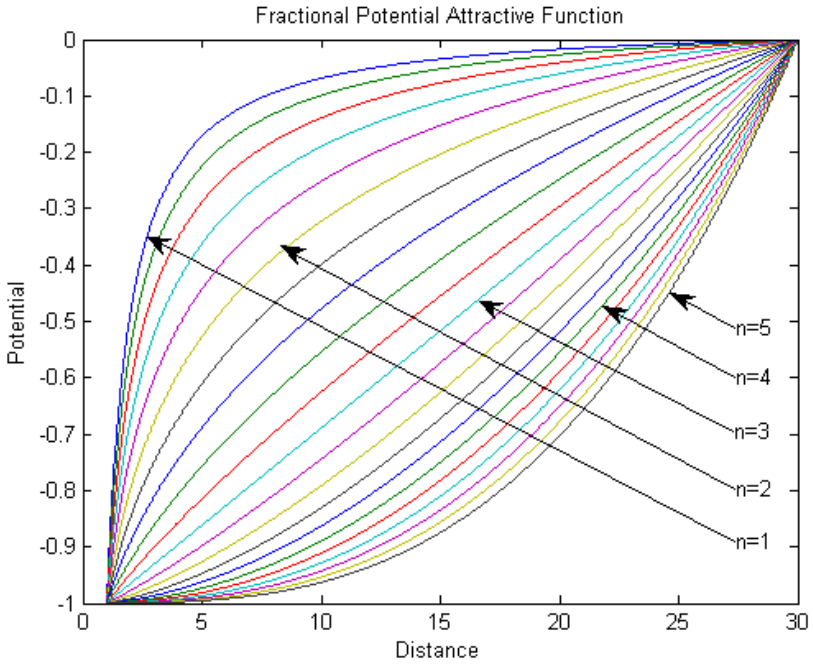

Fig. 5.9: Attractive fractional order potential field ($1 \leq n \leq 5$).

Navigation for Tag Estimation

Besides avoiding other UAs and staying within bounds, the main navigation objective is to fly in areas to improve the estimate of the tag position. Four methods are presented: The Attractive Method, the Repulsive Method, the Offset Repulsive Method, and the Dual-offset Repulsive Method.

Figure 5.10 shows a PF map for the Attractive Navigation method. In this method, a large attractive PF is formed at the estimated position of the tag. This draws the UAs to the estimated position (the center of the graph in Figure 5.10).

The Repulsive Method also has a large attractive field centered at the estimated position of the tag. However, it includes a small repulsive PF also centered at the estimated position of the tag. The attractive field draws the UAs in, and the repulsive field keeps them from getting close to the estimated position. Instead of going to the estimated position, they circle around it. Figure 5.11 shows the PF map for the Repulsive Method. The wide band 400m from the center of the map is where the repulsive field meets the attractive field.

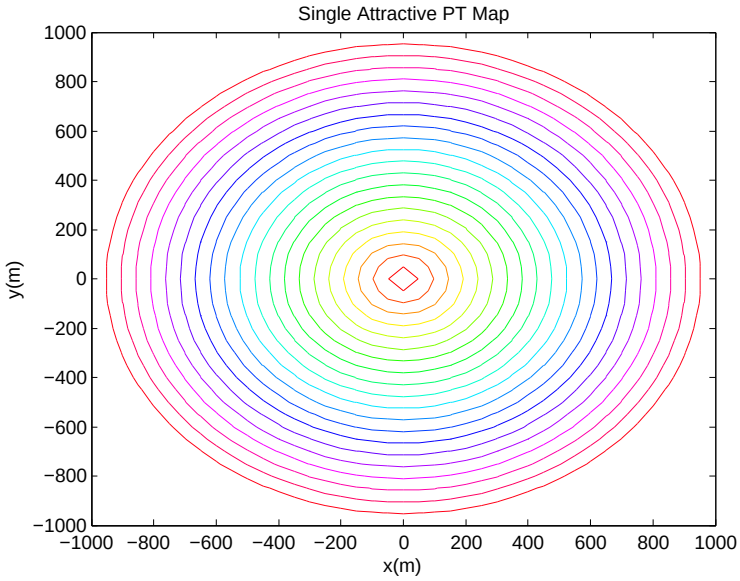

Fig. 5.10: Potential field map for the Attractive Method.

This is the area of least potential and the location the UAs will be attracted to.

The Offset Repulsive Method is identical to the Repulsive Method except the small repulsive field is centered around a point offset from the estimated position of the tag. Figure 5.12 shows an example of the Offset Repulsive Method. In this example, the repulsive PF is placed at an offset of 100m in the positive x direction. This offset creates the moon shaped area displayed in Figure 5.12 which the UAs are attracted to. The axis on which the offset is placed is dependent on the covariance of the estimate. If the offset is currently placed on the x-axis and the UAs are flying in that area, then the variance of the estimate along the x axis will decrease. Once it is 10% lower than the variance along the y axis, the offset will move clockwise to the y axis and the UAs will move with it. After a few iterations, the offset and the UAs will have made a full circle around the estimate in a clock-wise direction.

The Dual-offset Repulsive Method uses two repulsive PFs. Each one is offset an equal distance from the estimated position of the tag to create the map shown in Figure 5.13. In this specific example, the two offsets are placed 200m away from the estimate on the x-axis. This creates the two low-potential areas shown above and below the repulsive PFs on the y-axis. Like the Offset Repulsive Method, this method also chooses the axis to place the

offsets based on the variance of the estimation. If the variance along the x axis is too high, then the offsets will be placed on the y-axis to attract the UAs to the x-axis. This method might produce better results with multiple UAs than the Offset Repulsive Method since it encourages the UAs to spread out and fly in different areas.

5.2 Experimental Results

5.2.1 Flight Simulation

Figure 5.14 shows the map of the flight simulation environment. A border surrounds the flight area and has a potential field to keep the UAs inside. The tag is located in the middle of the map (0,0) and the boundary of the signal is indicated by the black dotted circle around the tag location. The location of the UAs are indicated on the map by a star symbol. The contours surrounding the UA are their potential fields and the blue line behind the UA is its track. The estimated location of the tag is drawn on the map by the 'o' symbol.

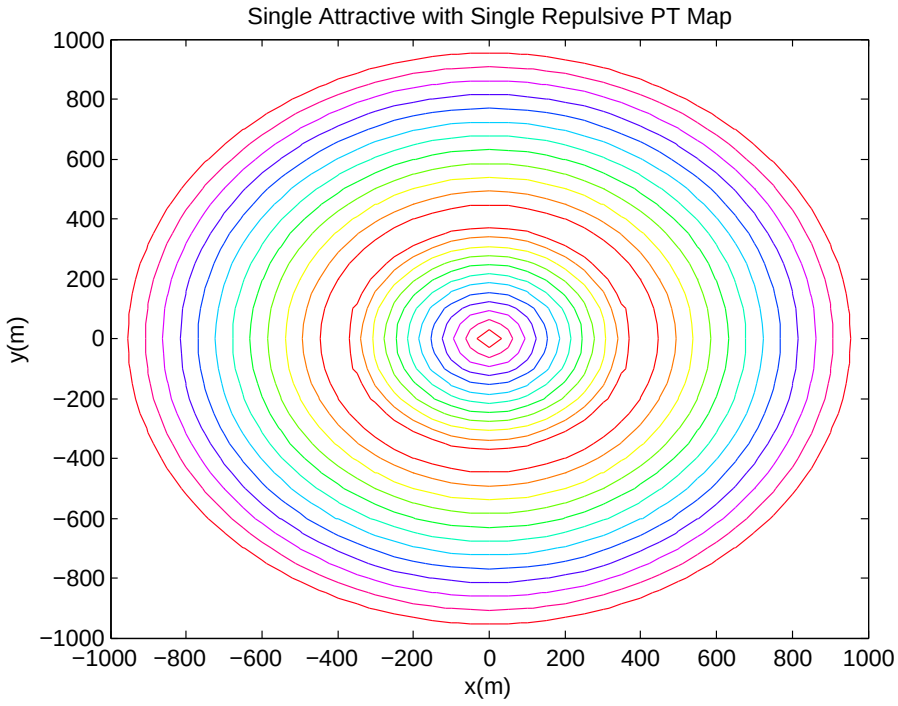

Fig. 5.11: Potential field map for the Repulsive Method.

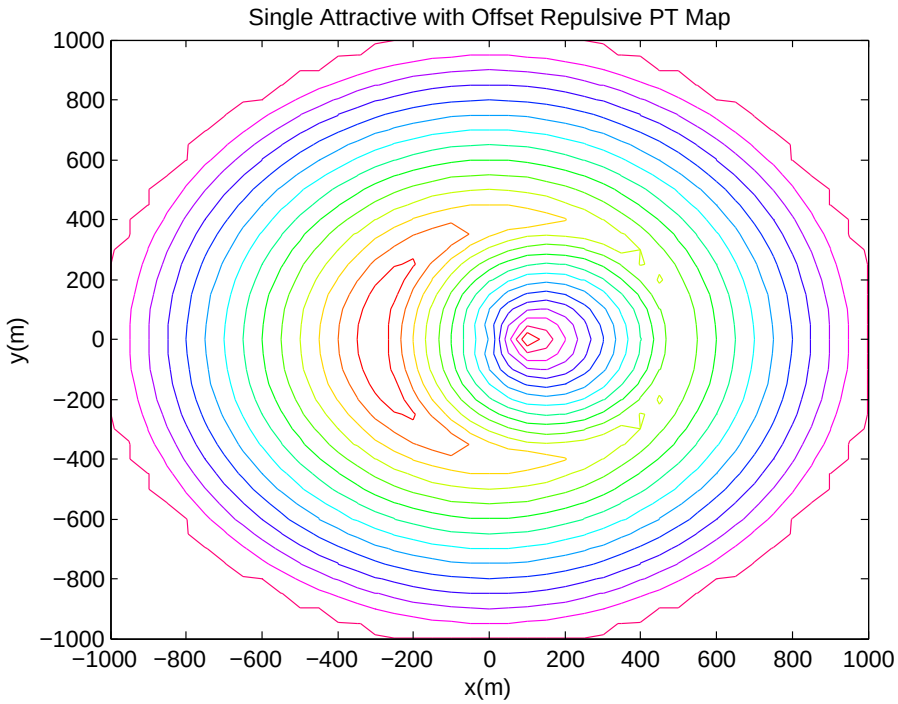

Fig. 5.12: Potential field map for the Offset Repulsive Method.

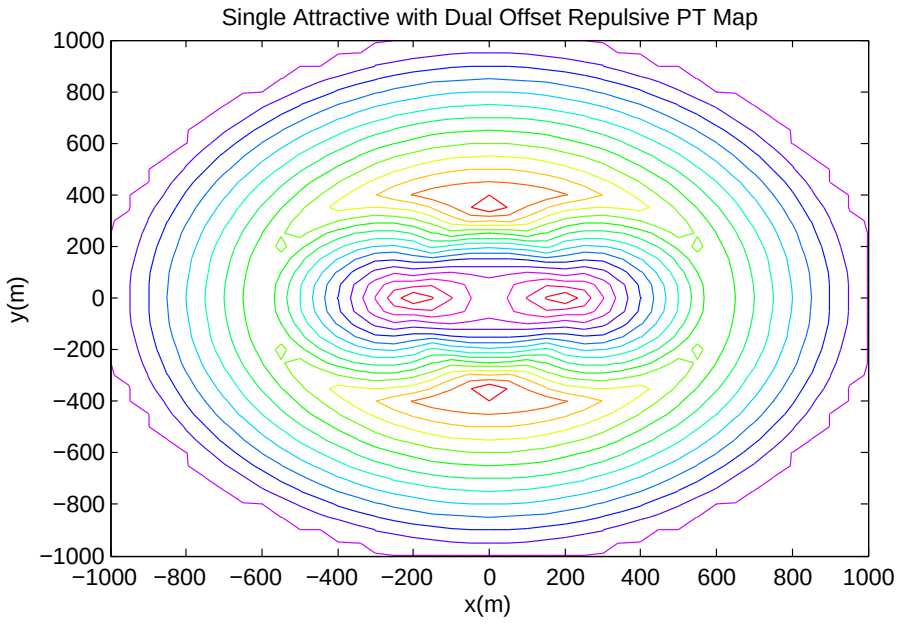

Fig. 5.13: Potential field map for the Dual-offset Repulsive Method.

The large contour lines centered at the estimated tag location are the potential fields of the estimate (Single Attractive Method). The covariance of the tag location estimate is also indicated on the map by the covariance ellipse drawn in black.

Initial simulations were ran to validate the real-world disturbances added to the simulation (e.g. wind, GPS error, etc.). Table 5.1 contains the values for the simulation parameters that were used for the following results.

Simulated Disturbance and Noise Results

Figure 5.15 shows an example of the position error of the UA in the x and y axis. As it shows, the simulation did well at creating conditions that a UA might encounter during flight.

The wind was also well simulated (Figure 5.16). This is even more apparent when looking at the plots of ground speed (Figure 5.17) and yaw vs. heading (Figure 5.18). As is expected under windy conditions, the ground speed is highly variable even though the airspeed was kept constant. The difference between the values for yaw and heading (crab

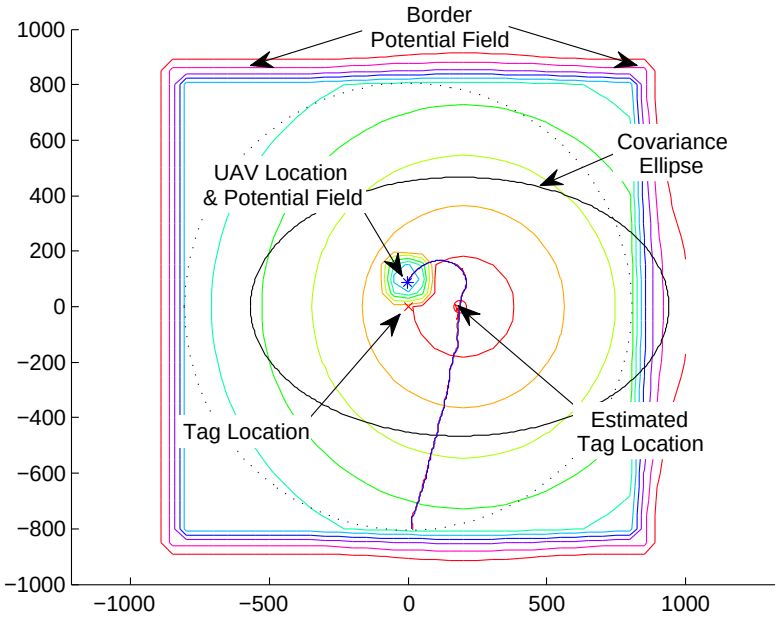

Fig. 5.14: Map for the fish-tracking flight simulation.

Table 5.1: Parameters for the fish-tracking flight simulation.

Symbol	Value	Description
dt	0.1	Simulation step size (s)
GPS_{dt}	1	GPS Measurement interval (s)
S_{dt}	4	Tag interval (s)
$3\sigma_x$	5	3-sigma value for GPS bias (m)
$3\sigma_y$	5	3-sigma value for GPS bias (m)
$3\sigma_\phi$	2	3-sigma value for heading process noise (degrees)
τ_x	10	Time constant for GPS bias in x (s)
τ_y	10	Time constant for GPS bias in y (s)
$\|W\|_0$	5	Nominal wind magnitude (m/s)
$3\sigma_{\|W\|}$	5	3-sigma wind magnitude bias (m/s)
$3\sigma_{\angle W}$	5	3-sigma wind direction bias (degrees)
$\tau_{\|W\|}$	50	Time constant for wind magnitude (s)
$\tau_{\angle W}$	50	Time constant for wind direction (s)
u_{max}	10	Max turning rate for UAs (deg/s)
k_i	10	Gain for heading controller
x_T, y_T	(0,0)	Position of tag
α_T	45	Polarization angle of tag
$3\sigma_s$	40.3	3-sigma value for signal strength noise

angle) also illustrates the success in modeling the wind.

Figure 5.19 shows a plot of the measured signal strength ($\tilde{S}$) vs. the signal strength without noise (f_s). A noisy, variable signal is expected given the noisy data acquired and the dependence on polarization angle.

PF Navigation Method Results

The Attractive PF Method is demonstrated in Figure 5.14. As expected, the UA is drawn toward the estimated position of the tag due to the large attractive field centered at the estimated position. Figure 5.20 shows a flight using the Repulsive Method. With this method, the UA is encouraged to circle around the estimated position; however, it can get turned around by the wind and blocked from covering the entire circle.

The Offset Repulsive Method (Figure 5.21) is more successful at directing the UA completely around the estimate. In addition, it yields an interesting variance plot (Figure 5.22) which shows "steps" of improvement in each axis when that particular axis is being worked on by the UA.

The Dual-Offset Repulsive Method yields similar results to the Offset Repulsive Method. Figure 5.23 shows how multiple UAs might behave with the two separate areas of low potential.

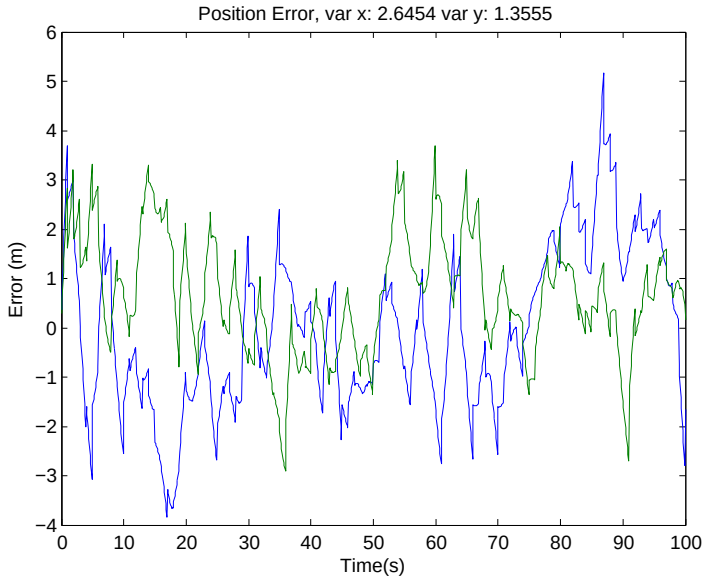

Fig. 5.15: Plot of UA position error in x and y.

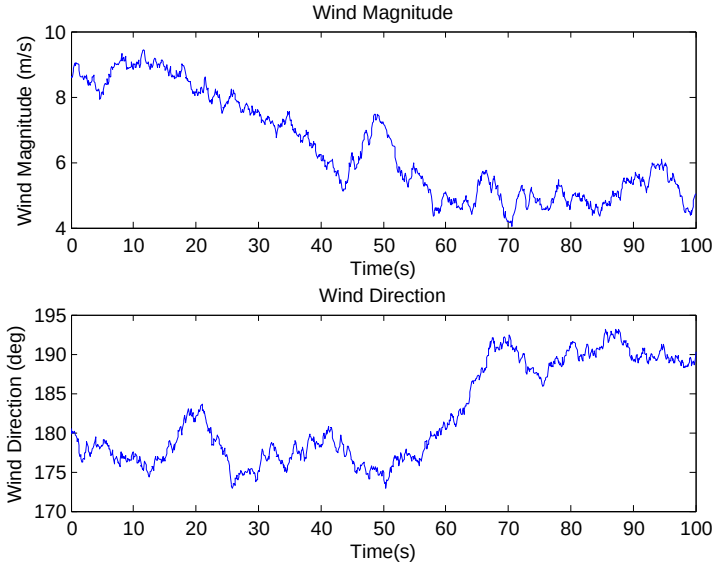

Fig. 5.16: Plot of wind magnitude and direction.

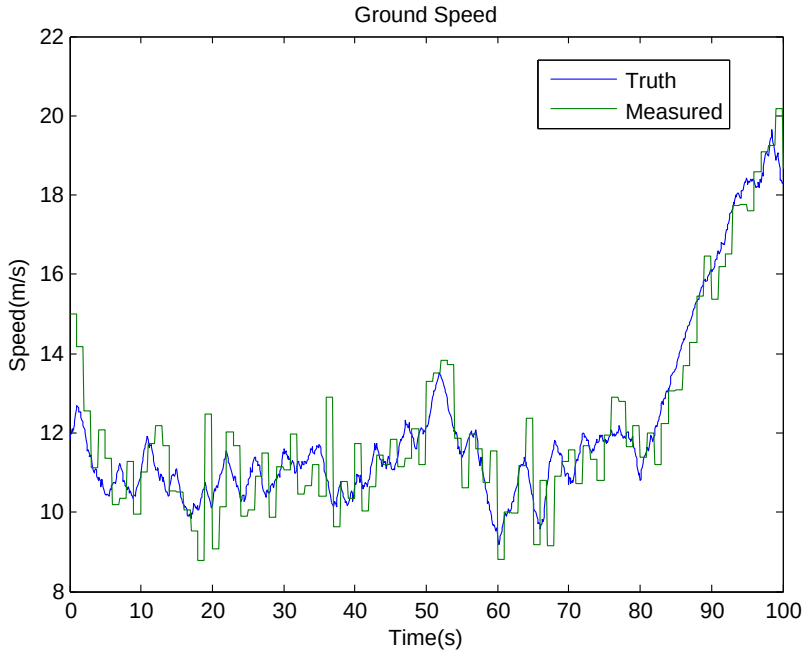

Fig. 5.17: Plot of actual and measured ground speed.

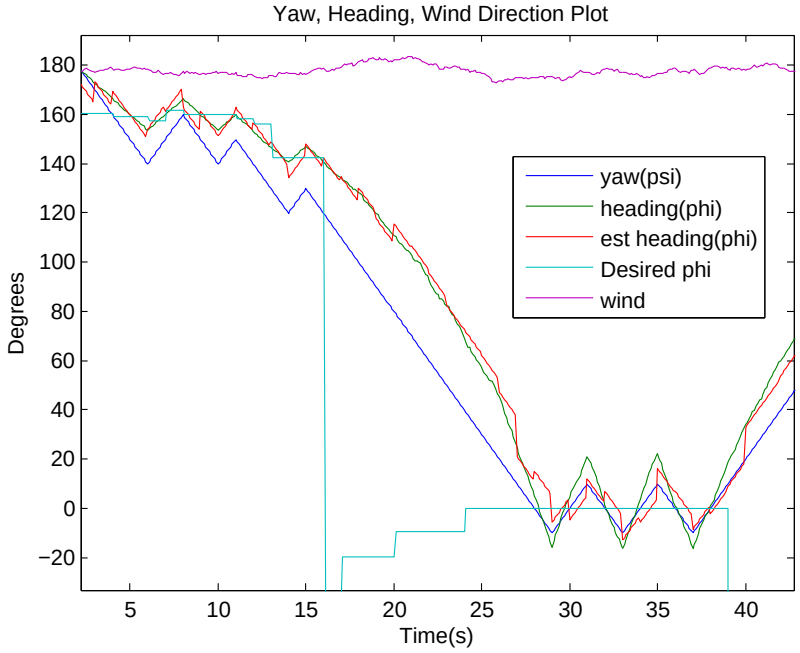

Fig. 5.18: Plot of yaw, heading, and wind direction.

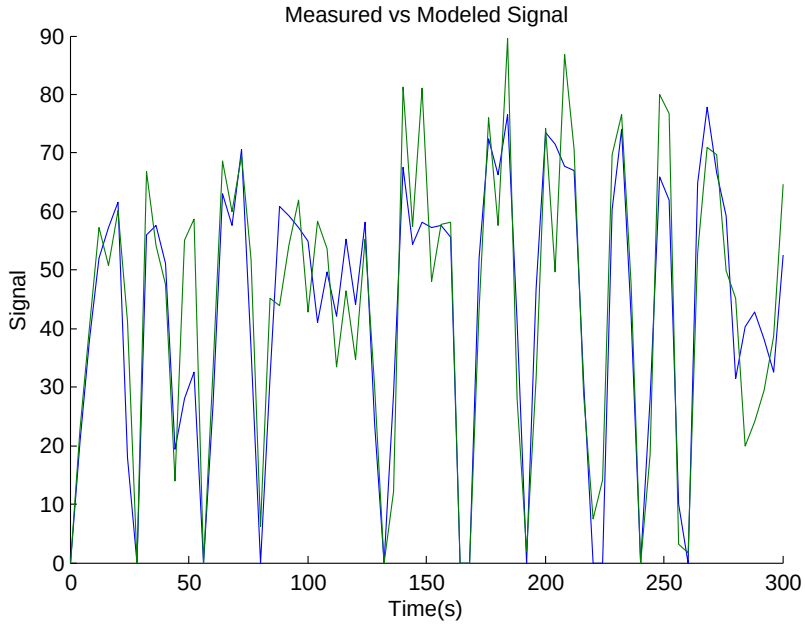

Fig. 5.19: Plot of measured and modeled signal strength.

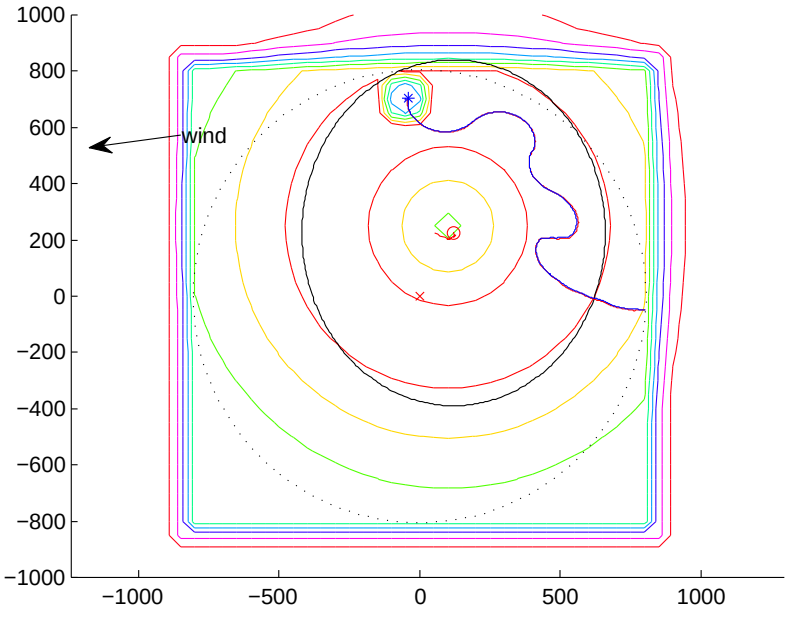

Fig. 5.20: Simulation results for the Repulsive Method.

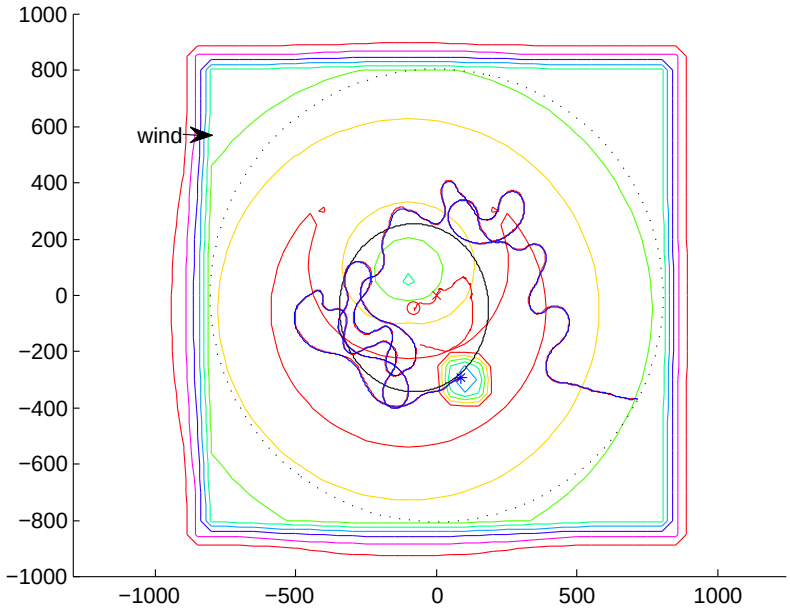

Fig. 5.21: Simulation results for the Offset Repulsive Method.

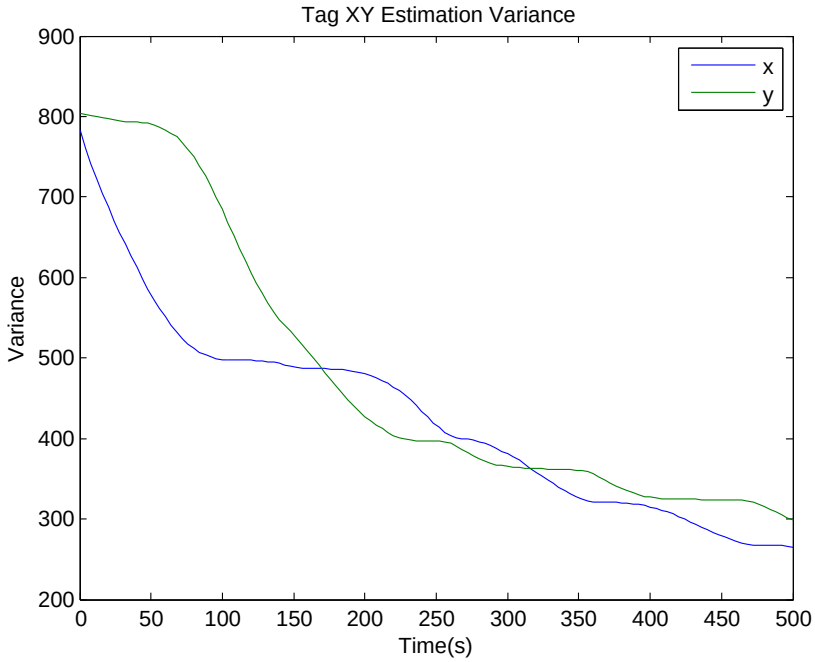

Fig. 5.22: Tag position variance plot for the Offset Repulsive Method.

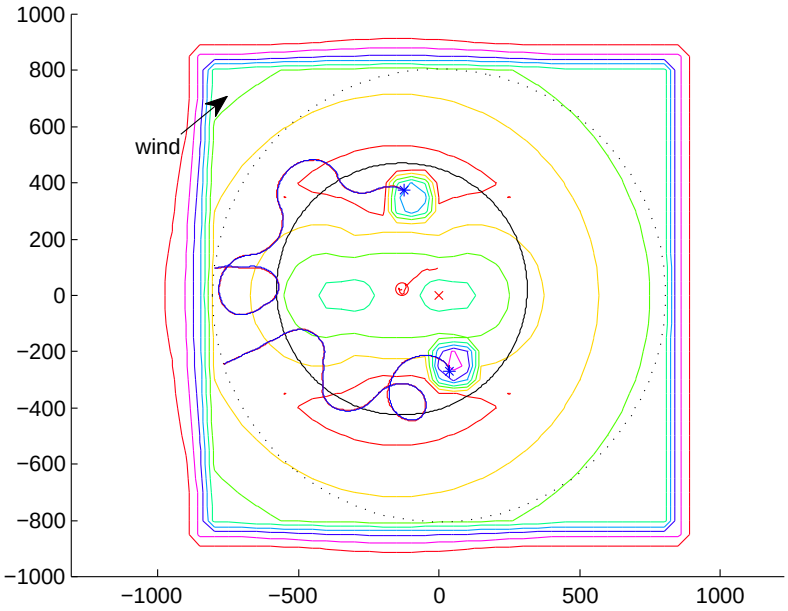

Fig. 5.23: Simulation results for the Dual-offset Repulsive Method (2 UAs).

5.2.2 Monte Carlo Simulations

Table 5.2 shows the results of the Monte Carlo Simulations. The mean, the 3-sigma values, and the 99% chi-squared confidence interval for the 3-sigma values are listed for all four methods. Each method was also simulated with one, two and three UAs.

With a higher mean and 3-sigma value than any of the others, the Attractive method seems to be the worst option. Focusing on the other three methods and the simulations with just one UA, the following observations should be noted.

1. The two offset methods have very similar results and have a lower mean value than the Repulsive Method.

2. The Repulsive Method may have a higher mean than the offset methods, but the upper 3-sigma value is lower.

3. The Repulsive Method is the only one that has a lower 3-sigma value greater than zero.

Table 5.2: Monte Carlo simulation results for tag error dispersion and 100 flights (meters).

Method	# of UAs	Final Mean	Upper 3-sig	Lower 3-sig	Chi-2 Spread
Att	1	274	671	0	149
Rep	1	251	343	159	35
Offset	1	160	408	0	93
Dual	1	160	360	0	76
Att	2	249	577	0	123
Rep	2	256	325	187	27
Offset	2	168	411	0	98
Dual	2	186	436	0	101
Att	3	234	572	0	127
Rep	3	255	318	192	27
Offset	3	186	443	0	111
Dual	3	190	471	0	108

4. The Repulsive has the smallest gap between the mean and the 3-sigma values and the smallest Chi-2 spread.

The conclusion from these observations is that while the offset methods may achieve higher accuracy estimates, they are less precise and have higher uncertainty. The Repulsive Method may not be able to achieve errors as low as the Offset Methods, however is much more reliable. The error trajectory plots of the Repulsive Method and the Offset Method also confirm this conclusion (Figures 5.24 and 5.25)

The table also shows that with the Attractive and Repulsive methods, having multiple UAs improved the estimation performance. The opposite is true with the Offset and Dual-offset methods; they performed worse with more than one UA. Even so the general improvement shown in the table from multiple UAs is not great. The greatest contribution that multiple UAs made to the estimate is illustrated in the error trajectory plots. Figure 5.26 shows the trajectory plot for the Repulsive Method and three UAs. Compared to the Repulsive plot with one UA (Figure 5.24), the plot with three UAs converges ten times faster than the plot with one UA. Even though using multiple UAs did not improve the error in the estimate, they can be used to find the tag in shorter time.

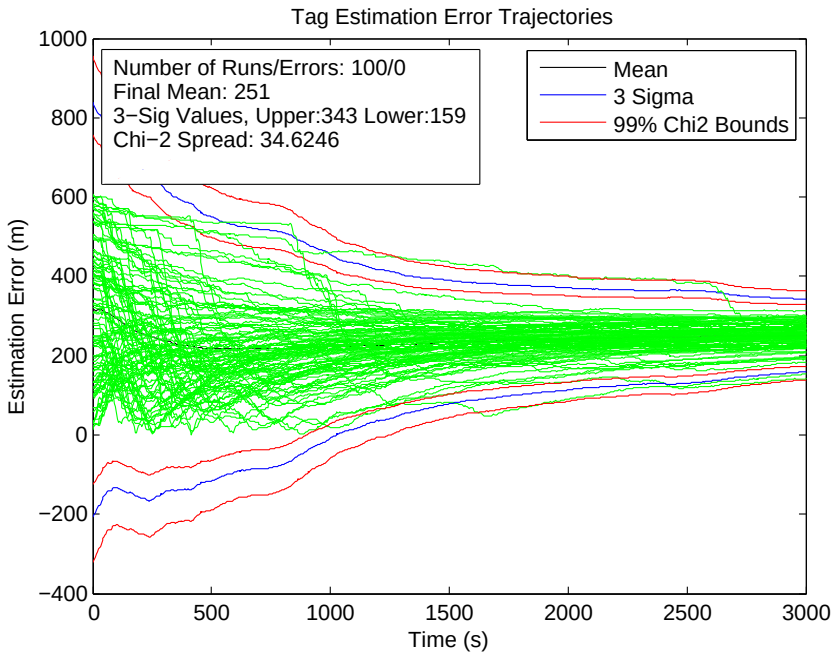

Fig. 5.24: MC simulation with 1 UA using Repulsive Method.

5.2.3 Summary

The simulation proved successful at implementing real-world disturbances like GPS bias, a variable ground speed, and a crab angle. The estimation of the tag was also successful despite the noisy signal and the simplified measurement model. The Monte Carlo analysis showed that the Offset and Dual-offset Methods could estimate the tag with the highest accuracy but also with the highest variability. The Repulsive Method was not able to estimate with the same accuracy but was very consistent. The use of multiple UAs did not improve the estimation accuracy; in some cases, it made the estimates worse. However, multiple UAs were able to find the tag ten times faster than a single UA.

Future work includes sensitivity analysis to figure out which error sources are major contributors to the tracking error. With this information, meaningful improvements can be made on the platform to increase the accuracy. A well-tuned heading controller or wind compensation could also increase the accuracy. Future work also includes looking at ways to improve accuracy while using multiple UAs. This could possibly be achieved by keeping the UAs in formation and by giving each its own unique antenna configuration.

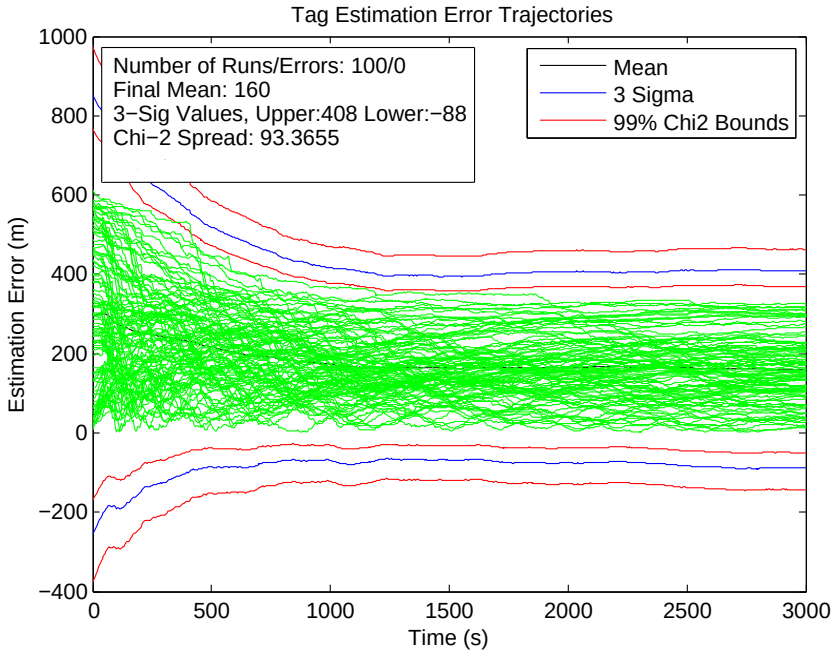

Fig. 5.25: MC simulation with 1 UA using Offset Repulsive Method.

5.3 Chapter Summary

This chapter illustrated how The Processing Cycle for Meaningful Remote Sensing can be used in real-time to provide feedback to the end user and to improve the accuracy of the actionable information. Simple, novel methods for radio-localization and multi-UA navigation were presented and tested using a real-world simulation scenario. Monte Carlo analysis was used to compare different navigation methods and to determine what expected performance would be in real-world situations. Improvements could be made, either in the payload or with the navigation methods, by doing a sensitivity analysis to find out which error sources are major contributors to the tracking error.

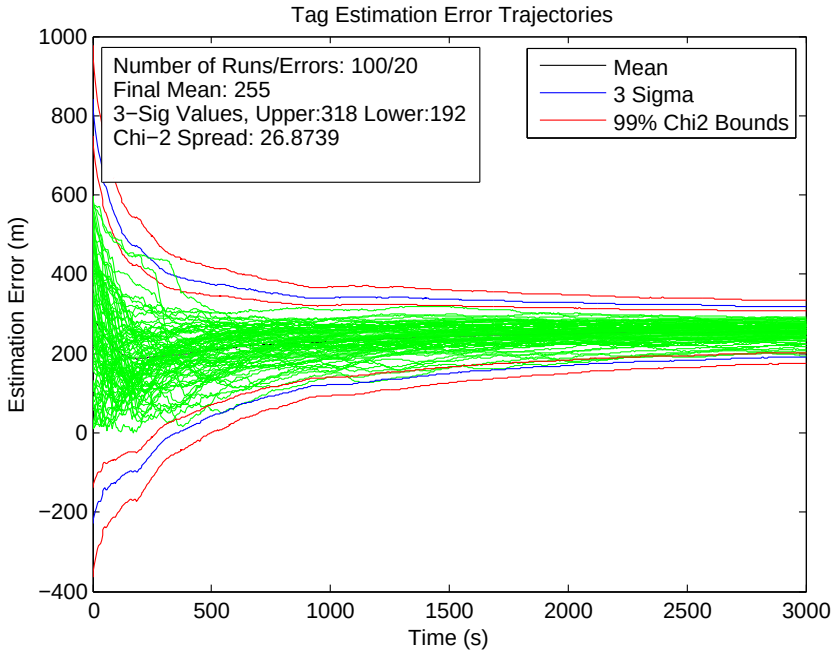

Fig. 5.26: MC simulation with 3 UA using Repulsive Method.

Chapter 6

Delivering Actionable Information

Previous chapters have shown how imagery can be captured, georeferenced, and calibrated from small UAS with consumer-grade cameras. However, the Processing Cycle for Meaningful Remote Sensing has not been completed. The last step, Application Processing, converts the scientific data into actionable information which is used by the end user. If this step is not done correctly and the data given to the end user is not useful, then there is no point in gathering the data in the first place. This chapter shows a few examples of how imagery from VIS-NIR and TIR cameras were used to provide actionable information for applications in vegetation mapping, precision agriculture, and fish habitat.

6.1 Vegetation Mapping

One of the great uses for VIS-NIR imagery is vegetation mapping. The red, green, blue, and NIR spectral bands of the VIS-NIR imagery contains a spectral fingerprint that can be used to classify the imagery into different types of vegetation [38]. This tool is very useful especially in managing problematic invasive plant species like *Phragmites Australis*. Imported from Europe over a hundred years ago, this aggressive grass species is invading wetlands across North America [63]. This causes many problems including displacing native vegetation [64], loss of flora and fauna, alternations to wetland nutrient cycling, and loss of habitat for many animals including birds [64–67]. At the Bear River Migratory Bird Refuge (BRMBR) in northern Utah, *Phragmites Australis* creates an issue for migratory birds on the Pacific Flyway which depend on this area as a resting stop [68]. To help control *Phragmites Australis* wetland managers could really benefit from having maps which show where it is, how it is growing, and which native plants are being replaced.

In 2010 and 2011, AggieAir was used to provide this information to wetland managers

[68]. VIS-NIR images of a 12-square mile area were captured, orthorectified, and calibrated using reflectance panels on four separate occasions over the summer. During the flight a ground crew identified ground features including *Phragmites australis*, water, road, etc. and surveyed the features using a survey grade GPS receiver. The calibrated VIS-NIR mosaics and the ground samples were then used to train a multiclass relevance vector machine (RVM) to classify the entire area. Figure 6.1 shows VIS-NIR mosaics with the resulting classified image.

The classified image in Figure 6.1 is a form of actionable information which can be used by wetland managers to help manage *Phragmites australis*. However since a series of images were acquired, mosaiced, and classified, change detection was used to show growth over the season (Figure 6.2). This additional actionable information can be used by the wetland managers to plan for future removal administration.

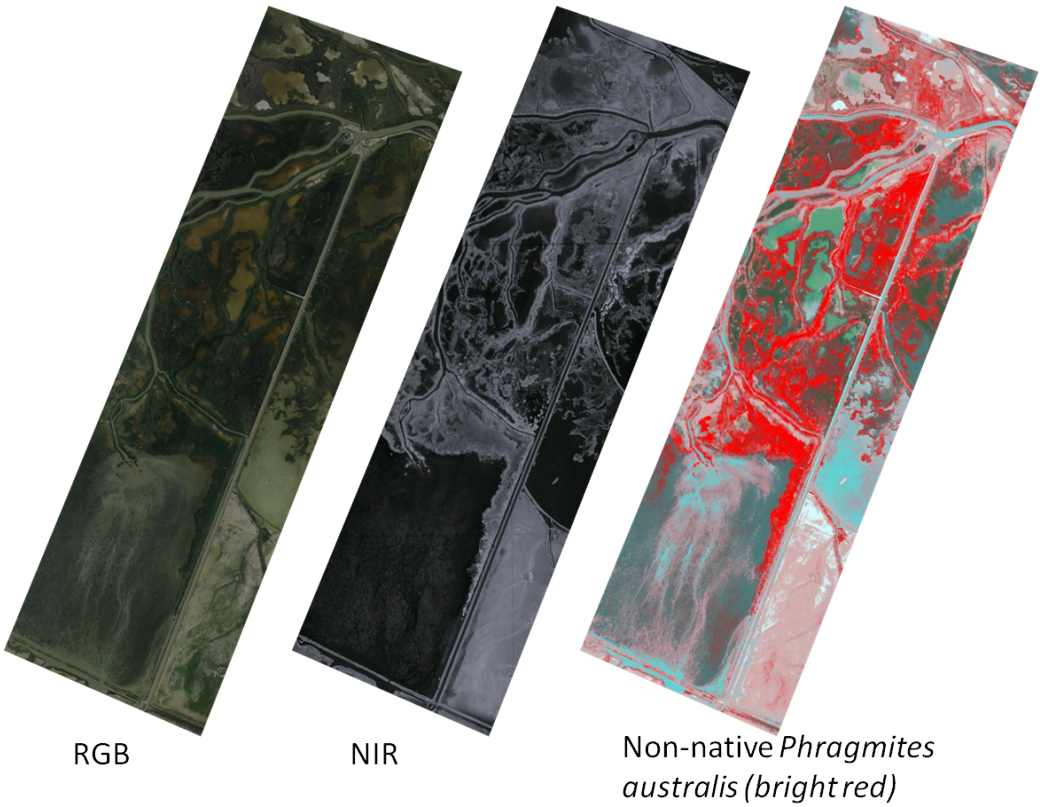

Fig. 6.1: VIS-NIR mosaics and a classified image of *Phragmites Australius*.

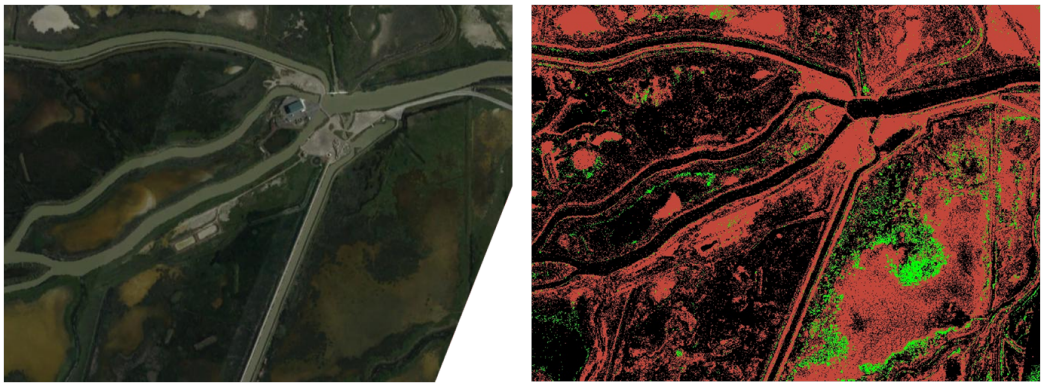

Fig. 6.2: A series of vegetation maps can be used for change detection.

6.2 Precision Agriculture

Precision agriculture is a process of using large quantities of data in order to make precise adjustments to agricultural inputs such as water and nutrients. Data from remote sensing sources can be very valuable to precision agriculture [69–72], and remotely sensed data from UAS can add even more value due to the high-resolution and flexible nature of UAS. This was demonstrated in 2013 using AggieAir by flying over a small farm with two center pivots five times over the course of two months [73, 74]. In addition to collecting VIS-NIR imagery, TIR imagery was also collected for precision agriculture since it is very important and includes data related to soil moisture and evaoptranspiration. This data was converted into georeferenced scientific data using the techniques previously outlined and used to generate maps with actionable information. Figure 6.3 shows the VIS-NIR and TIR mosaics of the area for one of the flights. To help generate the actionable information, index maps such as the Normalized Difference Vegetation Index (NDVI) and Leaf Area Index (LAI) are generated using the VIS-NIR mosaics (Figure 6.4). These maps are easy to generate and do not represent anything physical; however they add additional sets of data that are used when generating other maps.

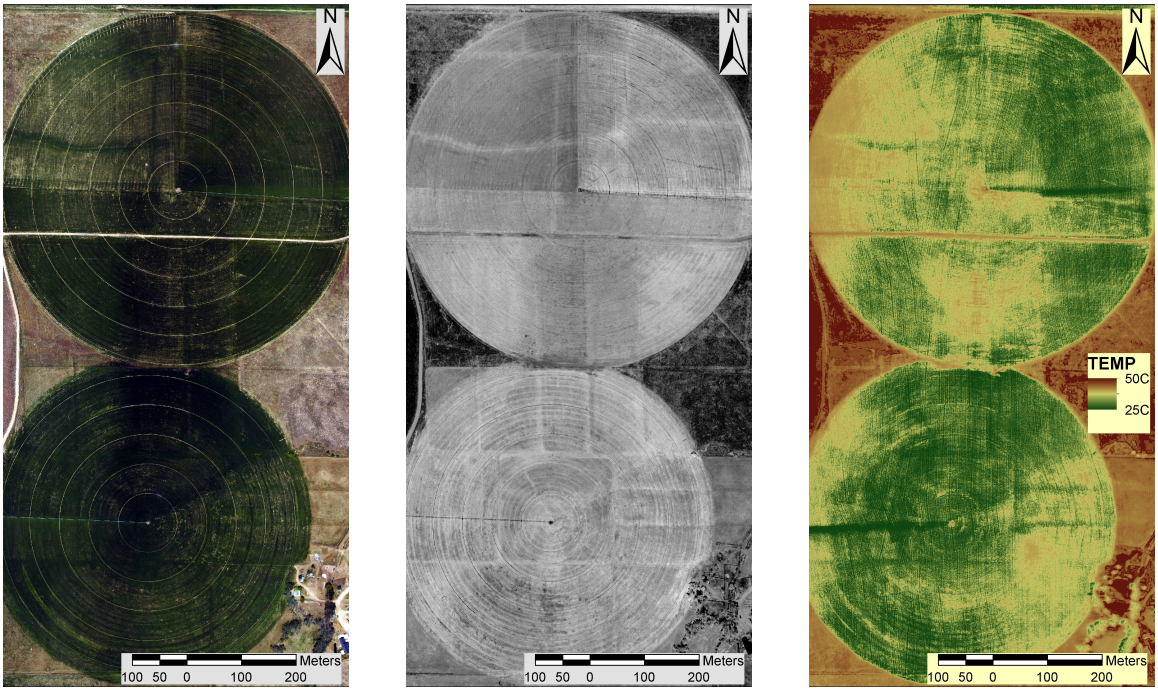

Fig. 6.3: VIS-NIR and thermal mosaics of two center pivots.

Figures 6.5, 6.6, and 6.7 show the results from the AggieAir fights. Figures 6.5 and 6.6 show the chlorophyll and nitrogen content of oats five weeks after germination and during early flowering. Maps like these are used to quantify plant health and can be used for yield predictions and to tell the farmer where and how much fertilizer to apply. Figure 6.7 is a map of evapotranspiration and describes how much water is being transpired from the plant; the methods used to generate this map is widely used with satellite data [75] but has shown good performance using the data from AggieAir. Similar methods can also be used to estimate and forecast soil moisture which could be used when scheduling irrigation.

Many might call results like these sufficiently simplified for use in routine precision agriculture. However further simplification is needed to reduce the data to fit the growers form of actuation. If the grower uses a center pivot to irrigate, the data would need to be presented in a way that the could be implemented on the pivot (e.g. when to turn it on and how fast it should run). If the grower uses flood irrigation, the data might need to be simplified even further to show which days to irrigate and which not to. Even though the results presented in this section are arguably not yet actionable, they are still very

impressive given the low-cost, and high-spatial and temporal resolutions. More work is being done in order to close the loop on precision agriculture.

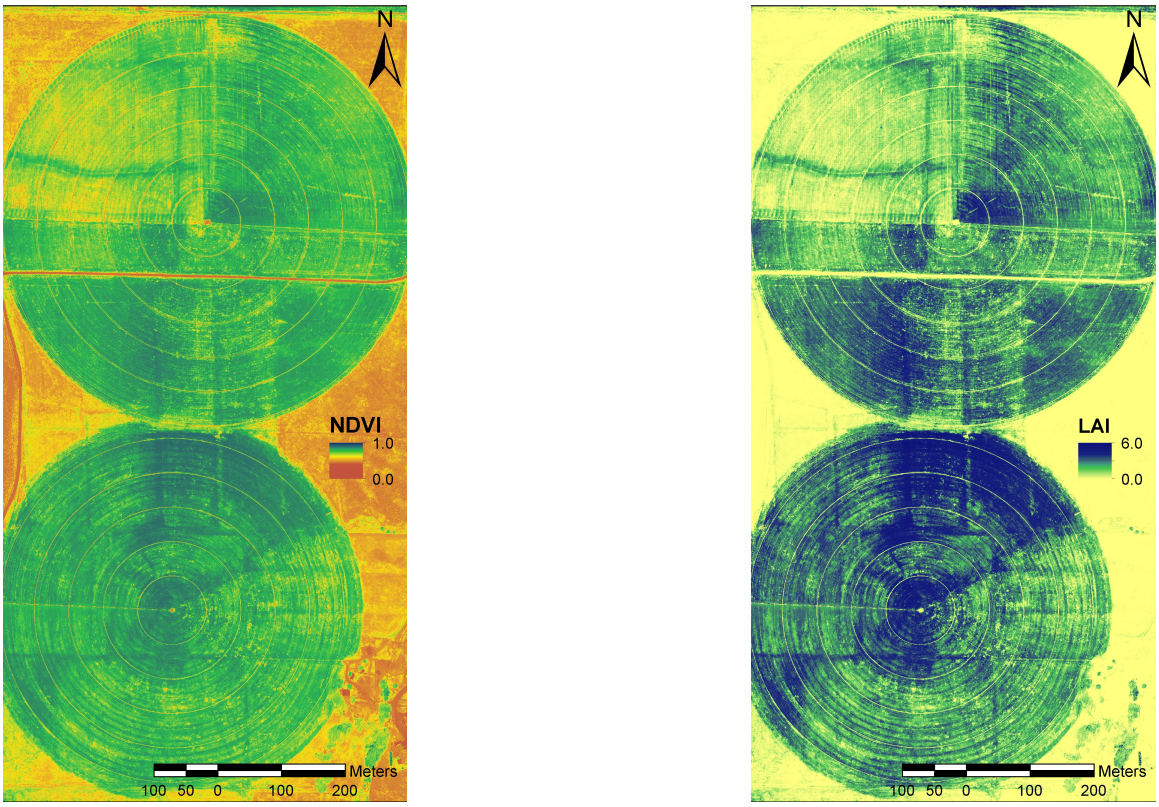

Fig. 6.4: NDVI and LAI maps of two center pivots.

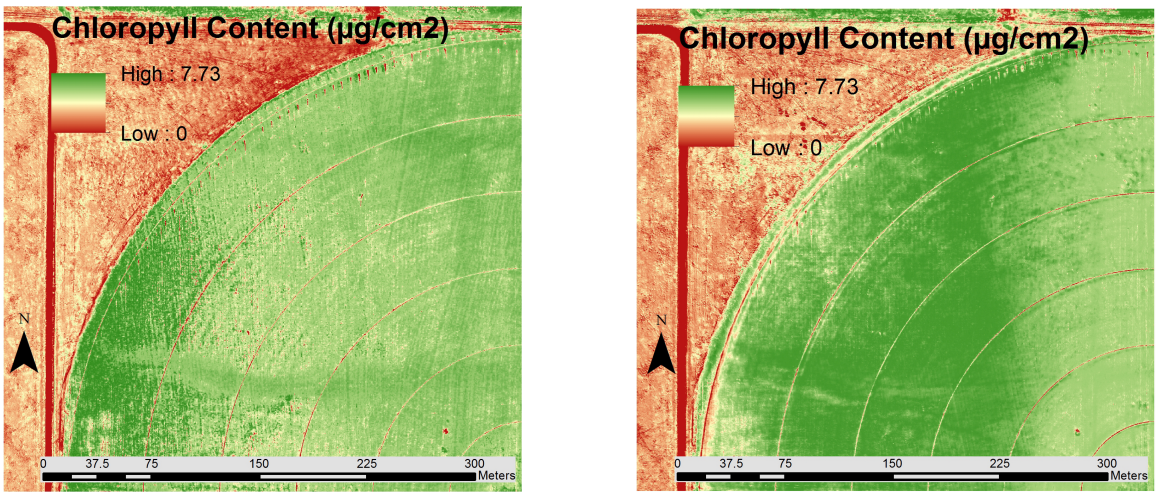

Fig. 6.5: Chlorophyll maps of oats five weeks after germination and early flowering.

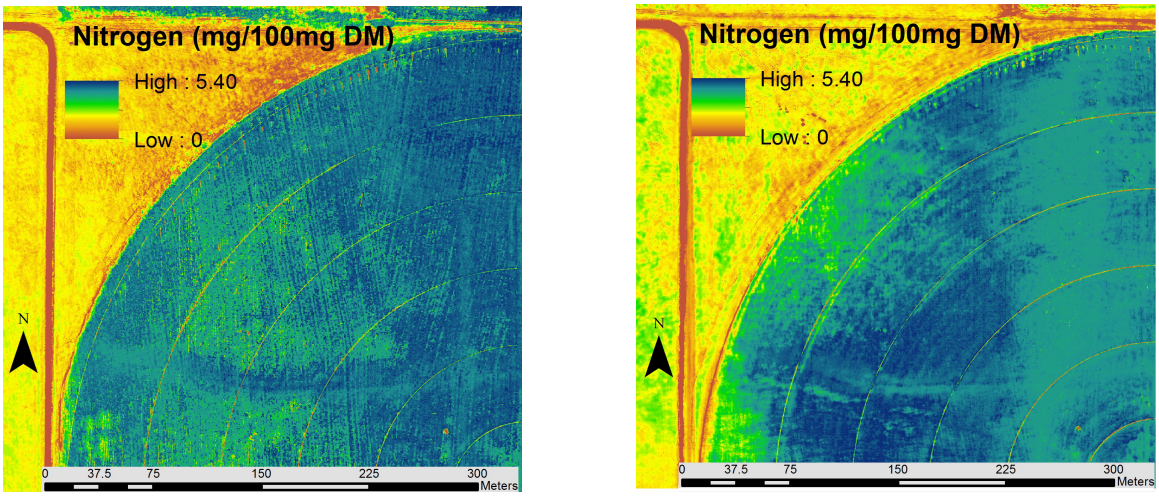

Fig. 6.6: Nitrogen maps of oats five weeks after germination and early flowering.

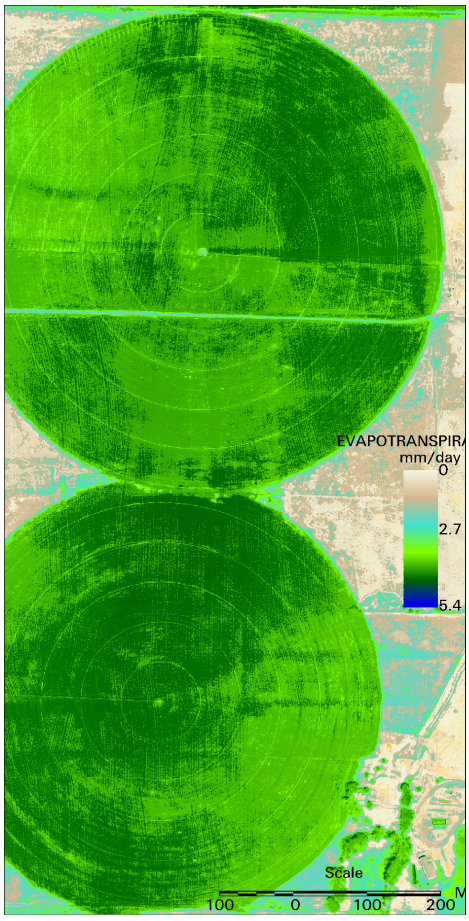

Fig. 6.7: Evapotranspiration maps of two center pivots.

6.3 Fish Thermal Refugia

Temperature is a critical physical characteristic of aquatic systems due to its relationship with chemical and biological reaction rates, and with aquatic species that are sensitive to temperature. Attempts to quantify processes influencing temperature regimes commonly include field based measurements at discrete locations that are often used to support instream temperature modeling [76]. More recently, spatially representative observations from distributed temperature sensing applications have been utilized in modeling efforts [77]. A growing body of literature has illustrated the utility of high resolution remotely sensed TIR imagery for mapping spatial temperature patterns in streams and rivers [15, 78] that provide information to identify biologically important areas such as thermal refugia [14] or to understand the effects of land management practices on stream temperature [79]. The use of thermal imagery to support temperature instream modeling has been shown to provide important information regarding system behavior [80], however, the utility of these data types in modeling is limited by the temporal, and at times the spatial resolution, of the data.

To test the utility of AggieAir for the thermal refugia application, AggieAir was flown over a river with significant ongoing research regarding changing temperature regimes within the river. Visual, NIR, and thermal images were all acquired and stitched together into separate orthorectified mosaics (Figure 6.8).

Since this application only requires stream temperature, it is necessary to separate the stream from land in the thermal mosaic. The NIR mosaic is very effective in mapping the banks of the river since water absorbs NIR light well. This makes water appear very dark in the imagery and allows us to easily delineate between water and land. The visual and thermal mosaics are also used to help map the banks of the river. After the stream is digitized, it can be used to remove the land and vegetation from the thermal mosaics (Figure 6.9). Removing the land is an important part of generating actionable information because the data is more focused toward what is really needed by the end user. In addition since the thermal mosaic only includes water, it can easily be corrected for emissivity and

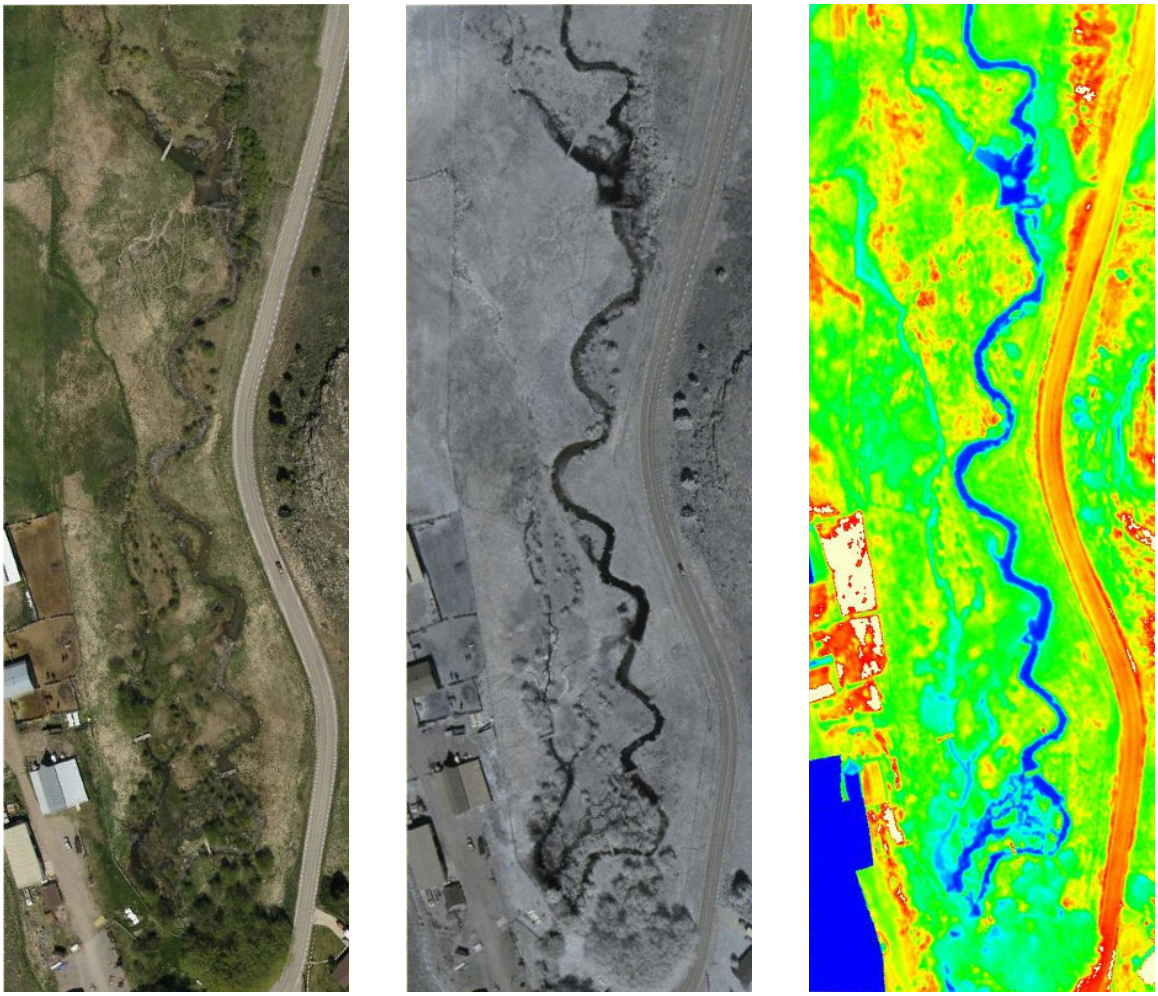

Fig. 6.8: VIS-NIR and thermal mosaics of river.

calibrated using temperature probes within the river.

6.4 Cyber Physical System Based on small UAS-Based Remote Sensing

The Processing Cycle for Meaningful Remote Sensing is part of a larger Cyber Physical System (CPS). A CPS is a system which includes hardware and software to provide sensing and actuation to a large scale closed-loop system to manage high-level complex systems [81]. A good example of a CPS is precision agriculture. The UAS acts as a sensor and provides actuators (automated center pivots, autonomous tractors) with data they can use to control complex systems such as soil moisture or plant nitrogen content. The Processing Cycle for Meaningful Remote Sensing is actually software that simply takes the data from the UAS

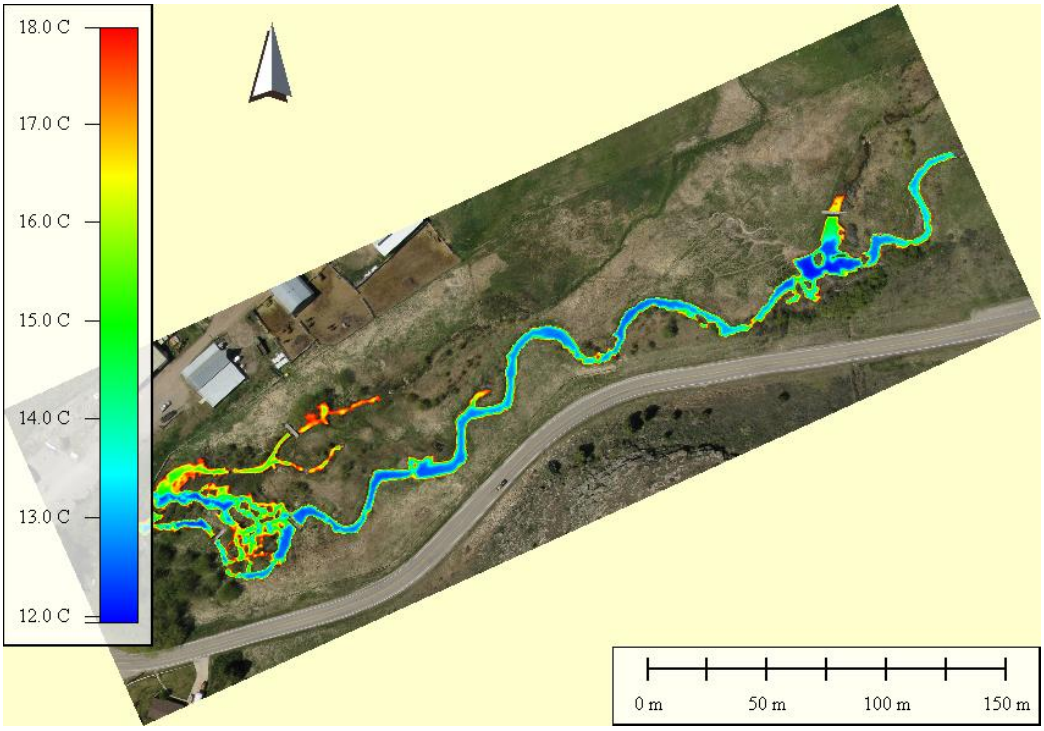

Fig. 6.9: Thermal mosaic of river displayed over visual mosaic.

and converts it in a form which can be understood by the actuators. Another example of a CPS is using multiple UAs for diffusion control in diffusion processes such as chemical and radiation leaks [82]. In this case, a group of sensor UAs could be used to measure the diffusion process while another group of actuation or sprayer UAs could be used to release chemicals to control the diffusion process.

6.5 Chapter Summary

This chapter showed some examples of how the Processing Cycle for Meaningful Remote Sensing can be completed by proving actionable information to the users and how this process is related to a CPS. For vegetation mapping, AggieAir VIS-NIR imagery was used to map an invasive plant species to help wetland managers manage the species. In addition, a series of images were captured over the growing season and change detection was used to map how the invasive plant species was growing. In precision agriculture, AggieAir VIS-NIR and TIR imagery was captured over two center pivots and used to generate maps of

plant chlorophyll, plant nitrogen, and evapotranspiration. While this data could be used as actionable information to know where to apply nitrogen or where to water, more work is still needed to simplify the data in a form that can be used by growers. Finally, an application in mapping fish habitat was included. This showed how VIS-NIR imagery can be used to map a river channel to simplify TIR imagery by removing the land so just the surface temperature of the river is left: thereby giving biologists actionable information about thermal refugia for fish.

Chapter 7

Conclusions and the Future of Small UAS Remote Sensing

This dissertation has shown how raw data from consumer-grade sensors can be acquired using a small unmanned aerial system (UAS), AggieAir, and converted to georeferenced scientific-grade data. Chapter 3 reviewed literature for the different processes used to convert digital numbers (DN) from visual and near-infrared (VIS-NIR) cameras into radiometric values of reflectance, where the process used by AggieAir was emphasized. The methods used to geometrically calibrate the camera and to create an orthorectified mosaic were also covered in Chapter 3, but also apply to processing images from a thermal-infrared (TIR) camera in Chapter 4. However, since the thermal camera is radiometric and outputs calibrated temperature, additional steps are presented to prepare the images for orthorectification. In addition, since a TIR camera is not sensitive to changes in color, a different calibration target is presented for geometrically calibrating the TIR camera. Special focus in Chapter 4 was made in Section 4.3 where the issues with external disturbances on the TIR camera is addressed. In order to calibrate for and model these external disturbances, two new ground sampling techniques are introduced, tested, and evaluated. Finally, Chapter 5 presents novel methods for tracking fish using biotelemetry and shows how the conversion from raw data into georeferenced scientific data can happen in real-time to give feedback to the UAS for navigation.

More work can be done in order to improve the data quality even further. One piece missing from the VIS-NIR processing chain includes a spectral calibration of the consumer-grade cameras. Knowing the spectral sensitivity of these cameras will help improve the radiometric calibration. While the ground sampling techniques worked well to calibrate the TIR imagery from the aircraft, more data should be gathered in order to model the external disturbances and remove the need for ground sampling. Since the biotelemetry fish

tracking application is still in its infancy, lots of work is needed to be done before this is made for routine use. Additional simulations are needed to perform sensitivity analysis and find out ways to improve the accuracy of the tag location estimation. At that point, the navigation routines need to be implemented in the autopilot and real-world experiments should be conducted under different scenarios to prove the system.

There is a lot of potential for using small UAS as a remote sensing platform. They have proved very useful in delivering quality data for many applications including vegetation mapping, fish habitat mapping, and precision agriculture. Perhaps if The Processing Cycle for Remote Sensing becomes more automated and actionable information can be delivered at the click of a button, small UAS will enable remote sensing to become "personal." And like personal computers or phones, many will be able to use small UAS to improve their everyday lives.

References

[1] R. Benedetti and P. Rossini, "On the use of NDVI Profiles as a Tool for Agricultural Statistics: The Case Study of Wheat Yield Estimate and Forecast in Emilia Romagna," *Remote Sensing of Environment*, vol. 45, no. 3, pp. 311–326, Sept. 1993.

[2] B. Rudorff and G. Batista, "Yield Estimation of Sugarcane Based on Agrometeorological-Spectral Models," *Remote Sensing of Environment*, vol. 33, no. 3, pp. 183–192, Sept. 1990.

[3] M. L. Stone, J. B. Solie, W. R. Raun, R. W. Whitney, S. L. Taylor, and J. D. Ringer, "Use of Spectral Radiance for Correcting in-season Fertilizer Nitrogen Deficiencies in Winter Wheat," *Transactions of the American Society of Agricultural and Biological Engineers*, vol. 39, no. 5, pp. 1623–1631, 1996.

[4] R. D. Jackson, S. B. Idso, R. J. Reginato, and P. J. Pinter, "Canopy Temperature as a Crop Water Stress Indicator," *Water Resources Research*, vol. 17, no. 4, p. 1133, 1981.

[5] A. Mathur and G. M. Foody, "Crop Classification by Support Vector Machine with Intelligently Selected Training Data for an Operational Application," *International Journal of Remote Sensing*, vol. 29, no. 8, pp. 2227–2240, Apr. 2008.

[6] J. Franke and G. Menz, "Multi-temporal Wheat Disease Detection by Multi-spectral Remote Sensing," *Precision Agriculture*, vol. 8, no. 3, pp. 161–172, June 2007.

[7] S. Thomson, L. Smith, J. Ray, and P. Zimba, "Remote Sensing and Implications for Variable-rate Application Using Agricultural Aircraft," in *Proceedings of Society of Photographic Instrumentation Engineers*, vol. 5153, 2004, p. 13.

[8] N. Coops and P. Catling, "Predicting the Complexity of Habitat in Forests from Airborne Videography for Wildlife Management," *International Journal of Remote Sensing*, vol. 18, no. 12, 1997.

[9] R. D. Wulf and R. Goossens, "Remote Sensing for Wildlife Management: Giant Panda Habitat Mapping from LANDSAT MSS Images," *Geocarto International*, vol. 3, no. 1, 1988.

[10] J. H. Everitt, C. Yang, R. S. Fletcher, C. J. Deloach, and M. R. Davis, "Using Remote Sensing to Assess Biological Control of Saltcedar," *Southwestern Entomologist*, vol. 32, no. 2, pp. 93–103, June 2007.

[11] P. H. Evangelista, T. J. Stohlgren, J. T. Morisette, and S. Kumar, "Mapping Invasive Tamarisk (Tamarix): A Comparison of Single-scene and Time-series Analyses of Remotely Sensed Data," *Remote Sensing*, vol. 1, no. 3, pp. 519–533, Aug. 2009.

[12] S. Sriharan, J. Everitt, C. Yang, and R. Fletcher, "Mapping Riparian and Wetland Weeds with High Resolution Satellite Imagery," in *Proceedings IEEE International Geoscience and Remote Sensing Symposium (IGARSS)*, 2008.

[13] C. Walter and D. D. Tullos, "Downstream Channel Changes after a Small Dam Removal: Using Aerial Photos and Measurement Error for Context; Calapooia River, Oregon," *River Research and Applications*, vol. 26, no. 10, pp. 1220–1245, Dec. 2010.

[14] C. E. Torgersen, D. M. Price, H. W. Li, and B. A. McIntosh, "Multiscale Thermal Refugia and Stream Habitat Associations of Chinook Salmon in Northeastern Oregon," *Ecological Applications*, vol. 9, no. 1, pp. 301–319, Feb. 1999.

[15] J. Kay, R. Handcock, A. Gillespie, C. Konrad, S. Burges, N. Naveh, and D. Booth, "Stream-temperature Estimation from Thermal Infrared Images," in *IEEE 2001 International Geoscience and Remote Sensing Symposium*, vol. 1. IEEE, 2001, pp. 112–114.

[16] P. Coppin and M. Bauer, "Digital Change Detection in Forest Ecosystems with Remote Sensing Imagery," *Remote Sensing Reviews*, vol. 13, no. 3-4, 1996.

[17] M. Lefsky, D. Harding, and W. Cohen, "Surface Lidar Remote Sensing of Basal Area and Biomass in Deciduous Forests of Eastern Maryland, USA," *Remote Sensing of Environment*, vol. 67, no. 1, pp. 83–98, 1999.

[18] C. Wessman, J. Aber, D. Peterson, and J. Melillo, "Remote Sensing of Canopy Chemistry and Nitrogen Cycling in Temperate Forest Ecosystems," *Nature*, vol. 335, no. 6186, 1988.

[19] S. G. Bajwa and E. D. Vories, "Spectral Response of Cotton Canopy to Water Stress," in *Proceedings of the American Society of Agricultural and Biological Engineers Annual Meeting*, July 2006.

[20] R. H. Gray and J. M. Haynes, "Spawning Migration of Adult Chinook Salmon (Oncorhynchus tshawytscha) Carrying External and Internal Radio Transmitters," *Journal of the Fisheries Research Board of Canada*, vol. 36, no. 9, pp. 1060–1064, Sept. 1979.

[21] A. Rango, A. Laliberte, J. E. Herrick, C. Winters, K. Havstad, C. Steele, and D. Browning, "Unmanned Aerial Vehicle-based Remote Sensing for Rangeland Assessment, Monitoring, and Management," *Journal of Applied Remote Sensing*, vol. 3, no. 1, p. 033542, Jan. 2009.

[22] J. Berni, P. J. Zarco-Tejada, L. Suarez, and E. Fereres, "Thermal and Narrowband Multispectral Remote Sensing for Vegetation Monitoring from an Unmanned Aerial Vehicle," *IEEE Transactions on Geoscience and Remote Sensing*, vol. 47, no. 3, pp. 722–738, Mar. 2009.

[23] L. Wallace, A. Lucieer, C. Watson, and D. Turner, "Development of a UAV-LiDAR System with Application to Forest Inventory," *Remote Sensing*, vol. 4, no. 6, pp. 1519–1543, May 2012.

[24] A. M. Jensen, T. Hardy, M. McKee, and Y. Q. Chen, "Using a Multispectral Autonomous Unmanned Aerial Remote Sensing Platform (AggieAir) for Riparian and Wetland Applications," in *Proceedings IEEE International Geoscience and Remote Sensing Symposium (IGARSS)*, Aug. 2011.

[25] A. Laliberte, C. Winters, and A. Rango, "UAS Remote Sensing Missions for Rangeland Applications," *Geocarto International*, vol. 26, no. 2, pp. 141–156, Dec. 2011.

[26] A. M. Jensen, M. McKee, and Y. Chen, "Calibrating Thermal Imagery from an Unmanned Aerial System - AggieAir," in *Proceedings IEEE International Geoscience and Remote Sensing Symposium (IGARSS)*, 2013.

[27] A. M. Jensen, D. K. Geller, and Y. Chen, "Monte Carlo Simulation Analysis of Tagged Fish Radio Tracking Performance by Swarming Unmanned Aerial Vehicles in Fractional Order Potential Fields," *Journal of Intelligent & Robotic Systems*, vol. 74, no. 1-2, pp. 287–307, Oct. 2014.

[28] "Academy of Model Aeronautics Membership Manual," Academy of Model Aeronautics, 2014. [Online]. Available: https://www.modelaircraft.org/files/memanual.pdf

[29] "Unmanned Aircraft Systems (UAS) Operational Approval (8900.227)," Federal Aviation Administration, 2013. [Online]. Available: https://www.faa.gov/regulations_policies/orders_notices/index.cfm/go/document.information/documentID/1021650

[30] A. S. Laliberte, M. A. Goforth, C. M. Steele, and A. Rango, "Multispectral Remote Sensing from Unmanned Aircraft: Image Processing Workflows and Applications for Rangeland Environments," *Remote Sensing*, vol. 3, no. 11, pp. 2529–2551, Nov. 2011.

[31] J. Kelcey and A. Lucieer, "Sensor Correction of a 6-Band Multispectral Imaging Sensor for UAV Remote Sensing," *Remote Sensing*, vol. 4, no. 5, pp. 1462–1493, May 2012.

[32] J. Berni, P. J. Zarco-Tejada, L. Surez, V. González-Dugo, and E. Fereres, "Remote Sensing of Vegetation from UAV Platforms using Lightweight Multispectral and Thermal Imaging Sensors," in *The International Archives of the Photogrammetry, Remote Sensing and Spatial Information Sciences*, 2008.

[33] A. Simpson, T. Stombaugh, L. Wells, and J. Jacob, "Imaging Techniques and Applications for UAV's in Agriculture," in *Proceedings of the American Society of Agricultural and Biological Engineers Annual Meeting*, July 2003.

[34] C. Coopmans, B. Stark, and C. M. Coffin, "A Payload Verification and Management Framework for Small UAV-based Personal Remote Sensing Systems," in *Proceedings of the 5th International Symposium on Resilient Control Systems*. IEEE, Aug. 2012, pp. 184–189.

[35] G. L. Ritchie, D. G. Sullivan, C. D. Perry, J. E. Hook, and C. W. Bednarz, "Preparation of a Low-Cost Digital Camera System for Remote Sensing," *Applied Engineering in Agriculture*, vol. 24, no. 6, pp. 885–894, 2008.

[36] T. Miura and A. Huete, "Performance of Three Reflectance Calibration Methods for Airborne Hyperspectral Spectrometer Data," *Sensors*, vol. 9, no. 2, pp. 794–813, 2009.

[37] E. R. Hunt, M. Cavigelli, C. S. T. Daughtry, J. E. Mcmurtrey, and C. L. Walthall, "Evaluation of Digital Photography from Model Aircraft for Remote Sensing of Crop Biomass and Nitrogen Status," *Precision Agriculture*, vol. 6, no. 4, pp. 359–378, Aug. 2005.

[38] S. Clemens, "Procedures for Correcting Digital Camera Imagery Acquired by the AggieAir Remote Sensing Platform," Master's thesis, Utah State University, 2012.

[39] J. Kannala, J. Heikkilä, and S. S. Brandt, "Geometric Camera Calibration," in *Wiley Encyclopedia of Computer Science and Engineering*. Hoboken, NJ: John Wiley & Sons, Inc., Mar. 2007, pp. 1–11.

[40] J. Bouguet, "Camera Calibration Toolbox for Matlab," 2012. [Online]. Available: http://www.vision.caltech.edu/bouguetj/calib_doc/

[41] J. Heikkila and O. Silven, "A Four-Step Camera Calibration Procedure with Implicit Image Correction," in *Proceedings of IEEE Computer Society Conference on Computer Vision and Pattern Recognition*. IEEE Computer Society, 1997, pp. 1106–1112.

[42] "MosaicMill EnsoMOSAIC," 2012. [Online]. Available: http://www.ensomosaic.com

[43] A. Jensen, "gRAID: A Geospatial Real-Time Aerial Image Display for a Low-Cost Autonomous Multispectral Remote Sensing Platform (AggieAir)," Master's thesis, Utah State University, 2009.

[44] W. Ji and P. Rhodes, "Spectral Color Characterization of Digital Cameras: A Review," in *Proceedings of Society of Photographic Instrumentation Engineers Vol*, 2012.

[45] C. E. Torgersen, R. N. Faux, B. A. McIntosh, N. J. Poage, and D. J. Norton, "Airborne Thermal Remote Sensing for Water Temperature Assessment in Rivers and Streams," *Remote Sensing of Environment*, vol. 76, no. 3, pp. 386–398, 2001.

[46] M. A. Gallo, D. S. Willits, R. A. Lubke, and E. C. Thiede, "Low-cost Uncooled IR Sensor for Battlefield Surveillance," in *Proceedings Society of Photographic Instrumentation Engineers 2020, Infrared Technology XIX*, vol. 2020, 1993, pp. 351–362.

[47] T. W. Parker, C. A. Marshall, M. Kohin, and R. Murphy, "Uncooled Infrared Sensors for Surveillance and Law Enforcement Applications," in *Proceedings Society of Photographic Instrumentation Engineers 2935, Surveillance and Assessment Technologies for Law Enforcement*, vol. 2935, 1997, pp. 182–187.

[48] "Infrared Cameras Incorporated," 2012. [Online]. Available: http://www.infraredcamerasinc.com

[49] A. Jensen, B. Neilson, M. McKee, and Y. Chen, "Thermal Remote Sensing With an Autonomous Unmanned Aerial Remote Sensing Platform for Surface Stream Temperatures," in *Proceedings IEEE International Geoscience and Remote Sensing Symposium (IGARSS)*, 2012, pp. 5049–5052.

[50] A. J. Prata, "Land Surface Temperatures Derived from the Advanced Very High Resolution Radiometer and the Along-Track Scanning Radiometer: 2. Experimental Results and Validation of AVHRR Algorithms," *Journal of Geophysical Research*, vol. 99, no. D6, 1994.

[51] G. Wukelic, D. Gibbons, L. Martucci, and H. Foote, "Radiometric Calibration of Landsat Thematic Mapper Thermal Band," *Remote Sensing of Environment*, vol. 28, pp. 339–347, 1989.

[52] R. R. Irish, "Landsat 7 Science Data Users Handbook," National Aeronautics and Space Administration, 2000.

[53] "Landsat Data Continuity Mission," 2013. [Online]. Available: http://ldcm.gsfc.nasa.gov/index.html

[54] R. W. Hillyard and E. R. Keeley, "Distribution and Spawning Migrations of Fluvial Bonneville Cutthroat Trout in the Bear River, Idaho," Idaho State University, Feb., 2009.

[55] M. Leonardo, A. Jensen, C. Coopmans, M. McKee, and Y. Chen, "A Miniature Wildlife Tracking UAV Payload System using Acoustic Biotelemetry," in *Proceedings of the ASME International Design Engineering Technical Conferences & Computers and Information in Engineering Conference*, Portland, Aug. 2013.

[56] E. W. Frew, C. Dixon, B. Argrow, and T. Brown, "Radio Source Localization by a Cooperating UAV Team," in *Infotech@ Aerospace*, 2005.

[57] F. Korner, R. Speck, A. H. Goktogan, and S. Sukkarieh, "Autonomous Airborne Wildlife Tracking Using Radio Signal Strength," in *Proceedings of the IEEE/RSJ International Conference on Intelligent Robots and Systems*. IEEE, Oct. 2010, pp. 107–112.

[58] S. Ge and Y. Cui, "Dynamic Motion Planning for Mobile Robots Using Potential Field Method," *Autonomous Robots*, vol. 13, no. 3, pp. 207–222, Nov. 2002.

[59] T. Paul, T. R. Krogstad, and J. T. Gravdahl, "Modelling of UAV Formation Flight Using 3D Potential Field," *Simulation Modelling Practice and Theory*, vol. 16, no. 9, pp. 1453–1462, Oct. 2008.

[60] O. Khatib, "Real-time Obstacle Avoidance for Manipulators and Mobile Robots," in *Proceedings of the IEEE International Conference on Robotics and Automation*, vol. 2. Institute of Electrical and Electronics Engineers, 1985, pp. 500–505.

[61] Y. Chen, Z. Wang, and K. Moore, "Optimal Spraying Control of a Diffusion Process Using Mobile Actuator Networks with Fractional Potential Field Based Dynamic Obstacle Avoidance," in *Proceedings of the IEEE International Conference on Networking, Sensing and Control*. IEEE, 2006, pp. 107–112.

[62] K. Miller, "The Weyl Fractional Calculus," in *Fractional Calculus and Its Applications*, ser. Lecture Notes in Mathematics, B. Ross, Ed. Berlin, Heidelberg: Springer, 1975, vol. 457, pp. 80–89.

[63] S. Galatowitsch, N. Anderson, and P. Ascher, "Invasiveness in Wetland Plants in Temperate North America," *Wetlands*, vol. 19, no. 4, pp. 733–755, 1999.

[64] M. Marks, B. Lapin, and J. Randall, "Phragmites Australis (P. communis): Threats, Management and Monitoring." *Natural Areas Journal*, 1994.

[65] L. Meyerson, R. Chambers, and K. Vogt, "The Effects of Phragmites Removal on Nutrient Pools in a Freshwater Tidal Marsh Ecosystem," *Biological Invasions*, vol. 1, no. 2-3, pp. 129–136, 1999.

[66] L. Meyerson, K. Saltonstall, and L. Windham, "A Comparison of Phragmites Australis in Freshwater and Brackish Marsh Environments in North America," *Wetlands Ecology and Management*, vol. 8, no. 2-3, pp. 89–103, 2000.

[67] L. Windham and J. Ehrenfeld, "Net Impact of a Plant Invasion on Nitrogen-cycling Processes within a Brackish Tidal Marsh," *Ecological Applications*, vol. 13, pp. 883–896, 2003.

[68] B. Zaman, M. McKee, and A. Jensen, "Use of High-Resolution Multispectral Imagery Acquired with an Autonomous Unmanned Aerial Vehicle to Quantify the Spread of an Invasive Wetland Species," in *Proceedings IEEE International Geoscience and Remote Sensing Symposium (IGARSS)*, Aug. 2011.

[69] M. Moran, Y. Inoue, and E. Barnes, "Opportunities and Limitations for Image-based Remote Sensing in Precision Crop Management," *Remote Sensing of Environment*, vol. 61, no. 3, pp. 319–346, 1997.

[70] B. Brisco, R. Brown, and T. Hirose, "Precision Agriculture and the Role of Remote Sensing: A Review," *Can J Remote Sensing*, vol. 24, no. 3, pp. 315–327, 1998.

[71] R. Pearson, J. Grace, and G. May, "Real-time Airborne Agricultural Monitoring," *Remote Sensing of Environment*, vol. 49, no. 3, pp. 304–310, 1994.

[72] D. Lamb and R. Brown, "Precision Agriculture: Remote-Sensing and Mapping of Weeds in Crops," *Journal of Agricultural Engineering Research*, vol. 78, no. 2, pp. 117–125, 2001.

[73] M. Al-Arab, A. M. Ticlavilca, A. F. Torres-Rua, I. Maslova, and M. McKee, "Use of High-Resolution Multispectral Imagery to Estimate Chrorophyll and Plant Nitrogen in Oats (Avena sativa)," Abstract B43C-0493 presented at 2013 Fall Meeting, American Geophysical Union (AGU), San Francisco, CA, 2013.

[74] M. Al-Arab, A. Torres-Rua, A. Ticlavilca, A. Jensen, and M. McKee, "Use of High-Resolution Multispectral Imagery from an Unmanned Aerial Vehicle in Precision Agriculture," in *Proceedings IEEE International Geoscience and Remote Sensing Symposium (IGARSS)*, 2013.

[75] A. F. Torres-Rua, W. R. Walker, and M. McKee, "The Lower Sevier River Basin Crop Monitor and Forecast Decision Support System: Exploiting Landsat Imagery to Provide Continuous Information to Farmers and Water Managers," Abstract IN14A-07 presented at 2013 Fall Meeting, American Geophysical Union (AGU), San Francisco, CA, 2013.

[76] G. W. Brown, "Predicting Temperatures of Small Streams," *Water Resources Research*, vol. 5, no. 1, p. 68, 1969.

[77] M. C. Westhoff, H. H. G. Savenije, W. M. J. . Luxemburg, G. S. Stelling, N. C. Van De Giesen, J. S. Selker, L. Pfister, and S. Uhlenbrook, "A Distributed Stream Temperature Model using High Resolution Temperature Observations," *Hydrology and Earth System Sciences*, vol. 11, no. 4, pp. 1469–1480, July 2007.

[78] B. H. Atwell, R. B. MacDonald, and L. A. Bartolucci, "Thermal Mapping of Streams from Airborne Radiometric Scanning," *Journal of the American Water Resources Association*, vol. 7, no. 2, pp. 228–243, Apr. 1971.

[79] D. J. Norton, M. A. Flood, B. McIntosh, N. J. Poage, P. J. LaPlaca, J. P. Craig, S. R. Karalus, J. R. Sedell, C. Torgersen, Y. D. Chen, S. C. McCutheeon, S. C. Duong, H. Puffenberger, J. Moeller, V. Kelley, E. Porter, and L. Shoemaker, "Modeling, Monitoring, and Restoring Water Quality and Habitat in the Pacific Northwestern Watersheds," U.S. Environmental Protection Agency, Washington, DC, 1996.

[80] N. C. Cristea and S. J. Burges, "Use of Thermal Infrared Imagery to Complement Monitoring and Modeling of Spatial Stream Temperatures," *Journal of Hydrologic Engineering*, vol. 14, no. 10, p. 1080, Feb. 2009.

[81] C. Coopmans, B. Stark, A. Jensen, Y. Chen, and M. McKee, "Cyber-Physical Systems Enabled By Small Unmanned Aerial Vehicles," in *Handbook of Unmanned Aerial Vehicles*, K. P. Valavanis and G. J. Vachtsevanos, Eds. New York, NY: Springer, 2014.

[82] H. Chao and Y. Chen, *Remote Sensing and Actuation Using Unmanned Vehicles*. Hoboken, NJ: Wiley-IEEE Press, 2012.

Appendix

Certificate of Authorization

This appendix contains an FAA COA given to Utah State University using AggieAir to fly on the North slope of Alaska near a remote field station called Toolik. The flight operations for this COA and part of the pre-flight checklist for airworthiness are also included.

DEPARTMENT OF TRANSPORTATION
FEDERAL AVIATION ADMINISTRATION

CERTIFICATE OF WAIVER OR AUTHORIZATION

ISSUED TO

Utah Water Research Laboratory - Utah State University

8200 Old Main Hill
Logan, UT 84322

This certificate is issued for the operations specifically described hereinafter. No person shall conduct any operation pursuant to the authority of this certificate except in accordance with the standard and special provisions contained in this certificate, and such other requirements of the Federal Aviation Regulations not specifically waived by this certificate.

OPERATIONS AUTHORIZED

Operation of the AggieAir Unmanned Aircraft System (UAS) in Class G airspace at or below 1,000 feet Above Ground Level (AGL) in the vicinity of the Kuparuk River basin (as depicted in Attachment 1) under the jurisdiction of Anchorage Air Route Traffic Control Center (ARTCC).

LIST OF WAIVED REGULATIONS BY SECTION AND TITLE

N/A

STANDARD PROVISIONS

1. A copy of the application made for this certificate shall be attached and become a part hereof.
2. This certificate shall be presented for inspection upon the request of any authorized representative of the Federal Aviation Administration, or of any State or municipal official charged with the duty of enforcing local laws or regulations.
3. The holder of this certificate shall be responsible for the strict observance of the terms and provisions contained herein.
4. This certificate is nontransferable.

Note-This certificate constitutes a waiver of those Federal rules or regulations specifically referred to above. It does not constitute a waiver of any State law or local ordinance.

SPECIAL PROVISIONS

Special Provisions are set forth and attached.

This certificate 2013-WSA-63 is effective from June 25, 2013 to June 24, 2015, and is subject to cancellation at any time upon notice by the Administrator or his/her authorized representative.

BY DIRECTION OF THE ADMINISTRATOR

FAA Headquarters, AJV-115
(Region)

Douglas Gould
(Signature)

June 21, 2013
(Date)

Air Traffic Manager, UAS Tactical Operations Section
(Title)

FAA Form 7711-1 (7-74)

COA Number: 2013-WSA-63

Issued To: Utah Water Research Laboratory - Utah State University, referred herein as the "proponent"

Address: 8200 Old Main Hill
Logan, UT 84322

Activity: Operation of the AggieAir Unmanned Aircraft System (UAS) in Class G airspace at or below 1,000 feet Above Ground Level (AGL) in the vicinity of the Kuparuk River basin (as depicted in Attachment 1) under the jurisdiction of Anchorage Air Route Traffic Control Center (ARTCC).

Purpose: To prescribe UAS operating requirements in the National Airspace System (NAS) for the purpose of quantifying the influences of lateral inflows on river water temperatures in the Kuparuk River basin.

Dates of Use: This COA is valid from June 25, 2013 to June 24, 2015. Should a renewal become necessary, the proponent shall advise the Federal Aviation Administration (FAA), in writing, no later than 45 business days prior to the requested effective date.

Public Aircraft

1. A public aircraft operation is determined by statute, 49 USC §40102(a)(41) and §40125.
2. All public aircraft flights conducted under a COA must comply with the terms of the statute.
3. All flights must be conducted per the declarations submitted on COA on-line.

STANDARD PROVISIONS

A. **General.**

The review of this activity is based upon current understanding of UAS operations and their impact in the NAS. This COA will not be considered a precedent for future operations. (As changes in or understanding of the UAS industry occur, limitations and conditions for operations will be adjusted.)

All personnel connected with the UAS operation must read and comply with the contents of this authorization and its provisions.

A copy of the COA including the special limitations must be immediately available to all operational personnel at each operating location whenever UAS operations are being conducted.

This authorization may be canceled at any time by the Administrator, the person authorized to grant the authorization, or the representative designated to monitor a specific operation. As a general rule, this authorization may be canceled when it is no longer required, there is an abuse of its provisions, or when unforeseen safety factors develop. Failure to comply with the authorization is cause for cancellation. The proponent will receive written notice of cancellation.

During the time this COA is approved and active, a site safety evaluation/visit may be accomplished to ensure COA compliance, assess any adverse impact on ATC or airspace, and ensure this COA is not burdensome or ineffective. Deviations, accidents/incidents/mishaps, complaints, etc will prompt a COA review or site visit to address the issue. Refusal to allow a site safety evaluation/visit may result in cancellation of the COA. Note: This section does not pertain to agencies that have other existing agreements in place with the FAA.

B. **Airworthiness Certification.**

The unmanned aircraft must be shown to be airworthy to conduct flight operations in the NAS. Utah Water Research Laboratory - Utah State University has made its own determination that the AggieAir unmanned aircraft is airworthy. The AggieAir must be operated in strict compliance with all provisions and conditions contained in the Airworthiness Safety Release, including all documents and provisions referenced in the COA application.

1. A configuration control program must be in place for hardware and/or software changes made to the UAS to ensure continued airworthiness. If a new or revised Airworthiness Release is generated as a result of changes in the hardware or software affecting the operating characteristics of the UAS, notify the UAS Integration Office of the changes as soon as practical.

a. Software and hardware changes should be documented as part of the normal maintenance procedures. Software changes to the aircraft and control station as well as hardware system changes are classified as major changes unless the agency has a formal process, accepted by the FAA. These changes should be provided to the UAS Integration office in summary form at the time of incorporation.

b. Major modifications or changes, performed under the COA, or other authorizations that could potentially affect the safe operation of the system must be documented and provided to the FAA in the form of a new AWR, unless the agency has a formal process, accepted by the FAA.

c. All previously flight proven systems to include payloads, may be installed or removed as required, and that activity recorded in the unmanned aircraft and ground control stations logbooks by persons authorized to conduct UAS maintenance Describe any payload equipment configurations in the UAS logbook that will result in a weight and balance change, electrical loads, and or flight dynamics, unless the agency has a formal process, accepted by the FAA.

d. For unmanned aircraft system discrepancies, a record entry should be made by an appropriately rated person to document the finding in the logbook. No flights may be conducted following major changes, modifications or new installations unless the party responsible for certifying airworthiness has determined the system is safe to operate in the NAS and a new AWR is generated, unless the agency has a formal process, accepted by the FAA. The successful completion of these tests must be recorded in the appropriate logbook, unless the agency has a formal process, accepted by the FAA.

2. The AggieAir must be operated in strict compliance with all provisions and conditions contained within the spectrum analysis assigned and authorized for use within the defined operations area.

3. All items contained in the application for equipment frequency allocation must be adhered to, including the assigned frequencies and antenna equipment characteristics. A ground operational check to verify the control station can communicate with the aircraft (frequency integration check) must be conducted prior to the launch of the unmanned aircraft to ensure any electromagnetic interference does not adversely affect control of the aircraft.

4. The use of a Traffic Collision Avoidance System (TCAS) in any mode while operating an unmanned aircraft is prohibited.

C. **Operations.**

1. Unless otherwise authorized as a special provision, a maximum of one unmanned aircraft will be controlled:

a. In any defined operating area,

b. From a single control station, and

c. By one pilot at a time.

2. A Pilot-in-Command (PIC) is the person who has final authority and responsibility for the operation and safety of flight, has been designated as PIC before or during the flight, and holds the appropriate category, class, and type rating, if appropriate, for the conduct of the flight. The responsibility and authority of the PIC as described by 14 CFR 91.3, Responsibility and Authority of the Pilot-in-Command, apply to the unmanned aircraft PIC. The PIC position may rotate duties as necessary with equally qualified pilots. The individual designated as PIC may change during flight. **Note:** The PIC can only be the PIC for one aircraft at a time. For Optionally Piloted Aircraft (OPA), PIC must meet UAS guidance requirements for training, pilot licensing, and medical requirements when operating OPA as a UAS.

3. The PIC must conduct a pre-takeoff briefing as applicable prior to each launch. The briefing should include but is not limited to the:

   a. Contents of the COA,

   b. Altitudes to be flown,

   c. Mission overview including handoff procedures,

   d. Frequencies to be used,

   e. Flight time, including reserve fuel requirements,

   f. Contingency procedures to include lost link, divert, and flight termination, and

   g. Hazards unique to the flight being flown.

Note: Flight Crew Member (UAS). In addition to the flight crew members identified in 14 CFR Part 1, Definitions and Abbreviations, an Unmanned Aircraft System flight crew members include pilots, sensor/payload operators, and visual observers and may include other persons as appropriate or required to ensure safe operation of the aircraft.

4. All operations will be conducted in compliance with Title 14 CFR Part 91. Special attention should be given to:

   a. § 91.3 Responsibility and authority of the pilot in command

   b. § 91.13 Careless or reckless operation

   c. § 91.17 Alcohol or drugs

   d. § 91.103 Preflight Actions

   e. § 91.111 Operating near other aircraft.

   f. § 91.113 Right-of-way rules: Except water operations

   g. § 91.115 Right-of-way rules: Water operations

h. § 91.119 Minimum safe altitudes: General

i. § 91.123 Compliance with ATC clearances and instructions.

j. § 91.133 Restricted and prohibited areas

k. § 91.137 Temporary flight restrictions in the vicinity of disaster/hazard areas

l. § 91.145 Management of aircraft operations in the vicinity of aerial demonstrations and major sporting events

m. § 91.151 Fuel requirements for flight in VFR conditions

n. § 91.155 Basic VFR weather minimums

o. § 91.159 VFR cruising altitude or flight level

p. § 91.209 Aircraft Lights

q. § 91.213 Inoperative instruments and equipment

r. § 91.215 ATC transponder and altitude reporting equipment and use

s. Appendix D to Part 91—Airports/Locations: Special Operating Restrictions

5. Unless otherwise authorized as a special provision, all operations must be conducted in visual meteorological conditions (VMC) during daylight hours in compliance with Title 14 of the Code of Federal Regulations (CFR) Part 91 §91.155 and the following:

6. Special Visual Flight Rules (VFR) operations are not authorized.

   a. VFR cloud clearances specified in 14 CFR Part 91 §91.155, must be maintained, except in Class G airspace where Class E airspace visibility requirements must be applied, but not less than 3 statute miles (SM) flight visibility and 1000' ceiling.

   b. Flights conducted under Instrument Flight Rules (IFR) in Class A airspace shall remain clear of clouds. NOTE: Deviations from IFR clearance necessary to comply with this provision must have prior ATC approval.

   c. Chase aircraft must maintain 5 NM flight visibility.

7. Night operations are prohibited unless otherwise authorized as a special provision.

8. Operations (including lost link procedures) must not be conducted over populated areas, heavily trafficked roads, or an open-air assembly of people.

D. **Air Traffic Control (ATC) Communications.**

1. The pilot and/or PIC will maintain direct, two-way communication with ATC and have the ability to maneuver the unmanned aircraft in response to ATC instructions, unless addressed in the Special Provision Section.

a. When required, ATC will assign a radio frequency for air traffic control during flight. The use of land-line and/or cellular telephones is prohibited as the primary means for in-flight communication with ATC.

2. The PIC must not accept an ATC clearance requiring the use of visual separation, sequencing, or visual approach.

3. When necessary, transit of airways and routes must be conducted as expeditiously as possible. The unmanned aircraft must not loiter on Victor airways, jet routes, Q and T routes, IR routes, or VR routes.

4. For flights operating on an IFR clearance at or above 18,000 feet mean sea level (MSL), the PIC must ensure positional information in reference to established National Airspace System (NAS) fixes, NAVAIDs, and/or waypoints is provided to ATC. The use of latitude/longitude positions is not authorized, except oceanic flight operations.

5. If equipped, the unmanned aircraft must operate with:

   a. An operational mode 3/A transponder with altitude encoding, or mode S transponder (preferred) set to an ATC assigned squawk.

   b. Position/navigation and anti-collision lights on at all times during flight unless stipulated in the special provisions or the proponent has a specific exemption from 14 CFR Part 91.209.

6. Operations that use a Global Positioning System (GPS) for navigation must check Receiver Autonomous Integrity Monitoring (RAIM) notices prior to flight operations. Flight into a GPS test area or degraded RAIM is prohibited for those aircraft that use GPS as their sole means for navigation.

E. **Safety of Flight.**

1. The proponent or delegated representative is responsible for halting or canceling activity in the COA area if, at any time, the safety of persons or property on the ground or in the air is in jeopardy, or if there is a failure to comply with the terms or conditions of this authorization.

2. ATC must be immediately notified in the event of any emergency, loss and subsequent restoration of command link, loss of PIC or observer visual contact, or any other malfunction or occurrence that would impact safety or operations.

3. Sterile Cockpit Procedures:

   a. Critical phases of flight include all ground operations involving:

      (1) Taxi (movement of an aircraft under its own power on the surface of an airport).

      (2) Take-off and landing (launch or recovery).

(3) All other flight operations in which safety or mission accomplishment might be compromised by distractions.

b. No crewmember may perform any duties during a critical phase of flight not required for the safe operation of the aircraft.

c. No crewmember may engage in, nor may any PIC permit, any activity during a critical phase of flight which could:

(1) Distract any crewmember from the performance of his/her duties, or

(2) Interfere in any way with the proper conduct of those duties.

d. The pilot and/or the PIC must not engage in any activity not directly related to the operation of the aircraft. Activities include, but are not limited to, operating UAS sensors or other payload systems.

e. The use of cell phones or other electronic devices is restricted to communications pertinent to the operational control of the unmanned aircraft and any required communications with Air Traffic Control.

4. See-and-Avoid.

Unmanned aircraft have no on-board pilot to perform see-and-avoid responsibilities; therefore, when operating outside of active restricted and warning areas approved for aviation activities, provisions must be made to ensure an equivalent level of safety exists for unmanned operations. Adherence to 14 CFR Part 91 §91.111, §91.113 and §91.115, is required.

a. The proponent and/or delegated representatives are responsible at all times for collision avoidance with all aviation activities and the safety of persons or property on the surface with respect to the UAS.

b. UAS pilots will ensure there is a safe operating distance between aviation activities and unmanned aircraft at all times.

c. Any crew member responsible for performing see-and-avoid requirements for the UA must have and maintain instantaneous communication with the PIC.

d. UA operations will only be conducted within Reduced Vertical Separation Minimum (RVSM) altitudes, when appropriately equipped or having received a clearance under an FAA deviation. **NOTE:** UA operations should not plan on an en-route clearance in RVSM altitudes, without being RVSM equipped.

e. Visual observers must be used at all times except in Class A, airspace, active Restricted Areas, and Warning areas designated for aviation activities.

(1) Observers may either be ground-based or in a chase plane.

(2) If the chase aircraft is operating more than 100 feet above/below and/or more than ½ NM laterally of the unmanned aircraft, the chase aircraft PIC will advise the controlling ATC facility.

f. The PIC is responsible to ensure visual observers are:

(1) Able to see the aircraft and the surrounding airspace throughout the entire flight, and

(2) Able to provide the PIC with the UA's flight path, and proximity to all aviation activities and other hazards (e.g., terrain, weather, structures) sufficiently to exercise effective control of the UA to:

(a) Comply with CFR Parts 91.111, 91.113 and 91.115, and

(b) Prevent the UA from creating a collision hazard.

5. Observers must be able to communicate clearly to the pilot any instructions required to remain clear of conflicting traffic, using standard phraseology as listed in the Aeronautical Information Manual when practical.

6. A PIC may rotate duties as necessary to fulfill operational requirements; a PIC must be designated at all times.

7. Pilots flying chase aircraft must not concurrently perform observer or UA pilot duties.

8. Pilot and observers must not assume concurrent duties as both pilot and observer.

9. The required number of ground observers will be in place during flight operations.

10. The use of multiple successive observers (daisy chaining) is prohibited unless otherwise authorized as a special provision.

11. The dropping or spraying of aircraft stores, or carrying of hazardous materials (including ordnance) outside of active Restricted, Prohibited, or Warning Areas approved for aviation activities is prohibited unless specifically authorized as a special provision.

F. **Crewmember Requirements.**

1. All crewmembers associated with the operation of the unmanned aircraft, including chase operations, must be qualified or must be receiving formal training under the direct supervision of a qualified instructor, who has at all times, responsibility for the operation of the unmanned aircraft.

2. Pilots and observers must have an understanding of, and comply with, Title 14 Code of Federal Regulations, and/or agency directives and regulations, applicable to the airspace where the unmanned aircraft will operate.

3. Pilots, supplemental pilots, and observers must maintain a current second class (or higher) airman medical certificate that has been issued under 14 CFR Part 67, or an FAA accepted agency equivalent based on the application.

4. At a minimum, the use of alcohol and/or drugs in violation of 14 CFR Part 91 §91.17 applies to UA pilots and observers.

5. At a minimum, observers must receive training on rules and responsibilities described in 14 CFR Part 91 §91.111. §91.113 and §91.115, regarding cloud clearance, flight visibility, and the pilot controller glossary, including standard ATC phraseology and communication.

6. Recent Pilot Experience (Currency). The proponent must provide documentation, upon request, showing the pilot/supplemental pilot/PIC maintains an appropriate level of recent pilot experience in either the UAS being operated or in a certified simulator. At a minimum, he/she must conduct three takeoffs (launch) and three landings (recovery) in the specific UAS within the previous 90 days (excluding pilots who do not conduct launch/recovery during normal/emergency operations). If a supplemental pilot assumes the role of PIC, he/she must comply with PIC rating requirements.

7. A PIC and/or supplemental pilot have the ability to assume the duties of an internal or an external UAS pilot at any point during the flight.

8. A PIC may be augmented by supplemental pilots.

9. PIC Ratings.
   Rating requirements for the UAS PIC depend on the type of operation conducted. The requirement for the PIC to hold, at a minimum, a current FAA private pilot certificate or the FAA accepted agency equivalent, based on the application of 14 CFR Part 61, is predicated on various factors including the location of the planned operations, mission profile, size of the unmanned aircraft, and whether or not the operation is conducted within or beyond visual line-of-sight.

   a. The PIC must hold, at a minimum, a current FAA private pilot certificate or the FAA accepted agency equivalent, based on the application or 14 CFR Part 61.under all operations:

      (1) Approved for flight in Class A, B, C, D, E, and G (more than 400 feet above ground level (AGL)) airspace.

      (2) Conducted under IFR (FAA instrument rating required, or the FAA accepted agency equivalent, based on the application or 14 CFR Part 61.

      (3) Approved for night operations.

      (4) Conducted at or within 5 NM of a joint use or public airfields.

      (5) Requiring a chase aircraft.

(6) At any time the FAA has determined the need based on the UAS characteristics, mission profile, or other operational parameters.

b. Operations without a pilot certificate may be allowed when all of the following conditions are met:

(1) The PIC has successfully completed, at a minimum, FAA private pilot ground instruction and passed the written examination, or the FAA accepted agency equivalent, based on the application. Airman Test reports are valid for the 24-calendar month period preceding the month the exam was completed, at which time the instruction and written examination must be repeated.

(2) Operations are during daylight hours.

(3) The operation is conducted in a sparsely populated location.

(4) The operation is conducted from a privately owned airfield, military installation, or off-airport location.

(5) Operations are approved and conducted solely within visual line-of-sight in Class G airspace.

(6) Visual line-of-sight operations are conducted at an altitude of no more than 400 feet Above Ground Level (AGL) in class G airspace at all times.

c. The FAA may require specific aircraft category and class ratings in manned aircraft depending on the UAS seeking approval and the characteristics of its flight controls interface.

10. PIC Recent Flight Experience (Currency).

a. For those operations that require a certificated pilot or FAA accepted agency equivalent, based on the application, the PIC must have flight reviews 14 CFR Part 61.56, and if the pilot conducts takeoff, launch, landing or recovery the PIC must maintain recent pilot experience in manned aircraft per 14 CFR Part 61.57,; Recent Flight Experience: Pilot in Command.

b. For operations approved for night or IFR through special provisions, the PIC must maintain minimum recent pilot experience per 14 CFR Part 61.57, Recent Flight Experience: Pilot in Command, as applicable.

11. Supplemental pilots must have, at a minimum, successfully completed private pilot ground school and passed the written test or the FAA accepted agency equivalent, based on the application. The ground school written test results are valid for two years from the date of completion, at which time the instruction and written examination must be repeated. If a supplemental pilot assumes the role of PIC, he/she must comply with PIC rating, currency, medical, and training requirements listed in this document.

12. Ancillary personnel such as systems operators or mission specialists must be thoroughly familiar with and possess operational experience of the equipment being used. If the systems being used are for observation and detection of other aircraft for collision

avoidance purposes, personnel must be thoroughly trained on collision avoidance procedures and techniques and have direct communication with the UAS pilot, observer, and other crewmembers.

13. The Agency will ensure that Crew Resource Management (CRM) training is current for all crew members before flying operational or training missions. The CRM program must consist of initial training, as well as CRM recurrent training during every recurrent training cycle, not to exceed a 12 month interval between initial training and recurrent training or between subsequent recurrent training sessions.

G. **Notice to Airmen (NOTAM).**

1. A distant (D) NOTAM must be issued when unmanned aircraft operations are being conducted. This requirement may be accomplished:
   a. Through the proponent's local base operations or NOTAM issuing authority, or
   b. By contacting the NOTAM Flight Service Station at 1-877-4-US-NTMS (1-877-487-6867) not more than 72 hours in advance, but not less than 48 hours prior to the operation, unless otherwise authorized as a special provision. The issuing agency will require the:
      (1) Name and address of the pilot filing the NOTAM request
      (2) Location, altitude, or operating area
      (3) Time and nature of the activity.

2. For proponents filing their NOTAM with the Department of Defense: The requirement to file with an Automated Flight Service Station (AFSS) is in addition to any local procedures/requirements for filing through the Defense Internet NOTAM Service (DINS).

H. **Data Reporting.**

1. Documentation of all operations associated with UAS activities is required regardless of the airspace in which the UAS operates. This requirement includes COA operations within Special Use airspace. NOTE: Negative (zero flights) reports are required.
2. The proponent must submit the following information through UAS COA On-Line on a monthly basis:
   a. The number of flights conducted under this COA. (A flight during which any portion is conducted in the NAS must be counted only once, regardless of how many times it may enter and leave Special Use airspace between takeoff and landing)
   b. Aircraft operational hours per flight
   c. Ground control station operational hours in support of each flight, to include Launch and Recovery Element (LRE) operations

d. Pilot duty time per flight

e. Equipment malfunctions (hardware/software) affecting either the aircraft or ground control station

f. Deviations from ATC instructions and/or Letters of Agreement/Procedures

g. Operational/coordination issues

h. The number and duration of lost link events (control, vehicle performance and health monitoring, or communications) per aircraft per flight.

I. **Incident/Accident/Mishap Reporting.**

Immediately after an incident or accident, and before additional flight under this COA, the proponent must provide initial notification of the following to the FAA via the UAS COA On-Line forms (Incident/Accident).

1. All accidents/mishaps involving UAS operations where any of the following occurs:
   a. Fatal injury, where the operation of a UAS results in a death occurring within 30 days of the accident/mishap
   b. Serious injury, where the operation of a UAS results in a hospitalization of more than 48 hours, the fracture of any bone (except for simple fractures of fingers, toes, or nose), severe hemorrhage or tissue damage, internal injuries, or second or third-degree burns
   c. Total unmanned aircraft loss
   d. Substantial damage to the unmanned aircraft system where there is damage to the airframe, power plant, or onboard systems that must be repaired prior to further flight
   e. Damage to property, other than the unmanned aircraft.

2. Any incident/mishap that results in an unsafe/abnormal operation including but not limited to:
   a. A malfunction or failure of the unmanned aircraft's on-board flight control system (including navigation)
   b. A malfunction or failure of ground control station flight control hardware or software (other than loss of control link)
   c. A power plant failure or malfunction
   d. An in-flight fire
   e. An aircraft collision
   f. Any in-flight failure of the unmanned aircraft's electrical system requiring use of alternate or emergency power to complete the flight
   g. A deviation from any provision contained in the COA

h. A deviation from an ATC clearance and/or Letter(s) of Agreement/Procedures

i. A lost control link event resulting in

(1) Fly-away, or

(2) Execution of a pre-planned/unplanned lost link procedure.

3. Initial reports must contain the information identified in the COA On-Line Accident/Incident Report.

4. Follow-on reports describing the accident/incident/mishap(s) must be submitted by providing copies of proponent aviation accident/incident reports upon completion of safety investigations. Such reports must be limited to factual information only where privileged safety or law enforcement information is included in the final report.

5. Public-use agencies other than those which are part of the Department of Defense are advised that the above procedures are not a substitute for separate accident/incident reporting required by the National Transportation Safety Board under 49 CFR Part 830 §830.5.

6. This COA is issued with the provision that the FAA be permitted involvement in the proponent's incident/accident/mishap investigation as prescribed by FAA Order 8020.11, Aircraft Accident and Incident Notification, Investigation, and Reporting.

FLIGHT STANDARDS SPECIAL PROVISIONS

A. **Contingency Planning**

1. **Point Identification**. The proponent must submit contingency plans that address emergency recovery or flight termination of the unmanned aircraft (UA) in the event of unrecoverable system failure. These procedures will normally include Lost Link Points (LLP), Divert/Contingency Points (DCP) and Flight Termination Points (FTP) for each operation. LLPs and DCPs must be submitted in latitude/longitude (Lat/Long) format along with a graphic representation plotted on an aviation sectional chart (or similar format). FTPs or other accepted contingency planning measures must also be submitted in latitude/longitude (Lat/Long) format along with a graphic representation plotted on an aviation sectional chart, or other graphic representation acceptable to the FAA. The FAA accepts the LLPs, DCPs, FTPs, and other contingency planning measures, submitted by the proponent but does not approve them. When conditions preclude the use of FTPs, the proponent must submit other contingency planning options for consideration and approval. At least one LLP, DCP, and FTP (or an acceptable alternative contingency planning measure) is required for each operation. The proponent must furnish this data with the initial COA application. Any subsequent changes or modifications to this data must be provided to AJV-13 for review and consideration no later than 30 days prior to proposed flight operations.

2. **Risk Mitigation Plans**. For all operations, the proponent must develop detailed plans to mitigate the risk of collision with other aircraft and the risk posed to persons and property on the ground in the event the UAS encounters a lost link, needs to divert, or the flight needs to be terminated. The proponent must take into consideration all airspace constructs and minimize risk to other aircraft by avoiding published airways, military training routes, NAVAIDs, and congested areas. In the event of a contingency divert or flight termination, the use of a chase aircraft is preferred when the UAS is operated outside of Restricted or Warning Areas. If time permits, the proponent should make every attempt to utilize a chase aircraft to monitor the aircraft to a DCP or to the FTP. In the event of a contingency divert or flight termination, the proponent will operate in Class A airspace and Special Use airspace to the maximum extent possible to reduce the risk of collision with non-participating air traffic.

   a. **LLP Procedures**.
      (1) LLPs are defined as a point, or sequence of points where the aircraft will proceed and hold at a specified altitude, for a specified period of time, in the event the command and control link to the aircraft is lost. The aircraft will autonomously hold, or loiter, at the LLP until the communication link with the aircraft is restored or the specified time elapses. If the time period elapses, the aircraft may autoland, proceed to another LLP in an attempt to regain the communication link, or proceed to an FTP for flight termination. LLPs may be used as FTPs. In this case, the aircraft may loiter at the LLP/FTP until link is re-established or fuel exhaustion occurs.

(2) For areas where multiple or concurrent UAS operations are authorized in the same operational area, a segregation plan must be in place in the event of a simultaneous lost link scenario. The segregation plan may include altitude offsets and horizontal separation by using independent LLPs whenever possible.

b. **DCP Procedures**.

(1) A DCP is defined as an alternate landing/recovery site to be used in the event of an abnormal condition that requires a precautionary landing. Each DCP must incorporate the means of communication with ATC throughout the descent and landing (unless otherwise specified in the Special Provisions) as well as a plan for ground operations and securing/parking the aircraft on the ground. This includes the availability of ground control stations capable of launch/recovery, communication equipment, and an adequate power source to operate all required equipment.

(2) For local operations, the DCP specified will normally be the airport/facility used for launch and recovery; however, the proponent may specify additional DCPs as alternates.

(3) For transit and/or mission operations that are being conducted in Class A airspace or Class E airspace above flight level (FL)-600, DCPs will be identified during the flight to be no further than one hour of flight time at any given time, taking into consideration altitude, winds, fuel consumption, and other factors. If it is not possible to define DCPs along the entire flight plan route, the proponent must identify qualified FTPs along the entire route and be prepared to execute flight termination at one of the specified FTPs if a return to base (RTB) is not possible.

(4) It is preferred that specified DCPs are non-joint use military airfields, other government-owned airfields, or private-use airfields. However, the proponent may designate any suitable airfield for review and consideration.

c. **Flight Termination Procedures**.

(1) Flight termination is the intentional and deliberate process of performing controlled flight into terrain (CFIT). Flight termination must be executed in the event that all contingencies have been exhausted and further flight of the aircraft cannot be safely achieved or other potential hazards exist that require immediate discontinuation of flight. FTPs or alternative contingency planning measures must be located within power off glide distance of the aircraft during all phases of flight and must be submitted for review and acceptance. The proponent must ensure sufficient FTPs or other contingency plan measures are defined to accommodate flight termination at any given point along the route of flight. The location of these points is based on the assumption of an unrecoverable system failure and must take into consideration altitude, winds, and other factors.

(2) Unless otherwise authorized, FTPs must be located in sparsely populated areas. Except for on- or near-airport operations, FTPs will be located no closer than five nautical miles from any airport, heliport, airfield, NAVAID, airway, populated

area, major roadway, oil rig, power plant, or any other infrastructure. For offshore locations, the proponent must refer to appropriate United States Coast Guard (USCG) charts and other publications to avoid maritime obstructions, shipping lanes, and other hazards. Populated areas are defined as those areas depicted in yellow on a VFR sectional chart or as determined from other sources.

(a) It is preferred that flight termination occurs in Restricted or Warning Areas, government-owned land, or offshore locations that are restricted from routine civil use. However, the proponent may designate any suitable location for review and consideration.

(b) The proponent is required to survey all designated areas prior to their use as an FTP. All FTPs will be reviewed for suitability on a routine and periodic basis, not to exceed six months. The proponent assumes full risk and all liability associated with the selection and use of any designated FTP.

(c) It is desirable that the proponent receive prior permission from the land owner or using agency prior to the use of this area as an FTP. The proponent should clearly communicate the purpose and intent of the FTP.

(d) For each FTP, plans must incorporate the means of communication with ATC throughout the descent as well as a plan for retrieval/recovery of the aircraft.

(e) Contingency planning must take into consideration all airspace constructs and minimize risk to other aircraft by avoiding published airways, military training routes, NAVAIDs, and congested areas to the maximum extent possible.

(f) In the event of a contingency divert or flight termination, if time permits, the use of a chase aircraft is preferred when the UA is operated outside of Restricted or Warning Areas.

(g) In the event of a contingency divert or flight termination or other approved contingency measures, the proponent will operate in Class A airspace and Special Use airspace to the maximum extent possible to reduce the risk of collision with non-participating air traffic.

B. **Night Operation Limitations.**

UAS night operations are those operations that occur between the end of evening civil twilight and the beginning of morning civil twilight, as published in the American Air Almanac, converted to local time. (Note: this is equal to approximately 30 minutes after sunset until 30 minutes before sunrise).

1. Night operations are not authorized.

AIR TRAFFIC CONTROL SPECIAL PROVISIONS

A. **Coordination Requirements.**

1. At least 24 hours prior to operations the proponent shall notify Anchorage ARTCC and advise of time for commencement and termination of operations and provide NOTAM number and information.

2. Additionally, the proponent shall coordinate all UAS operations with the Toolik Field Station at (907) 455-2533 to deconflict helicopter operations in the vicinity.

B. **Communication Requirements.**

1. Proponent will make a blind broadcast on CTAF (122.9 MHz) indicating the launch and termination of UAS operations and monitor CTAF during flight operations.

2. ATC special provisions A & C will be used in lieu of maintaining direct two-way communications with ATC.

C. **Emergency/Contingency Procedures.**

Lost Link Procedures:

In the event of a lost link, the UAS pilot will immediately notify Toolik Field Station at (907) 455-2533, state pilot intentions, and comply with the following provisions:

a) Comply with those procedures outlined in Attachment 2.

b) If lost link occurs within a restricted or warning area, or the lost link procedure above takes the UA into the restricted or warning area – the aircraft will not exit the restricted or warning areas until the link is re-established.

c) The unmanned aircraft lost link mission will not transit or orbit over populated areas.

d) Lost link programmed procedures will avoid unexpected turn-around and/or altitude changes.

e) Lost link orbit points shall not coincide with the centerline of Victor airways.

Lost Communications:

Comply with those procedures outlined in Attachment 3.

AUTHORIZATION

This Certificate of Waiver or Authorization does not, in itself, waive any Title 14 Code of Federal Regulations, nor any state law or local ordinance. Should the proposed operation conflict with any state law or local ordinance, or require permission of local authorities or property owners, it is the responsibility of Utah Water Research Laboratory - Utah State University to resolve the matter. This COA does not authorize flight within Special Use airspace without approval from the using agency. Utah Water Research Laboratory - Utah State University is hereby authorized to operate the AggieAir Unmanned Aircraft System in the operations area depicted in the Activity section of this attachment.

Attachment 1

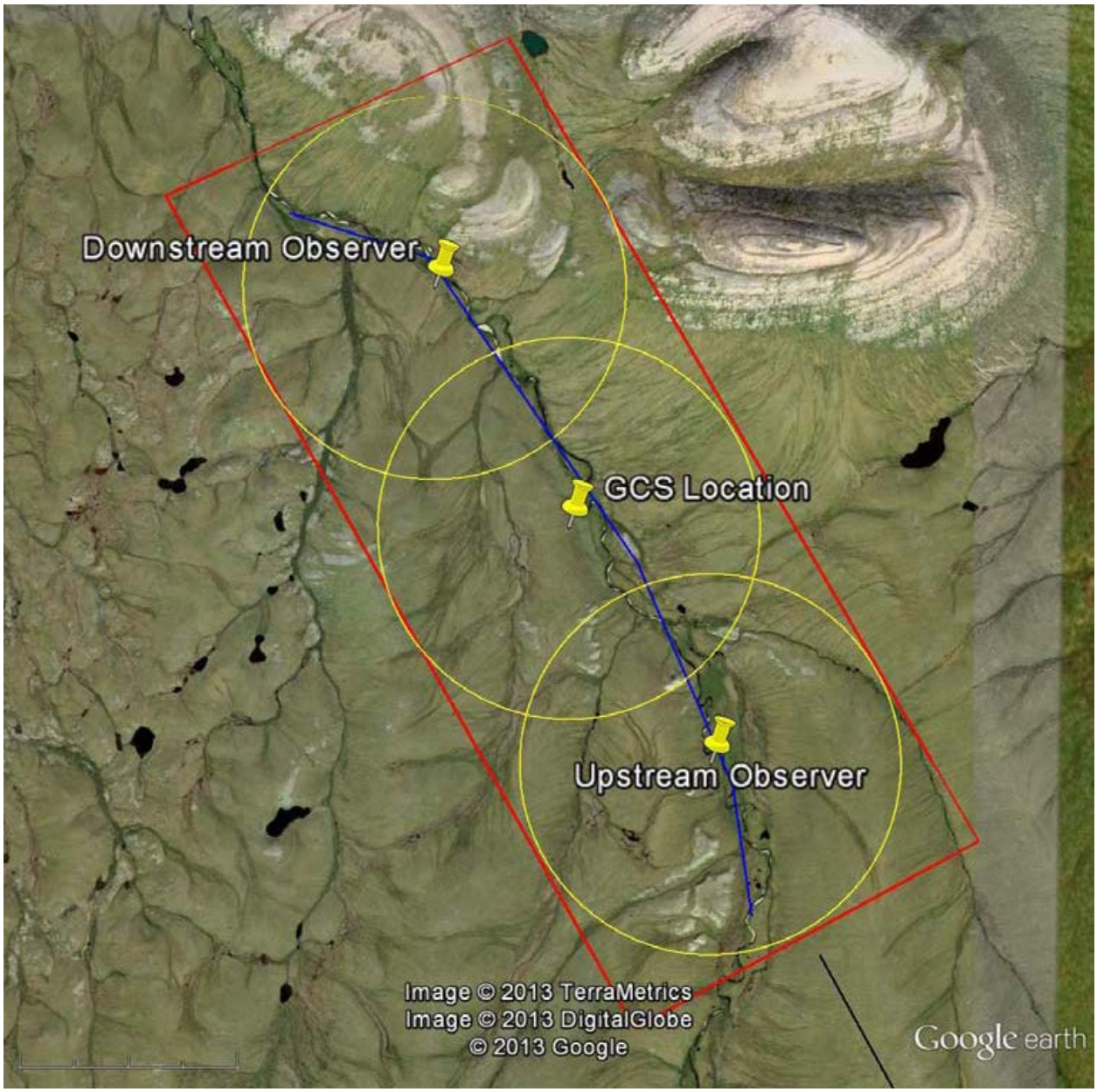

68-44-40.92N / 149-30-13.15W – Downstream Observer
68-43-35.95N / 149-28-32.53W – Ground Station / Takeoff / Landing Location
68-42-31.97N / 149-26-46.26W – Upstream Observer

Attachment 2

LOST LINK PROCEDURE(S)

Before takeoff, the UA is preprogrammed with a flight plan. This flight plan can be modified during flight if the UA is within communication range of the ground control station (GCS). However, the flight plan is built and simulated such that the UA can successfully fly the flight plan without any interaction from the GCS operator. Therefore the communication link between the UA and the GCS operator is not necessary for a successful flight. Nonetheless, for more safety, the UA is programmed to fly back to the GCS Location and circle above at 650’ AGL if communication is lost for more than 30 seconds. The GCS Location is located near the pilot (68°43'35.95"N 149°28'32.53"W). If communication is reestablished while flying towards the GCS Location, the pilot can change the flight plan to stay within communication range and resume the flight. The pilot could also land the UA using the landing area indicated by the flight operations. If communication is not reestablished, the pilot will take manual control and land the UA in the landing area when it comes into visual line-of-sight. If the pilot is not able to take manual control of the UA and communication has not been reestablished with the GCS, the UA will continue circling around GCS Location for 2 minutes or until the battery voltage falls below 10v. At this point, the motor will shut off, the autopilot will stop holding altitude, and the UA will safely descend to the ground in the same pattern around the GCS Location.

Attachment 3

LOST COMMUNICATIONS PROCEDURE(S)

To keep the UA within line-of-sight (LOS), one observer is placed at the GCS Location (68°43'35.95"N 149°28'32.53"W) and one observer is placed at each end of the flight area (a total of three observers during the flight). The downstream observer will be located at 68°44'40.92"N 149°30'13.15"W and the upstream observer will be located at 68°42'31.97"N 149°26'46.26"W. This always keeps the UA within a distance of 1 mile from an observer at all times. When an observer has the UA within LOS, this observer will be referred to as the active observer. The active observer will report to the pilot every 30 seconds using a commercial handheld two-way radio. This report will include whether the UA is within sight and the current status of the airspace around the UA. If another aircraft enters the airspace around the UA the observer will use the two-way radio to alert the pilot and suggest appropriate avoidance maneuvers. During the planned flight over the river, the three observers will exchange the responsibility of the active observer as the UA flies out of LOS of one observer and into LOS of another observer. With the two-way radios, the active observer will make sure that the next observer is ready and has the UA within LOS before exchanging the responsibilities of the active observer. If LOS is not established with the next observer before the UA flies outside LOS of the active observer, then the pilot will abort the planned flight over the river and send a command to the aircraft to return to the GCS Location and circle above it at 650’ AGL.

If the pilot does not get a report every 30 seconds from the active observer, then communication loss is assumed and the pilot will abort the planned flight over the river and send a command to the aircraft to return to the GCS Location and circle above it at 650’ AGL. At the GCS location, the observer and the pilot are collocated and will always have communication. With an active observer at the GCS, the pilot can either reestablish communication with the other observers and continue the flight or land the aircraft.

Flight Operations

Project Description

The aerial images taken from AggieAir will support a new National Science Foundation collaborative grant (ARC 1204220/1204216) between Utah State University (USU) and University of Alaska Fairbanks (UAF). Beth Neilson (PI from USU) and Doug Kane (Co-PI from UAF) will be working together to identify and quantify the influences of lateral inflows on river water temperatures in the Kuparuk River basin. The data provided by these flights for a small section of the river will result in fundamental information necessary to determine the frequency, distribution, and influences of these inflows. Similar information cannot be feasibly gathered using other measurement techniques.

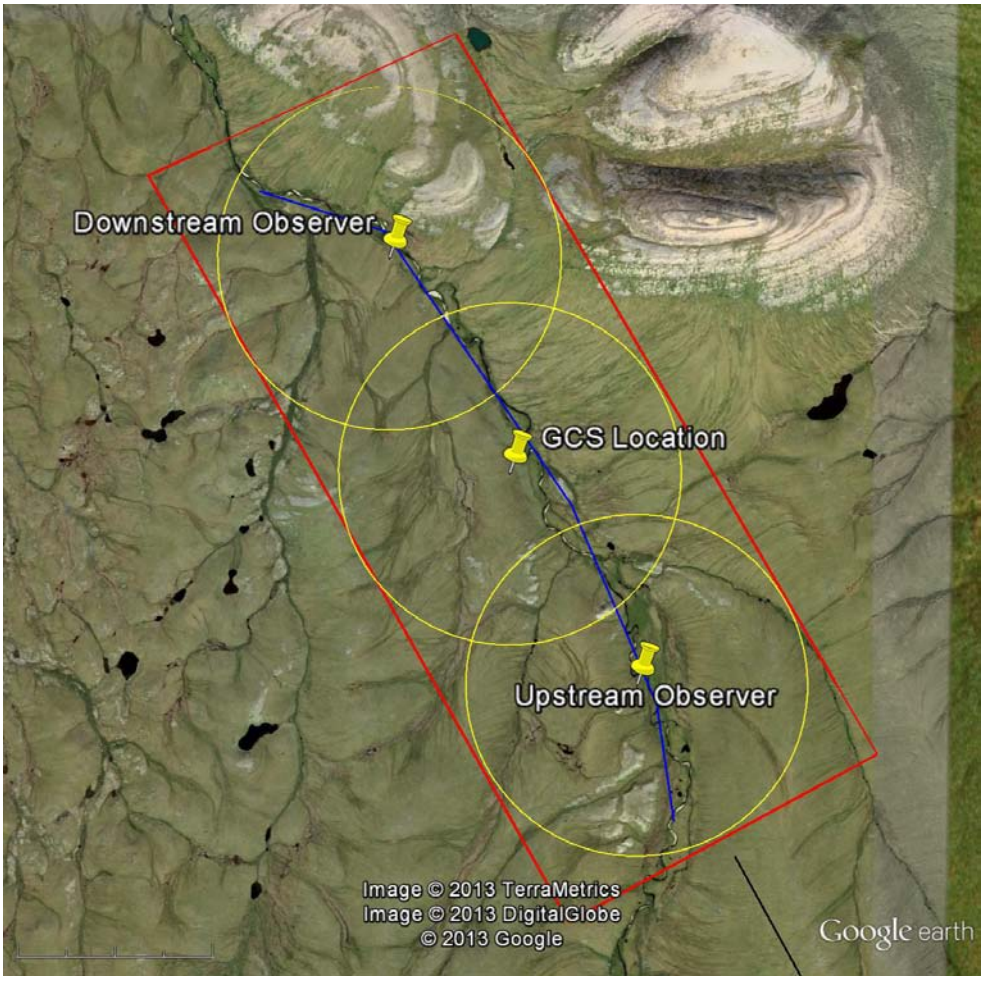

Figure 1: Flight Plan Map

Flight Area Description

Figure 1 shows the Kuparuk River 5-10 miles outside of the Toolik Field Station in the Arctic Circle Alaska. The land shown in the figure is owned by the State of Alaska; they have given us permission to

use their land for our study. The blue line indicates the 5 mile planned flight path of the unmanned aircraft (UA). While flying along this path, the UA will capture images of the river using visual, near infrared, and thermal cameras. The entire flight will take place in class G airspace below 1000’ AGL. The ground station will be setup at the GCS Location (68°43'35.95"N 149°28'32.53"W). This will also be the location for takeoff, landing, and the location the UA will fly back to incase of communication loss, fly away and lost-link.

The red polygon is a 5x2 mile rectangle that indicates the flight area. If the UA flies outside of this flight area, it will immediately return to the GCS Location and circle above it at 650’ AGL. This is extra security for the unlikely chance of a fly-away. This will also prevent the UA from flying over the pipeline located 3 miles south of the flight area.

Google Earth was used to create figure 1. A Google Earth KMZ file is included in the flight operations and can be opened in Google Earth to have a closer look at things (e.g. compare the flight area with a sectional map, measure distance, etc).

Observer Procedures

To keep the UA within line-of-sight (LOS), one observer is placed at the GCS Location and one observer is placed at each end of the flight area (a total of three observers during the flight). The downstream observer will be located at 68°44'40.92"N 149°30'13.15"W and the upstream observer will be located at 68°42'31.97"N 149°26'46.26"W. This always keeps the UA within a distance of 1 mile from an observer at all times. The yellow circles in figure 1 have a radius of 1 mile and display the observation area for each observer. When an observer has the UA within LOS, this observer will be referred to as the active observer. The active observer will report to the pilot every 30 seconds using a commercial handheld two-way radio. This report will include whether the UA is within sight and the current status of the airspace around the UA. If another aircraft enters the airspace around the UA the observer will use the two-way radio to alert the pilot and suggest appropriate avoidance maneuvers. During the planned flight over the river, the three observers will exchange the responsibility of the active observer as the UA flies out of LOS of one observer and into LOS of another observer. With the two-way radios, the active observer will make sure that the next observer is ready and has the UA within LOS before exchanging the responsibilities of the active observer. If LOS is not established with the next observer before the UA flies outside LOS of the active observer, then the pilot will abort the planned flight over the river and send a command to the aircraft to return to the GCS and circle above it at 650’ AGL.

If the pilot does not get a report every 30 seconds from the active observer, then communication loss is assumed and the pilot will abort the planned flight over the river and send a command to the aircraft to return to the GCS and circle above it at 650’ AGL. At the GCS location, the observer and the pilot are collocated and will always have communication. With an active observer at the GCS, the pilot can either reestablish communication with the other observers and continue the flight or land the aircraft.

Flight Operations

The list below summarizes the planned flight over the river. The flight will be less than 45 minutes.

1. Communication links between observers, the UA, and the pilot are checked before flight.
2. The UA is launched at the GCS Location (GCS observer is active)
3. After Takeoff, the UA circles around the GCS Location at 650’ and waits for further instruction.
4. The pilot checks the flight behavior of the UA to make sure it is functioning correctly.
5. The pilot sends the command to the UA to begin the 5 mile flight over the river.
6. The UA will fly toward the south point (upstream) of the flight path at 1000’ AGL.
7. Before the UA flies out of the GCS observation area, the GCS observer exchanges active observation to the upstream observer.
8. The UA begins its flight along the flight path at the southern point and follows the flight path toward the north (1000’ AGL).
9. Before the UA flies out of the upstream observation area, the upstream observer exchanges active observation to the GCS observer.
10. Before the UA flies out of the GCS observation area, the GCS observer exchanges active observation to the downstream observer.
11. When the UA finishes the flight over the river by reaching the northern (downstream) point of the flight path, it will turn around and return to the GCS Location.
12. Before the UA flies out of the downstream observation area, the downstream observer exchanges active observation to the GCS observer.
13. When the UA reaches the GCS Location, it will circle around it at 650’ AGL and wait for further instruction.
14. The pilot sends a command to the UA to land at the GCS Location.

Weather Conditions

Before going out to the site and setting up the ground station, the weather is checked to make sure the conditions are good for the UA and for acquiring the images. The UA will only be flown if the wind speed is less than 20 miles/hour and under sunny conditions.

Flight Log

General Flight Information	Aircraft Name		
	Flight Plan		
	Flight #		
	Date		
	Launch Time		
	Recovery Time		
	Duration		
	Temperature		
	Wind Speed		
	Wind Direction		
	Weather Condition		
	AGL Flight Altitude		
	Battery Numbers		
Pre-Flight Checklist	Airframe clean and in good condition		
	Motor/Prop mounted well		
	Control rods straight/servos mounted well		
	Payload Doors Clear		
	Tracker On		
	Payload installed		
	GCS displays correct aircraft		
	Aircraft battery level		
	GPS Quality		
	Correct position		
	AGL on ground		
	Payload Initialized		
	Payload doors Closed		
	Transmitter battery level		
	Correct transmitter mode / zero trim		
	Good RC Quality		
	Control surfaces respond correctly		
	Flaps respond correctly		
	Motor turns correctly / Log cleared		
	Correct Orientation		
	Check Air speed Indicator		
	Check transmitter fail safe		

Vita

Austin Jensen

✉ austin.m.jensen@ieee.org

Education

2010–Present **PhD in Electrical Engineering**, *Utah State University*, Logan UT.

2006–2009 **Masters in Electrical Engineering**, *Utah State University*, Logan UT, *3.95 GPA*.
Emphasis in controls

2003–2006 **Bachelors in Electrical Engineering**, *Utah State University*, Logan UT, *3.1 GPA*.
Maintained GPA while working 30 hours weekly, Received minor in Math

2000–2003 **Associates in Electrical Engineering**, *Snow College*, Ephraim UT, *3.1 GPA*.
Attended on music scholarship

Master thesis

Title *(gRAID): A GEOSPATIAL REAL-TIME AERIAL IMAGE DISPLAY FOR A LOW-COST AUTONOMOUS MULTISPECTRAL REMOTE SENSING PLATFORM (AggieAir)*

Supervisors Dr. YangQuan Chen (Major Professor), Dr. Rees Fullmer, Dr. Wei Ren

Description Image processing and payload development for a low-cost, autonomous, multispectral remote sensing platform called AggieAir

Experience

January 2009–Present **Research Engineer**, *Utah Water Research Laboratory*, Logan UT.
- Created the AggieAir Flying Circus: A service center at USU that uses AggieAir to capture aerial imagery
- Supervises students on future development and research with the AggieAir system
- Supervises the crew at the service center
- Maintains service center server (Web, FTP, Samba, and SVN services) and website
- Maintains other computers used for image processing
- Developed AggieAir into a product of which is currently sold by USU
- Developed new software and hardware in support of projects at the service center
- Participates in marketing activities to sell the AggieAir products and services
- Developed the training manuals used to train others to operate the AggieAir system
- Trains customers to operate AggieAir
- Gives support to customers that purchase the AggieAir system after training
- Applied for and received multiple Certificates of Authorization (COA) from the FAA to operate AggieAir in various locations
- Gives COA support to customers who purchase the AggieAir system
- Has 15 invention disclosures and 1 patent pending with USU

March 2006–January 2009 **Research Assistant**, *Center for Self Organizing and Intelligent Systems*, Logan UT.
- Involved in many projects which include: electrical chemical chip, SumoMotes, mesh sensor networking, and AggieAir
- Project leader for AggieAir and purchasing agent
- Graduate Teaching Assistant (2007). ECE5320 Mechatronics (4 credits, lab intensive)
- Web Master (2007), http://mechatronics.ece.usu.edu/ece5320
- REU Graduate Mentor and Outdoor Activity Planner (2007-2008)

Projects

SumoMote.

- Developed small mobile robot (SumoBot size) with manipulator
- Monitored and controlled bot on basestation through wireless link
- Became efficient using Java
- Proficient with Atmega RISC microcontrollers

SumoBot Competition.

- Took second place in competition by pushing other SumoBots out of ring
- Experienced with Zilog microcontroller, IR sensors and motor controllers

Robot Arm Playing Checkers.

- Built and programmed robot arm to play checkers with user through computer interface
- Became proficient with circuit design and how to interface hardware with computer

Electrochemical Chip.

- Interfaced electrochemical chip to computer through wireless mote
- Became experienced with nesC and TMotes

Near infrared radiometer.

- Designed radiometer using phototransister, lens and LCD display

Professional Service

- Reviewed papers for 2007 IEEE/ASME International Conference on Mechatronic and Embedded Systems and Applications
- Session Chair for 2009 IEEE/ASME International Conference on Mechatronic and Embedded Systems and Applications, The First Symposium on Small Unmanned Aerial Vehicle Technologies & Applications
- Reviewed papers for 2011 International Conference on Unmanned Aircraft Systems
- Reviewed papers for 2011 IEEE/ASME International Conference on Mechatronic and Embedded Systems and Applications
- Gave full day tutorial on UAV Personal Remote Sensing at the International Conference on Unmanned Aircraft Systems 2011
- Reviewed papers for 2012 International Conference on Unmanned Aircraft Systems
- Reviewed papers for 2012 IEEE/ASME International Conference on Mechatronic and Embedded Systems and Applications
- Gave full day tutorial on Thermal Remote Sensing at the International Conference on Unmanned Aircraft Systems 2012
- Reviewed papers for 2013 International Conference on Unmanned Aircraft Systems
- Reviewed papers for 2013 IEEE/ASME International Conference on Mechatronic and Embedded Systems and Applications
- Gave half day tutorial on Airworthiness Enhancing Architectures and Human Factors for Small Unmanned Aerial Systems at the International Conference on Unmanned Aircraft Systems 2013
- Reviewed journal paper for the Journal of Dynamic Systems, Measurement and Control, 2013
- Session Chair for 2013 International Conference on Unmanned Aircraft Systems
- Reviewed journal paper for ISA Transactions, 2013

Computer skills

Programming Languages C#, C++, C, Java, Python, Assembly, Matlab, nesC, LaTeX

Computer Programs Matlab, NASA World Wind, Eagle, Powerpoint, Excel, Word, IMAGINE

Languages

German **Semi-Proficient** *Lived in Germany for 4 months as exchange student. Studied for 2.5 years*

Honors, Awards and Recognitions

-Electrical and Computer Engineering Department Outstanding Graduate Teaching Assistant (2008-2009)

-IEEE IGARSS Student Travel Award (2008)

-2nd Place at UAS AUVSI 2008 Competition. Served as Graduate supervisor and Safety Pilot

-USU GSS Travel Grant to ASME/IEEE MESA07, Las Vegas

-Selected as participant of NSF REU experience on MAS-net

-Eagle Scout

Community Service

-Gave many lectures on using UAVs for remote sensing for a GIS class at USU

-Volunteered: Logan Multiple Sclerosis Bike Race

-Volunteered: Diabetic Camp for children (3 years)

-UAV demo: Edith Bowen Elementary School

References

Dr. YangQuan Chen, *yqchen@ece.usu.edu*, (435)797-0148.

Dr. Don Cripps, *don.cripps@usu.edu*, (435)797-8171.

Dr. Mac Mckee, *mac.mckee@usu.edu*, (435)797-3157.

Publications

Steven L Barfuss, Austin Jensen, and Shannon Clemens. Evaluation and Development of Unmanned Aircraft (UAV) for UDOT Needs. Technical report, Utah State University, 2012.

Haiyang Chao, Marc Baumann, Austin Jensen, YangQuan Chen, Yongcan Cao, Wei Ren, and Mac McKee. Band-reconfigurable Multi-UAV-Based Cooperative Remote Sensing for Real-Time Water Management and Distributed Irrigation Control. In *In Proceedings of the IFAC World Congress*, Seoul, Korea, July 2008.

Haiyang Chao, Austin M. Jensen, Yiding Han, YangQuan Chen, and Mac McKee. Advances in Geoscience and Remote Sensing. In Gary Jedlovec, editor, *Advances in Geoscience and Remote Sensing*, pages 463–489. INTECH, October 2009.

Cal Coopmans, Austin Jensen, and YangQuan Chen. Fractional-Order Complementary Filter for Small Unmanned Aerial System Navigation. In *Proc. of the International Conference on Unmanned Aircraft Systems (ICUAS)*, 2013.

Calvin Coopmans, Long Di, Austin Jensen, Aaron A. Dennis, and YangQuan Chen. Improved Architecture Designs for a Low Cost Personal Remote Sensing Platform: Flight Control and Safety. In *Volume 3: 2011 ASME/IEEE International Conference on Mechatronic and Embedded Systems and Applications, Parts A and B*, volume 2011, pages 937–943. ASME, 2011.

Calvin Coopmans, Austin M. Jensen, and YangQuan Chen. Fractional-Order Complementary Filters for Small Unmanned Aerial System Navigation. *Journal of Intelligent & Robotic Systems*, October 2013.

Christopher Hall, Daniel Morgan, Austin M Jensen, Haiyang Chao, YangQuan Chen, and Mac McKee. Multiple Micro Aerial Vehicles for Applications in Real-Time Remote Sensing. In *AWRA 2008 Annual Water Resources Conference*, New Orleans, LA, USA, November 2008.

Christopher J. Hall, Daniel Morgan, Austin Jensen, Haiyang Chao, Calvin Coopmans, Mitchel Humpherys, and YangQuan Chen. Team OSAM-UAV's Design for the 2008 AUVSI Student UAS Competition. In *Volume 3: ASME/IEEE 2009 International Conference on Mechatronic and Embedded Systems and Applications; 20th Reliability, Stress Analysis, and Failure Prevention Conference*, volume 2009, pages 575–584. ASME, 2009.

Yiding Han, Austin Jensen, and Huifang Dou. Programmable Multispectral Imager Development as Light Weight Payload for Low Cost Fixed Wing Unmanned Aerial Vehicles. In *Proceedings of the 2009 {ASME/IEEE} International Design Engineering Technical Conferences & Computers and Information in Engineering Conference*, San Diego, CA, USA, August 2009.

Nathan Hoffer, Cal Coopmans, Austin Jensen, and YangQuan Chen. Small Low-Cost Unmanned Aerial Vehicle System Identification: A Survey and Catagorization. In *Proc. of the International Conference on Unmanned Aircraft Systems (ICUAS)*, 2013.

Nathan V. Hoffer, Calvin Coopmans, Austin M. Jensen, and YangQuan Chen. A Survey and Categorization of Small Low-Cost Unmanned Aerial Vehicle System Identification. *Journal of Intelligent & Robotic Systems*, October 2013.

Austin Jensen. gRAID: A Geospatial Real-Time Aerial Image Display for a Low-Cost Autonomous Multispectral Remote Sensing Platform (AggieAir). Masters thesis, Utah State University, 2009.

Austin Jensen and Yangquan Chen. Calibration Method for Aerial Vehicles. US Patent App. 12/835,417, 2010.

Austin Jensen and YangQuan Chen. Tracking Tagged Fish with Swarming Unmanned Aerial Vehicles Using Fractional Order Potential Fields and Kalman Filtering. In *Proc. of the International Conference on Unmanned Aircraft Systems (ICUAS)*, 2013.

Austin Jensen, Cal Coopmans, and YangQuan Chen. Basics and Guidelines of Complementary Filters for Small UAS Navigation. In *Proc. of the International Conference on Unmanned Aircraft Systems (ICUAS)*, 2013.

Austin Jensen, B.T. Neilson, M. McKee, and Y.Q. Chen. Thermal Remote Sensing With an Autonomous Unmanned Aerial Remote Sensing Platform for Surface Stream

Temperatures. In *Proc. IEEE Int. Geoscience and Remote Sensing Symp. (IGARSS)*, pages 5049–5052, 2012.

Austin M Jensen, Marc Baumann, and YangQuan Chen. Low-Cost Multispectral Aerial Imaging Using Autonomous Runway-Free Small Flying Wing Vehicles. In *Proc. IEEE Int. Geoscience and Remote Sensing Symp. (IGARSS)*, July 2008.

Austin M Jensen, YangQuan Chen, Thom Hardy, and Mac McKee. AggieAir - A Low-cost Autonomous Multispectral Remote Sensing Platform: New Developments and Applications. In *Proc. IEEE Int. Geoscience and Remote Sensing Symp. (IGARSS)*, July 2009.

Austin M. Jensen, David K. Geller, and YangQuan Chen. Monte Carlo Simulation Analysis of Tagged Fish Radio Tracking Performance by Swarming Unmanned Aerial Vehicles in Fractional Order Potential Fields. *Journal of Intelligent & Robotic Systems*, October 2013.

Austin M Jensen, Yiding Han, and YangQuan Chen. Using Aerial Images to Calibrate Inertial Sensors of a Low-cost Multispectral Autonomous Remote Sensing Platform (AggieAir). In *Proc. IEEE Int. Geoscience and Remote Sensing Symp. (IGARSS)*, July 2009.

Austin M Jensen, Thomas Hardy, Mac McKee, and Yang Quan Chen. Using a Multispectral Autonomous Unmanned Aerial Remote Sensing Platform (AggieAir) for Riparian and Wetland Applications. In *Proc. IEEE Int. Geoscience and Remote Sensing Symp. (IGARSS)*, August 2011.

Austin M. Jensen, Mac McKee, and YangQuan Chen. Calibrating Thermal Imagery from an Unmanned Aerial System - AggieAir. In *Proc. IEEE Int. Geoscience and Remote Sensing Symp. (IGARSS)*, 2013.

Austin M Jensen, Daniel Morgan, Shannon Clemens, YangQuan Chen, and Thomas Hardy. Using Multiple Open-Source Low-Cost Unmanned Aerial Vehicles (UAV) for 3D Photogrammetry and Distributed Wind Measurement. In *Proceedings of the 2009 {ASME/IEEE} International Design Engineering Technical Conferences & Computers and Information in Engineering Conference*, August 2009.

Austin M Jensen, Norman Wildmann, YangQuan Chen, and Holger Voos. In-situ Unmanned Aerial Vehicle (UAV) Sensor Calibration to Improve Automatic Image Orthorectification. In *Proc. IEEE Int. Geoscience and Remote Sensing Symp. (IGARSS)*, pages 596–599, July 2010.

Miguel Leonardo, Austin Jensen, Calvin Coopmans, Mac McKee, and Yangquan Chen. A Miniature Wildlife Tracking UAV Payload System using Acoustic Biotelemetry. In *Proc. of the ASME International Design Engineering Technical Conferences & Computers and Information in Engineering Conference*, 2013.

Michal Podhradsky, Jarret Bone, Austin Jensen, and Calvin Coopmans. Smal Low-cost Unmanned Aerial Vehicle Lithium-polymer Battery Monitoring System. In *Proc. of the ASME International Design Engineering Technical Conferences & Computers and Information in Engineering Conference*, 2013.

Michal Podhradsky, Cal Coopmans, and Austin Jensen. Battery Model-Based Thrust Controller for a Small, Low Cost Multirotor Unmanned Aerial Vehicles. In *Proc. of the International Conference on Unmanned Aircraft Systems (ICUAS)*, 2013.

Michal Podhradský, Calvin Coopmans, and Austin Jensen. Battery State-Of-Charge Based Altitude Controller for Small, Low Cost Multirotor Unmanned Aerial Vehicles. *Journal of Intelligent & Robotic Systems*, October 2013.

Bushra Zaman, Mac McKee, and Austin Jensen. Use of High-Resolution Multispectral Imagery Acquired with an Autonomous Unmanned Aerial Vehicle to Quantify the Spread of an Invasive Wetland Species. In *Proc. IEEE Int. Geoscience and Remote Sensing Symp. (IGARSS)*, August 2011.